

AD-A044 849

CHARLES STARK DRAPER LAB INC CAMBRIDGE MASS  
DEVELOPMENT OF CAPABILITY FOR MULTIFUNCTION INTEGRATED REFERENC--ETC(U)  
JUL 77 K DALY, R NURSE, G SCHMIDT, P MOTYKA F33615-76-C-1216

F/G 1/3

UNCLASSIFIED

R-1042

AFAL-TR-77-64

NL

1 OF 2  
ADA  
044849



ADA 044849

AFAL-TR-77-64

mc 2

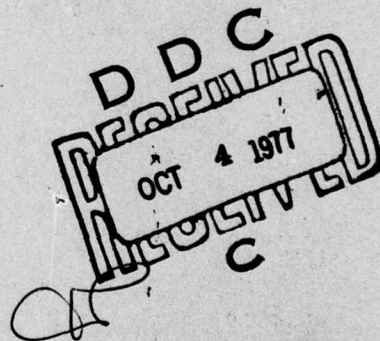
DEVELOPMENT OF CAPABILITY FOR MULTIFUNCTION  
INTEGRATED REFERENCE ASSEMBLY EVALUATION

The Charles Stark Draper Laboratory, Inc.  
Cambridge, Massachusetts 02139

July 1977

TECHNICAL REPORT AFAL-TR-77-64,

Final Report for Period 1 June 1976 through 31 March 1977



DDC FILE COPY

Approved for public release; distribution unlimited.

AIR FORCE AVIONICS LABORATORY  
AIR FORCE WRIGHT AERONAUTICAL LABORATORIES  
AIR FORCE SYSTEMS COMMAND  
WRIGHT-PATTERSON AIR FORCE BASE, OHIO 45433



NOTICE

When Government drawings, specifications, or other data are used for any purpose other than in connection with a definitely related Government procurement operation, the United States Government thereby incurs no responsibility nor any obligation whatsoever; and the fact that the Government may have formulated, furnished, or in any way supplied the said drawings, specifications, or other data, is not to be regarded by implication or otherwise as in any manner licensing the holder or any other person or corporation, or conveying any rights or permission to manufacture, use, or sell any patented invention that may in any way be related thereto.

This report has been reviewed and is approved for publication.

*Jack W. Bell*  
Project Engineer

FOR THE COMMANDER

*Ronald L. Ringo*  
RONALD L. RINGO  
Chief, Reference Systems Branch  
Reconnaissance & Weapon Delivery Div

ACCESSION for	
NTIS	White Section <input checked="" type="checkbox"/>
DDC	Buff Section <input type="checkbox"/>
UNANNOUNCED	
JUSTIFICATION	
BY	
DISTRIBUTION/AVAILABILITY CODES	
Dist.	SPECIAL
A	

Copies of this report should not be returned unless return is required by security considerations, contractual obligations, or notice on a specific document.

UNCLASSIFIED

SECURITY CLASSIFICATION OF THIS PAGE (When Data Entered)

19 REPORT DOCUMENTATION PAGE		READ INSTRUCTIONS BEFORE COMPLETING FORM
1. REPORT NUMBER AFAL-TR-77-64	2. GOVT ACCESSION NO.	3. RECIPIENT'S CATALOG NUMBER
4. TITLE (and Subtitle) DEVELOPMENT OF CAPABILITY FOR MULTIFUNCTION INTEGRATED REFERENCE ASSEMBLY EVALUATION.		5. TYPE OF REPORT & PERIOD COVERED Final Technical Report 6/1/76 - 3/31/77
7. AUTHOR(s) Daly, K; Motyka, P; Nurse, R; Palmer, P. Schmidt, G.		6. PERFORMING ORG. REPORT NUMBER R-1042
9. PERFORMING ORGANIZATION NAME AND ADDRESS The Charles Stark Draper Laboratory, Inc. Cambridge, Massachusetts 02139		8. CONTRACT OR GRANT NUMBER(s) F33615-76-C-1216
11. CONTROLLING OFFICE NAME AND ADDRESS Air Force Avionics Laboratory (RWA) Wright-Patterson Air Force Base Dayton, Ohio 45433		10. PROGRAM ELEMENT, PROJECT, TASK AREA & WORK UNIT NUMBERS Project 6095
14. MONITORING AGENCY NAME & ADDRESS (if different from Controlling Office) K. /Daly R. /Nurse G. /Schmidt P. /Motyka P. /Palmer		12. REPORT DATE Jul 1977
16. DISTRIBUTION STATEMENT (of this Report) Approved for public release; distribution unlimited		13. NUMBER OF PAGES 117
17. DISTRIBUTION STATEMENT (of the abstract entered in Block 20, if different from Report)		15. SECURITY CLASS. (of this report) UNCLASSIFIED
18. SUPPLEMENTARY NOTES		15a. DECLASSIFICATION/DOWNGRADING SCHEDULE
19. KEY WORDS (Continue on reverse side if necessary and identify by block number) Simulation Development Inertial Navigation Systems Life Cycle Cost MIRA		
20. ABSTRACT (Continue on reverse side if necessary and identify by block number) The significance of this research and development to the Air Force is the development of the tools and techniques required to assess the feasibility of using a minimum number of inertial sensors to provide the inertial reference information consistent with aircraft requirements for weapon delivery, flight control, navigation, fire control, and flight safety. Multifunction Inertial Reference Assembly (MIRA) is the term which describes the generic class of systems designed to meet this objective. Emphasis is placed on the		

DD FORM 1473 1 JAN 73 EDITION OF 1 NOV 65 IS OBSOLETE

UNCLASSIFIED 408 386

SECURITY CLASSIFICATION OF THIS PAGE (When Data Entered)

UNCLASSIFIED

SECURITY CLASSIFICATION OF THIS PAGE (When Data Entered)

20. Abstract (Continued)

development of a simulation capability for the evaluation of MIRA systems in realistic environments. A definition of the aircraft and flight-control system selected for the simulation is included along with a consideration of the inertial-sensor requirements for MIRA systems. Results demonstrating the capability of the simulation are presented. The life-cycle-cost implications of the MIRA approach are also dealt with.

UNCLASSIFIED

SECURITY CLASSIFICATION OF THIS PAGE (When Data Entered)



#### ACKNOWLEDGMENT

The work documented in this report was accomplished under USAF Contract F33615-76-C-1216 by The Charles Stark Draper Laboratory, Inc., Cambridge, Massachusetts. The monitoring Air Force project engineer is Mr. J. Bell (RWA-666A), Air Force Avionics Laboratory, Dayton, Ohio.

The Draper Laboratory Program Manager is Dr. G. Schmidt and the Technical Director is Dr. K. Daly. Contributors to this report are K. Daly, P. Motyka, R. Nurse, P. Palmer, and G. Schmidt. D. Hauger and M. Santarelli were responsible for the programming of the simulation.

## TABLE OF CONTENTS

<u>Section</u>	<u>Page</u>
1 INTRODUCTION.....	1
2 DEFINITION OF AIRCRAFT AND FLIGHT-CONTROL REQUIREMENTS.....	2
2.1 Introduction.....	2
2.2 Aircraft Definition.....	3
2.3 Flight-Control Definition.....	3
2.4 Future Aircraft and Flight-Control Capabilities.....	4
2.5 Inertial-Sensor Requirements for MIRA.....	5
2.5.1 Introduction.....	5
2.5.2 Approach for Determining Sensor Characteristics.....	6
2.5.3 Inertial-Sensor Requirements For Stability Augmentation.....	7
2.5.4 INS Requirements for Tactical Applications.....	9
2.5.5 Minimum Sensor Configuration.....	12
3 MIRA SIMULATION DEVELOPMENT.....	14
3.1 Introduction.....	14
3.2 General Description of MIRA Simulation Characteristics.....	15
3.3 Vehicle Six-Degree-of-Freedom Nonlinear Equations of Motion.....	17
3.4 Vehicle Aerodynamics.....	26
3.5 Thrust Forces and Moments.....	30
3.6 Trim Algorithm.....	31
3.7 Structural Modes.....	33
3.8 Flight-Control System.....	37
3.9 Simulation Inputs.....	41
3.10 Turbulence Simulation.....	42

# TABLE OF CONTENTS (Cont.)

<u>Section</u>	<u>Page</u>
3.11 Sensor Models.....	43
3.12 Navigation System Model.....	49
3.13 A General Description of the Navigation and Attitude-Error Propagation Model.....	59
4 DEMONSTRATION OF MIRA SIMULATION CAPABILITY AND COMPARISON OF RESULTS.....	62
4.1 Introduction.....	62
4.2 Data for MIRA Simulation Runs.....	62
4.3 MIRA Simulation Results.....	70
4.4 Conclusions from MIRA Simulation Results.....	89
5 LIFE-CYCLE COST MODELING.....	91
5.1 Introduction.....	91
5.2 Objective.....	93
5.3 LCC Model Survey.....	93
5.4 The CRIER Model.....	94
5.5 LCC Impact on Design.....	95
6 SUMMARY AND CONCLUSIONS.....	98
6.1 Phase I Summary.....	98
6.2 Phase II Inputs.....	100
LIST OF REFERENCES.....	102



# LIST OF SYMBOLS

$b$	Reference span of wing, ft.
$\bar{c}$	Mean aerodynamic chord, ft.
$cg$	Center of gravity.
$cg_{pos}$	Position of aircraft center of gravity, ( $\frac{\% \text{ of } \bar{c}}{100}$ ).
$C_1, C_2, C_3$	Constants of vertical-damping system.
$C_\ell, C_m, C_n$	Rolling, pitching, and yawing moment coefficients of vehicle.
$C_x, C_y, C_z$	Longitudinal, lateral, and normal body-axes force coefficients.
$C_{xy}, C_{yy}$	Coefficients representing lateral-accelerometer cross-coupling and nonlinear effects.
$[f]$	Specific-force vector, $ft/s^2$ .
$[F]$	Force vector of vehicle, lb.
$[F_{aero}]$	Aerodynamic force vector, lb.
$[F_{grav}]$	Vector of vehicle body-axes gravitational forces, $ft/s^2$ .
$F_{L_x}, F_{L_y}, F_{L_z}$	Left-engine thrust forces along vehicle, x, y, z body axes, lb.
$F_{R_x}, F_{R_y}, F_{R_z}$	Right-engine thrust forces along vehicle x, y, z body axes, lb.
$[F_{SM}]$	Vector of forces due to structural modes, lb.
$[F_{T_L}], [F_{T_R}]$	Vector of left- and right-engine thrust forces, lb.
$F_x, F_y, F_z$	Forces along vehicle x, y, z body axes, lb.
$F_{SM_x}, F_{SM_y}, F_{SM_z}$	Forces due to structural modes along vehicle x, y, z body axes, lb.

$g$	Acceleration due to gravity, $\text{ft/s}^2$ .
$[g]$	Navigation-system gravity vector, $\text{ft/s}^2$ .
$g_0$	Gravitational constant, $32.1725 \text{ ft/s}^2$ .
$g_x, g_y, g_z$	Components of navigation-system gravity vector, $\text{ft/s}^2$ .
$h$	Altitude of vehicle cg above surface of earth, ft.
$\dot{h}$	Altitude rate, $\text{ft/s}$ .
$h_N$	Navigation-system altitude, ft.
$[I]$	Matrix of vehicle moments of inertia, $\text{slug-ft}^2$ .
$[I_0]$	Identity matrix.
$I_x, I_y, I_z$	Vehicle moments of inertia about x, y, z body axes, $\text{slug-ft}^2$ .
$I_{xz}$	Vehicle product of inertia about x, z body axes, $\text{slug-ft}^2$ .
$K$	Gain of second-order system.
$K_f$	Rudder-flexibility gain.
$K_g$	Gust filter gain, $\sqrt{\pi/\Delta t}$ .
$K_{n_y}$	Lateral-acceleration feedback gain, $\text{deg/g}$ .
$K_{n_z}$	Normal-acceleration feedback gain, $\text{deg/g}$ .
$K_p$	Roll-rate feedback gain, $\text{deg/deg/s}$ .
$K_q$	Pitch-rate feedback gain, $\text{deg/deg/s}$ .
$K_r$	Yaw-rate feedback gain, $\text{deg/deg/s}$ .
$[l]$	Vector of distances along x, y, z body axes from cg to accelerometer location, ft.
$L_v, L_w$	$v_g, w_g$ turbulence scales, ft.
$m$	Mass of vehicle, slugs.
$M$	Mach number.
$[M]$	Vehicle moment vector, $\text{ft-lb}$ .
$[M_{\text{aero}}]$	Aerodynamic moment vector, $\text{ft-lb}$ .
$M_{L_x}, M_{L_y}, M_{L_z}$	Moments due to left-engine thrust, $\text{ft-lb}$ .
$M_{R_x}, M_{R_y}, M_{R_z}$	Moments due to right-engine thrust, $\text{ft-lb}$ .

$M_{SM_x}, M_{SM_y}, M_{SM_z}$	Rolling, pitching, yawing moments due to structural modes, ft-lb.
$[M_{SM}]$	Vector of vehicle moments due to structural modes, ft-lb.
$[M_{T_L}], [M_{T_R}]$	Vector of vehicle moments due to left-, right-engine thrust, ft-lb.
$M_{\alpha}$	Pitching moment due to angle-of-attack rate.
$[n]$	Vector of vehicle rigid-body accelerations at distance [1] from cg, g.
$N_{wind}, E_{wind}, D_{wind}$	Earth-surface wind components defined as wind from north, wind from east, and wind from below, ft/s.
$n_x, n_y, n_z$	Vehicle rigid-body accelerations at accelerometer location, positive along x, y, z body axes, g.
$n_{x_{BI}}, n_{y_{BI}}, n_{z_{BI}}$	Integrated longitudinal-, lateral-, and normal-accelerometer signals, ft/s.
$n_{x_{BIML}}, n_{y_{BIML}}, n_{z_{BIML}}$	Integrated longitudinal-, lateral-, and normal-accelerometer signals including effects of misalignment and lag, ft/s.
$n_{y_B}, n_{z_B}$	Lateral- and normal-accelerometer signals including structural-mode effects, g's.
$n_{y_{FCS}}$	Lateral-accelerometer flight-control-system feedback signal, g's.
$p, q, r$	Angular inertial velocities of vehicle about x, y, z body axes, deg/s or rad/s.
$p_A, q_A, r_A$	Body-axes angular velocities with respect to the local atmosphere, rad/s.
$p_G, r_G$	Vehicle roll- and yaw-rate signals about principal axes, deg/s.
$p_{GB}, q_{GB}, r_{GB}$	Roll-, pitch-, yaw-rate signals including bending effects, deg/s or rad/s.
$p_{GCT}$	Roll-rate gyro pulse count.
$p_{GCTI}$	Integerized roll-rate-gyro pulse count.



$p_{GFCS}, q_{GFCS}, r_{GFCS}$	Roll-, pitch-, yaw-rate flight-control-system feedback signals, deg/s.
$p_{GI}, q_{GI}, r_{GI}$	Integrated roll-, pitch-, yaw-rate signals, rad.
$p_{GIM}$	Integrated roll-rate gyro signal including misalignment effects, rad.
$p_0, p_1, p_2, p_3$	Parameters used in navigation-system quaternion update.
$p_{rel}, q_{rel}, r_{rel}$	Body-axes angular velocities with respect to earth, rad/s.
$\bar{q}$	$1/2 \rho V_a^2$ , dynamic pressure, lb/ft <sup>2</sup> .
$q_0, q_1, q_2, q_3$	Parameters of navigation-system quaternion update.
$[r]$	Distance vector.
$R_E$	$R_0 + h$ , actual distance of vehicle cg from center of earth, ft.
$R_0$	Radius of spherical earth, $2.086(10^7)$ ft.
$s$	Laplace-transform variable, s <sup>-1</sup> .
$S$	Wing area, ft <sup>2</sup> .
$SF_{n_Y}$	Lateral-accelerometer scale factor, pulses/ft/s.
$SF_{p_G}$	Roll-rate-gyro scale factor, pulses/rad.
$t_d(\omega)$	Time delay of second-order system, s.
$T$	Transfer function of second-order system.
$[T_{BC}]$	Body frame to navigation-system computational-frame transformation matrix.
$T_{BG_{ij}}$	$ij^{th}$ element of $[T_{BC}]$ .
$[T_{CE}]$	Navigation-system computational frame to earth-surface-frame transformation matrix.
$T_{CE_{ij}}$	$ij^{th}$ element of $[T_{CE}]$ .
$[T_{ESB}]$	Earth surface to body-axes transformation matrix.
$T_L, T_R$	Left- and right-engine thrust, lb.
$T_{v_g}, T_{w_g}$	$v_g, w_g$ filter transfer functions.
$u, v, w$	Linear inertial x, y, z body-axes velocities, ft/s.

$u_{EI}, v_{EI}, w_{EI}$	Linear velocities of earth with respect to inertial frame in body axes, ft/s.
$u_g, v_g, w_g$	Body-axes gust velocities, ft/s.
$u_{rel}, v_{rel}, w_{rel}$	Vehicle linear body-axes velocities with respect to earth, ft/s.
$u_{wind}, v_{wind}, w_{wind}$	Body-axes wind velocities, ft/s.
[V]	Vector of vehicle linear inertial-body-axes velocities, ft/s.
$V_A$	True airspeed, ft/s.
[V <sub>A</sub> ]	Vector of linear body-axes velocities with respect to the local atmosphere, ft/s.
$V_{A_x}, V_{A_y}, V_{A_z}$	Linear x, y, z body-axes velocities with respect to the local atmosphere, ft/s.
[V <sub>E</sub> ]	Vector of linear earth velocities with respect to inertial frame in earth axes, ft/s.
[V <sub>EI</sub> ]	Vector of linear earth velocities with respect to inertial frame in body axes, ft/s.
[V <sub>gust</sub> ]	Vector of linear body-axes gust velocities, ft/s.
$V_{L_x}, V_{L_y}, V_{L_z}$	Local vertical north vehicle velocities obtained from navigation system, ft/s.
[V <sub>NC</sub> ]	Vector of computational-frame velocities calculated by navigation system, ft/s.
$V_{NC_x}, V_{NC_y}, V_{NC_z}$	Total computational-frame velocities along x, y, z navigation-system axes, ft/s.
$V_{NC_x}^{(d)}$	Damped navigation-system vertical velocity, ft/s.
[V <sub>rel</sub> ]	Vector of linear body-axes velocities with respect to earth, ft/s.
$V_{rel}$	Total relative velocity, ft/s.
$V_s$	Speed of sound, ft/s.
[V <sub>wind</sub> ]	Vector of linear body-axes wind velocities, ft/s.
$w_A$	Wander angle, deg.

$[W]$	Vector of wind velocities with respect to earth in earth-axes frame, ft/s.
$x, y, z$	Axes of orthogonal coordinate system.
$[\dot{X}]$	Vector of linear velocities of earth-surface frame with respect to the earth, ft/s.
$\dot{x}, \dot{y}, \dot{z}$	Earth-surface-frame velocities with respect to earth, ft/s.
$x_{n_x}, y_{n_x}, z_{n_x}$	Location of longitudinal accelerometer relative to cg, ft.
$x_{n_y}, y_{n_y}, z_{n_y}$	Location of lateral accelerometer relative to cg, ft.
$x_{n_z}, y_{n_z}, z_{n_z}$	Location of normal accelerometer relative to cg, ft.
$\alpha$	Angle of attack, deg.
$\alpha_G$	Angle between x body axis and x principal axis, $-1.5^\circ$ .
$\beta$	Sideslip angle, deg.
$\gamma$	Flightpath angle, deg.
$\delta_a$	Combined spoiler and aileron deflection, positive trailing edge right surface down, rad or deg.
$\overline{\delta a}$	Variable in vertical-damping system of navigation model, $\text{ft/s}^2$ .
$\delta_e$	Horizontal tail deflection, positive trailing edge down, rad or deg.
$\delta h$	Altitude error, $h-h_N$ , ft.
$\partial h / \partial \eta_1, \partial h / \partial \eta_2, \partial h / \partial \eta_3$	Bending displacement per $\eta_1, \eta_2, \eta_3$ at normal-accelerometer location, positive displacement down, ft.
$\partial h / \partial \eta_6$	Lateral bending displacement per $\eta_6$ at lateral-accelerometer location, positive displacement down, ft.
$\delta_r$	Rudder surface deflection, positive trailing edge left, rad or deg.
$\delta_{RP}$	Rudder-pedal input, lb.
$\delta_{s_x}$	Longitudinal center-stick input, lb.
$\delta_{s_y}$	Roll center-stick input, lb.
$\delta_T$	Throttle input, deg.
$\Delta$	Incremental value from trim.



$\Delta b_{n_y}$	Lateral-accelerometer bias error, ft/s.
$\Delta b_{p_G}$	Roll-rate-gyro bias error, rad.
$\Delta c_g$	Difference in actual cg position and cg position at which aerodynamic coefficients are defined.
$\Delta n_{z_{FCS}}$	Incremental normal-accelerometer flight-control-system feedback signal, g.
$\Delta t$	Vehicle computation time increment, s.
$\Delta t_{HI}$	High-speed navigation-system computation increment, 0.02 s.
$\Delta t_{LO}$	Low-speed navigation-system computation increment, 0.2 s.
$\Delta V_{N_x}, \Delta V_{N_y}, \Delta V_{N_z}$	Accelerometer outputs transformed to navigation computational frame, ft/s.
$\Delta V_x, \Delta V_y, \Delta V_z$	Values of $V_{N_x}, V_{N_y}, V_{N_z}$ summed over low-speed navigation-system computation time, ft/s.
$\Delta V_{x_A}, \Delta V_{y_A}, \Delta V_{z_A}$	Integrated longitudinal-, lateral-, and normal-accelerometer inputs to navigation system, ft/s.
$\Delta x, \Delta y, \Delta z$	Distances along x, y, z body axes from cg to point-of-thrust application, ft.
$\epsilon_{n_y}$	Lateral-accelerometer scale-factor error.
$\epsilon_{p_G}$	Roll-rate-gyro scale-factor error.
$\zeta$	Damping ratio of second-order system.
$\zeta_1, \zeta_2$	Coefficients accounting for lateral-accelerometer misalignment errors.
$\eta_i$	Generalized bending-mode coefficient, $i = 1, 2, \dots, 6$ .
$[\Delta \theta]$	Vector of incremental angular rates of the vehicle body frame with respect to the navigation computational frame, rad.
$[\Delta \theta_B]$	Vector of incremental navigation gyro signals, rad.
$\Delta \theta_{B_x}, \Delta \theta_{B_y}, \Delta \theta_{B_z}$	Yaw-, pitch-, and roll-rate incremental navigation gyro signals, rad.
$\partial \theta / \partial \eta_1, \partial \theta / \partial \eta_2, \partial \theta / \partial \eta_3$	Pitch slope per $\eta_1, \eta_2, \eta_3$ positive nose up, rad.

$\lambda$	Latitude, rad or deg.
$\lambda_T$	Angle-of-thrust orientation, deg.
$\mu_1, \mu_2$	Coefficients accounting for roll-rate-gyro misalignment errors.
$\rho$	Air density, slugs/ft <sup>3</sup> .
$\sigma$	Longitude, rad or deg.
$\sigma_v, \sigma_w$	rms intensities of $v_g$ and $w_g$ , ft/s.
$\tau$	Filter time constant, s.
$\phi, \theta, \psi$	Roll, pitch, yaw angles of body axes with respect to earth-surface frame, deg or rad.
$\phi(\omega)$	Phase angle of second-order system, rad.
$\phi_T$	Angle-of-thrust orientation, deg.
$\partial\phi/\partial\eta_4, \partial\phi/\partial\eta_5, \partial\phi/\partial\eta_6$	Roll slope per $\eta_4, \eta_5, \eta_6$ , positive right wing down, rad.
$\psi'$	$\psi - w_A$ , rad.
$\partial\psi/\partial\eta_6$	Yaw slope per $\eta_6$ , positive nose right, rad.
$\omega$	Angular frequency, rad/s.
$\omega_n$	Natural angular frequency of second-order system, rad/s.
$[\omega]$	Vector of vehicle inertial-body-axes angular velocities, rad/s.
$[\omega_A]$	Vector of body-axes angular velocities with respect to the local atmosphere, rad/s.
$[\omega_{CE}]$	Vector of navigation-system computational-frame angular velocities with respect to earth, rad/s.
$[\omega_{CE}^X]$	Skew symmetric form of $[\omega_{CE}]$ .
$\omega_{CE_x}, \omega_{CE_y}, \omega_{CE_z}$	Navigation-system angular velocities about level axes, rad/s.
$[\omega_{CI}]$	Vector of navigation-system computational-frame angular velocities with respect to inertial reference, rad/s.
$\omega_{CI_x}, \omega_{CI_y}, \omega_{CI_z}$	Components of $[\omega_{CI}]$ .

$\omega_E$	Angular rate of earth rotation, $7.292(10^{-5})$ rad/s.
$[\omega_E]$	Vector of angular velocities of earth with respect to inertial frame in earth axes system, rad/s.
$[\omega_{EI}]$	Vector of angular velocities of earth with respect to inertial frame in body axes, rad/s.
$[\omega_{EI\chi}]$	Skew symmetric form of $[\omega_{EI}]$ .
$\omega_{EI_x}, \omega_{EI_y}, \omega_{EI_z}$	Components of $[\omega_{EI}]$ .
$[\omega_{rel}]$	Vector of body-axes angular velocities with respect to earth-centered frame, rad/s.
$[\omega_{rel\chi}]$	Skew symmetric form of $[\omega_{rel}]$ .
$[\omega\chi]$	Skew symmetric form of $[\omega]$ .
$\omega_x, \omega_y, \omega_z$	Body-axes angular velocities with respect to the earth-surface frame, rad/s.
$\omega_1, \omega_2, \omega_3$	Linear velocities in navigation-system velocity equation due to coupling between the angular velocities of the computational frame with respect to earth and the angular velocities of the earth with respect to the inertial reference with the computational-frame linear velocities, ft/s.

#### Subscripts

aero	Aerodynamic.
B	Body axes.
C	Navigation LVWA computational frame.
E	Earth centered frame.
err	Error.
grav	Gravitational.
I	Inertial-reference frame.
k	$k^{th}$ iteration of vehicle equations.
L	Left.
m	$m^{th}$ iteration of low-speed navigation system.
n	$n^{th}$ iteration of high-speed navigation system.
N	Navigation system.

ortho	Orthonormalized.
rel	Earth relative.
R	Right.
T	Thrust.
t	Trim.

#### Superscripts

-1	Inverse.
( $\cdot$ )	First derivative with respect to time.
( $\ddot{\phantom{x}}$ )	Second derivative with respect to time.

## SECTION 1

### INTRODUCTION

This Research and Development Technical report covers the work performed from 1 June to 31 December 1976 under Contract F33615-76-R-1216. This report is submitted in fulfillment of CDRL Sequence 3, dated 3 December 1975.

In accordance with the Statement of Work, the overall objective of this effort is to develop the tools and techniques required to assess the technical feasibility of using a minimum number of inertial sensors to provide the inertial-reference information consistent with the requirements for weapon delivery, flight control, navigation, fire control, and flight safety of an aircraft. The term Multifunction Inertial Reference Assembly (MIRA) will be used to describe the generic class of systems designed to meet this objective.

This MIRA effort is primarily oriented toward developing and demonstrating simulation capabilities to evaluate MIRA-type systems in realistic environments, and toward consideration of the life-cycle cost implications of the MIRA approach. The attempt is not to propose or evaluate specific systems as candidate MIRA approaches, but to develop a versatile evaluation capability which will have long-term utility in the MIRA effort.

The effort under Contract F33615-76-R-1216 is divided into three tasks: definition of program specifics, analysis and simulation development, and simulation and mechanization studies. The results of the first task are discussed in Section 2 of this report. The results of the second task are discussed in Section 3 (for the aircraft simulation), and Section 5 (for life-cycle cost models). The results of the third task are discussed in Section 4 (for the MIRA engineering and performance studies). Section 6 summarizes the results of the effort, and provides transitional information related to utilization in the development of the MIRA concept.



## SECTION 2

### DEFINITION OF AIRCRAFT AND FLIGHT-CONTROL REQUIREMENTS

#### 2.1 Introduction

At the beginning of the MIRA effort, a survey of potential candidate vehicles for use in simulating the "high-performance" application of the MIRA system was conducted. Although it was recognized at the time that a model of a state-of-the-art aircraft such as the F-15 would have been desirable, it was felt that the uncertainty associated with obtaining sufficient data on such an aircraft was large enough to seriously jeopardize this relatively short-term effort.

The Charles Stark Draper Laboratory, Inc. (CSDL), with the cooperation of the Air Force, obtained both rigid-body and bending-mode data for a typical high-performance vehicle. The data were sufficient to allow the detailed modeling of the aircraft dynamics and bending modes (up to approximately 141 radians/second) in a real-time all-digital simulation. The availability of the bending-mode data is particularly important since it is anticipated that the aircraft system responses to the bending dynamics will be a primary contributor to the MIRA-system location sensitivity.

The overall MIRA program considers both fighter- and transport-type aircraft. The fighter application produces a more severe environment in terms of accelerations, angular rates, and vibrational excitation. Therefore, the limitation of this MIRA effort to a fighter-type aircraft does not significantly limit the utility of the results or the validity of the demonstration of the simulation capabilities.

The entire simulation is structured for ease of modification of the aircraft characteristics. It is felt that this capability is an important feature for the MIRA program, not only because of the general nature of the effort, but also because of the early point of maturity of the program. While the existing simulation utilizes a significant portion of the available computational resources, it is felt that simulations appropriate for state-of-the-art fighter or transport aircraft could be developed within the existing simulation structure.

## 2.2 Aircraft Definition

The data selected to define the vehicle were the most comprehensive that could be found so that the simulation developed would have a great deal of flexibility and applicability. For example, the rigid-body aerodynamic data defining the vehicle were developed from wind-tunnel data during a program investigating high angle-of-attack flight. The aerodynamics are available as nonlinear polynomial functions valid beyond the stall angle of attack and over a wide range of sideslip angles. This is well beyond the flight envelope needed for the MIRA program. The data are valid for a vehicle in the clean configuration in subsonic flight and available in Reference 1.

The aeroelastic data defining the structural modes and their effect on the vehicle sensor responses were obtained from References 2 and 3. Definition of the vehicle in the MIRA simulation includes three longitudinal and three lateral directional modes. Each mode is represented by a coupled linear second-order differential equation. The longitudinal modes of interest are the stabilator-bending mode, the first vertical-bending mode, and the stabilator-rotation mode. These modes were selected in References 2 and 3 because they involve strong fuselage-stabilator coupling. They are excited by the stabilator-control-system inputs and contribute significantly to the sensor responses. The nominal frequency of the highest mode is 141 radians/second. The lateral-directional modes included in the MIRA simulation are the fuselage first torsion mode, the wing first asymmetric-bending mode, and the fuselage first lateral-bending mode. The highest mode frequency is 80.8 radians/second. Also incorporated into the MIRA simulation is the effect of the aeroelastic modes on the sensor responses.

## 2.3 Flight-Control Definition

The flight-control system selected for primary consideration during the development phase of the MIRA simulation was designed for the Survivable Flight-Control System (SFCS) Program and is presented in Reference 2. This flight-control system was developed using the structural-mode data programmed in the simulation. Together, these two sets of data provide a consistent package. However, the flight-control system developed for the SFCS Program is much more sophisticated than needed for MIRA. It is an adaptive system valid over the whole flight

envelope of the vehicle. For the MIRA effort, the adaptive system was reduced to a fixed-gain system suitable for operation in the vicinity of a nominal flight condition.

The flight-control system incorporates conventional feedback loops to improve the handling qualities of the bare airframe. For example, the longitudinal system incorporates pitch-rate and normal-acceleration feedback to the stabilator. The lateral-directional system incorporates roll-rate feedback to the ailerons and yaw-rate and lateral-acceleration feedback to the rudder. A roll-to-yaw crossfeed network is also included for turn coordination.

During the course of the simulation development, a second longitudinal flight-control system was programmed into it. The system was obtained from Reference 4. However, it was not given major consideration during this phase of the MIRA effort since it was not well defined nor consistent with the aeroelastic data used, as in the case of the previously discussed system. However, this system is available in the non-real-time simulation should it be desired to exercise an alternate configuration.

#### 2.4 Future Aircraft and Flight-Control Capabilities

As previously mentioned, the basic simulation developed for the MIRA program is capable of accommodating a wide range of aircraft and flight-control configurations. Although the impact of the MIRA system on the flight-control system is not of primary concern, and a relatively straightforward stability-augmentation control system was developed for the first phase, the simulation is capable of supporting considerable sophistication in the flight-control area. Among potential flight-control developments consistent with the MIRA approach are control systems for Control Configured Vehicles (CCV), distributed and fault-tolerant control systems, and active bending-mode compensation. The simulation is capable of supporting these efforts so long as the control rates are maintained within a realistic range for avionics computers in the early 1980 time period.

In addition to the simulation developed under this effort, CSDL has a substantial amount of data on the KC-135 and F-8 aircraft. Although the F-8 may not be considered an appropriate aircraft for the MIRA effort, the KC-135 could serve as an appropriate model for the transport application of MIRA, thus minimizing the program dependence upon external data sources. The reduced dynamic environment (linear

and angular accelerations) of a transport application would allow reduction of the flight-control and environment-integration rates, and therefore a reduction in the overall simulator duty cycle.

Preliminary investigations were made during the course of this effort into obtaining the appropriate F-15 aircraft modeling data for upgrading the vehicle model to a state-of-the-art aircraft. At the current time, it appears that sufficient information is available from McDonnell Douglas Aircraft Corporation (McDAC) to allow modeling of the rigid-body dynamics of this aircraft, but not the flexible-body dynamics. Although there may be limited benefits in doing so, it would be possible to convert the rigid-body dynamics to an F-15 while using nominal (or possibly new) data for bending dynamics. This approach might allow closer correlation of the CSDL effort to the McDAC MIRA effort; however, it represents a relatively inefficient utilization of the simulation since the bending dynamics represent the highest rate computational load, and can have a significant impact upon the MIRA-system performance. Presently, the simulation developed under this contract can run in real time without the bending dynamics. A real-time simulation with bending dynamics will be available early in 1977 in the second phase of the MIRA effort.

Although the choice of aircraft model involves a wide variety of possible options, the utility of the existing model should not be underestimated. The dynamics are representative of a large class of fighter aircraft which are of interest, while exact aircraft characteristics are not very significant this early in the MIRA program. In addition, there is a large body of information available concerning the vehicle which may be useful for comparative tradeoff studies of potential MIRA configurations.

## 2.5 Inertial-Sensor Requirements for MIRA

### 2.5.1 Introduction

Perhaps the most disparate requirements for inertial sensors in a tactical aircraft are those imposed by inertial navigation on the one hand, and stability augmentation on the other. In the former case, long-term accuracy of the inertial components per se is the prime requisite. The data from the inertial sensors are digital and represent the integrals of both specific force and angular rate (in a strap-down inertial measuring unit (IMU)). In the latter case, accuracy



requirements on the inertial sensors are orders of magnitude less stringent. The data from the sensors are analog and represent the lateral and normal components of the specific force and angular rate about the roll, pitch, and yaw axes of the vehicle. In the absence of a separate inertial navigation system (INS), attitude and heading reference data are supplied by a two-axis free vertical gyro, and heading by a single-axis directional gyro.

For further tactical applications, the prime stability-augmentation sensors (i.e., the two accelerometers and three rate gyros) will be at least triply redundant. Hence, by the addition of a longitudinal accelerometer to each of the three sets of sensors, one has all the sensors requisite to a triply redundant strapdown IMU. Of course, the stability and accuracy of the individual sensors would have to be upgraded to be compatible with the inertial-navigation requirements.

The resulting configuration consisting of three-gyro-plus-three-accelerometer prealigned inertial-sensor assemblies could be distributed throughout the aircraft in positions approximating the optimum locations for the individual stability-augmentation sensors. It is obvious that this configuration contains the minimum number of components for a given degree of redundancy, and hence should be the prime-candidate configuration.

#### 2.5.2 Approach for Determining Sensor Characteristics

Determination of the characteristics of the inertial sensors which simultaneously satisfy the requirements of the stability-augmentation and the inertial-navigation systems necessitates a multi-stage approach. First, the stability-augmentation or flight-control-system sensor requirements are established from considerations of the vehicle dynamics, e.g., maximum roll rate and normal acceleration, the natural frequency and damping ratio of the typical (analog) rate-gyro and accelerometer loops, and the threshold and linearity of the outputs. It may then be necessary to reinterpret the servo characteristics in the time domain as time delays. Next, the INS requirements imposed by target acquisition, fire control and/or weapon delivery are considered, and the necessary position, velocity, attitude and heading, and angular-rate accuracies are determined. Other factors include reaction time, radio-navigation aids, and air-data system. The range of INS parameter accuracies is tabulated and typical requirements are formulated. The INS requirements are interpreted in terms of inertial-component

performance, stability-augmentation requirements are superimposed, and the literature is searched for systems and/or components which satisfy these composite requirements. Finally, dynamic and performance models of the inertial components which satisfy the composite requirements are found or constructed for use in the system simulation. It should be acknowledged at the outset that it is impractical to consider mechanizing the integration of the exact equations of motion of the accelerometer pendulum, which has a time constant ranging from a few microseconds to a few hundred microseconds, while the natural frequency of the stability-augmentation-system outer loops is on the order of 1 hertz, and the natural frequency of the INS is 0.0002 hertz. Interest in the dynamic sensor performance extends only to frequencies on the order of 20 hertz.

### 2.5.3 Inertial-Sensor Requirements for Stability Augmentation

The stability-augmentation sensors are the normal and lateral accelerometers and the roll, pitch, and yaw rate gyros. These instruments provide analog voltage outputs proportional to specific force and angular rate respectively. Restoring force (torque) may be provided electrically or mechanically, or by a combination of both. Bandwidth of the loops need only be sufficient to ensure that positive feedback at the dominant structural modes does not occur. Sensitivity to structural vibrations within the passband is reduced by notch filters at the inputs to the stability-augmentation system.

Tentative characteristics of analog accelerometer and rate-gyro loops are given in Tables 2-1 and 2-2. Both loops are essentially second-order low-pass filters, i.e., the transfer functions are of the form

$$T = \frac{K}{s^2 + 2\zeta\omega_n s + \omega_n^2} \quad (2-1)$$

Table 2-1. Characteristics of flight-control accelerometers for MIRA.

Parameter	Value
Range	±10 g
Threshold	0.01 g
Natural Frequency	15 to 30 Hz
Damping Ratio	0.6 to 0.9
Linearity	0.5% of full scale
Output*	0.5 V/g

\* Normal accelerometer.

Table 2-2. Characteristics of flight-control rate gyros for MIRA.

Parameter	Value
Range	±400 deg/s
Threshold	±0.1 deg/s
Natural Frequency	15 to 30 Hz
Damping Ratio	0.6
Linearity	0.25% of full scale
Output*	0.125 V/deg/s

\* Roll rate gyro.

The resulting time delay is of interest when one considers mechanizing a digital stability-augmentation or flight-control system. The phase angle,  $\phi(\omega)$ , of the output is given by

$$\phi(\omega) = \tan^{-1} \left[ \frac{2\zeta \frac{\omega}{\omega_n}}{1 - \left(\frac{\omega}{\omega_n}\right)^2} \right] \quad (2-2)$$

And the time delay, of the filter as a function of frequency,  $t_d(\omega)$ , is the slope of the phase curve

$$t_d(\omega) = \frac{d\phi(\omega)}{d\omega} = \frac{\frac{2\zeta}{\omega_n} \left[ 1 + \left(\frac{\omega}{\omega_n}\right)^2 \right]}{\left[ 1 - \left(\frac{\omega}{\omega_n}\right)^2 \right]^2 + \left( \frac{2\zeta\omega}{\omega_n} \right)^2} \text{ seconds} \quad (2-3)$$

For median values of the filter parameters, i.e.,  $\zeta = 0.707$  and  $\omega_n = 130$  radians/second, the time-delay curve is shown in Figure 2-1. Over the range of frequencies corresponding to the fundamental structural resonances (6 to 14 hertz), the time delay is seen to be 12 to 13 milliseconds.

Bearing in mind that the outputs of the INS sensors are incremental velocities and angles, and hence need to be differentiated, the above considerations would require a minimum sampling frequency of 40 to 50 times per second for equivalent performance.

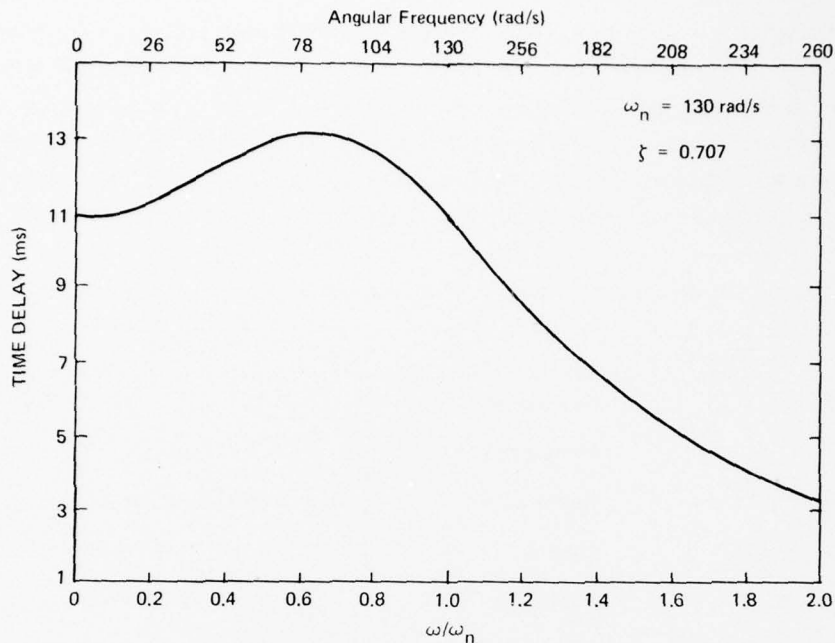


Figure 2-1. Time delay for second-order low-pass filter.

#### 2.5.4 INS Requirements for Tactical Applications

A brief survey of the INS-related requirements for advanced tactical aircraft displays a rather narrow range of acceptable position and velocity errors, but a much wider range of tolerable attitude and attitude (or body) rate errors. In some cases, the accuracy requirements mandate the use of position and velocity resets just prior to target acquisition. In other cases, the pointing and tracking requirements could not be met even by an aided INS. Disregarding the most stringent requirements, the ranges of acceptable INS accuracies are tabulated in Table 2-3. From the data of Table 2-3, a set of typical INS performance requirements is summarized in Table 2-4. The indicated position-error rate corresponds to uncompensated gyro-drift rates on the order of 0.01 degree/hour. The latter would produce an initial azimuth misalignment of about 1.0 milliradian, at 40 degrees latitude with perfect accelerometers. In a gimballed platform, the gyro-drift, accelerometer, and initial-alignment errors, which are correlated at entry into the navigation mode, will remain correlated during the mission. For a strapdown system this is not the case, and the error



propagation will be strongly mission-dependent. Generally, the strap-down INS navigation and attitude errors will be considerably larger than those in a gimballed INS with the same inertial components due to the vastly greater angular rates encountered. Gyro misalignment and scale-factor errors are also greatly amplified by these higher angular rates. In a strapdown system, an accelerometer bias of 100  $\mu\text{g}$  could quite easily produce a peak-velocity error in excess of 3.0 knots.

Table 2-3. INS accuracy ranges for advanced tactical applications.

Parameter		Value
Position	Horizontal <sup>(1)</sup>	0.5 to 1.0 nmi/h (CEP)
	Vertical <sup>(2)</sup>	167 to 200 ft
Velocity <sup>(3)</sup>	Each Axis	3.0 to 5.0 kn
Attitude <sup>(4)</sup>	Level	0.25 to 6.0 mrad
	Heading	0.86 to 20.6 $\widehat{\text{min}}$
Attitude Rate	Each Axis	0.15 to 1.0 mrad/s
Body Rate	Each Axis	0.0086 to 0.057 deg/s

(1) May require position/velocity updating near target.

(2) Inertial plus air-data errors.

(3) Not rms, but instantaneous errors. For some applications 1 knot is not enough.

(4) Heading error is greater than level errors.

Table 2-4. Typical INS requirements from target-acquisition, weapon-delivery, and fire-control requirements.

Parameter		Value
Position	Horizontal	0.7 nmi/h (CEP)
	Vertical	180 ft*
Velocity	Each Axis	4.0 kn**
Attitude	Level	4.0 $\widehat{\text{min}}$ **
	Heading	6.0 $\widehat{\text{min}}$ **
Attitude Rate	Each Axis	0.02 deg/s**

\* Includes effects of nonstandard lapse rate.

\*\* 1 $\sigma$  values at target acquisition.

With these considerations in mind, existing and proposed strapdown systems and/or components were surveyed in an effort to find systems or components with demonstrated capability of meeting both the performance and the dynamic requirements of advanced tactical missions. Failing this, systems or components with suitable demonstrated laboratory performance in developmental quantities might be considered.

Before attempting to summarize strapdown-system performance, it is useful to tabulate the more physical characteristics (e.g., size, weight, power) and cost, MTBF, etc. of a typical strapdown INS from the survey. These results are given in Table 2-5.

Table 2-5. Typical strapdown INS characteristics.

Parameter	Value
Volume	<1000 in. <sup>3</sup>
Weight	<30 lb
Power - Peak	<250 W
Operating	<100 W
Cost in Production Quantities	<\$30,000
MTBF	>3000 h
Acceleration	≥10 g
Angular Rate	≥300 deg/s

From the characteristics in Table 2-5, it is seen that the physical and cost characteristics of the typical strapdown INS are generally compatible with the intended application. However, the level of performance is very environment sensitive, and ranges from 0.6 to 4.0 nautical miles/hour (CEP). Furthermore, the initial-alignment method and reaction time are frequently unspecified. It should be noted that the reaction time for tactical applications is normally 10 minutes or less.

Table 2-5 is representative of the future class of strapdown systems comprising floated rate integrating gyros, tuned rotor gyros, laser gyros, ESGs, and even multisensors. It is representative of proposed

systems and those of which a limited number have been built. Each of these sensors has its claimed advantages and disadvantages, but it is clear that the multisensors would offer the minimum number of components required to perform three-axis rate and specific-force measurement. For the purposes of demonstrating the MIRA simulation, however, laser gyros were chosen as the initial rate sensors to be modeled, and single-degree-of-freedom accelerometers as the specific-force measuring devices.

The incremental velocity/linear acceleration sensors, in the strapdown systems surveyed, are generally of the pendulous single-axis type, with an analog rebalance loop and subsequent conversion to digital format (either direct or voltage-to-pulse rate and summation). The most common accelerometer is the Sunstrand (Q-Flex), which is a quartz flexure hinged-pendulum device with adequate range and performance. One disadvantage of trying to recover instantaneous acceleration from the incremental velocity (digital output) of the accelerometer is the fact that the quantization tends to be on the order of 0.032 foot/second/pulse or 1,000 pulses/second/g which militates against the recovery of instantaneous acceleration, i.e., with acceptably small time delay. However, separate processing of the analog output could yield the desired acceleration with negligible delay.

#### 2.2.5 Minimum Sensor Configuration

It is expected that during the 1980 time frame, triply redundant sensor systems will be standard on advanced tactical fighters. Therefore, the minimum sensor configuration would consist of three strapdown systems, each located at different fuselage stations in the aircraft. These would be FS 77, FS 186, and FS 383 for the simulation vehicle, which are considered the optimum locations for the normal accelerometer and roll rate gyro, the lateral accelerometer, and the pitch and yaw rate gyros respectively. Thus, when all components are operating, there would be one stability-augmentation sensor of each kind in its optimum location (master) plus two backup sensors in nonoptimum locations. Presumably, filtering would be applied to the outputs of the sensors; at least those in the nonoptimum locations to minimize the differences in indicated outputs relative to the masters. Lever-arm corrections would certainly have to be applied for at least two thirds of the sensors.

At each of the three locations, a complete strapdown IMU (and possibly its own navigation computer) would be mounted. Preprocessing of the stability-augmentation signals would also be performed at these locations either in an existing navigation computer or separate micro-processor(s).

The signals would be mixed and the stability-augmentation/flight-control computations would be performed in one (or more) centralized computer(s), which would provide the actuator signals.

Radio navigation aids, air data (with the possible exception of barometric altitude), and the navigation and attitude data from the three strapdown INS would be processed in the same (or other) computer(s) to provide "best" estimates of the navigation-data and navigation-parameter updates. The various pointing, tracking, fire-control, weapon-delivery, and display computations would likely be performed in this computer complex also.



## SECTION 3

### MIRA SIMULATION DEVELOPMENT

#### 3.1 Introduction

A major goal of the present program is the development of a simulation capability to evaluate the MIRA concept. In addition, the capability of the simulation is to be demonstrated. This section describes the simulation, and details the assumptions made in generating it, as well as the models, equations, and data programmed. A presentation of the data obtained from the use of the simulator and a discussion of the corresponding results follows in Section 4.

The simulation goals of the MIRA project can be achieved in several different ways. A series of simulator goals have been established which will provide the maximum long-term benefit to the program and concept evaluation. One of these goals is the development of a real-time simulation which will lessen computer operating costs and allow human interaction with the system. A fixed-base cockpit has been tied into the system allowing pilot evaluation of the candidate MIRA configurations prior to flight test. Another CSDL simulation goal is the development of an all-digital simulation capability. There are many factors which make an all-digital simulation most attractive when compared to a system utilizing analog computers. Among them are ease of setup, repeatability, reliability, etc. A third feature, incorporated into the MIRA simulation, is flexibility. Provisions have been, and will continue to be, included in the simulation which allows ease of change of parameters, sensor configurations, sensor locations, program subroutines and models, aircraft aerodynamics, and (in general) almost any portion of the simulation. The long-term benefit of each of these goals to the MIRA program is clearly evident.

The MIRA simulation utilizes a Xerox Data System Model (XDS) 9300 general-purpose digital computer as the basic computation unit. This machine has a 32,768-word magnetic core memory, 24-bit word length, and

1.75-microsecond machine cycle time. In the near future, this computation capability will be expanded by interfacing two Honeywell 124-series digital computers with the XDS 9300 to operate as parallel processors. One of these units is a basic 124 expanded to a Honeywell 224 memory configuration of 16k words, while the other unit is a basic 124 with 8k words of memory.

The basic program plan calls for the development of a non-real-time version of the MIRA simulation, programmed in Fortran on the XDS 9300, for purposes of checkout and to obtain preliminary data and results. This same simulation capability is to be expanded to real-time operation using fixed-point assembly language. The 124 computers are needed for this phase of the operation. At present, the evolution of the non-real-time simulation has been completed. The conversion of this simulation to real-time operation has begun, but only includes the rigid-body equations of motion of the vehicle at this point. The next step in the program involves bringing the real-time simulation capability up to the level of the non-real-time simulation.

### 3.2 General Description of MIRA Simulation Characteristics

A block diagram of the system programmed in the non-real-time simulation is presented in Figure 3-1. The nonlinear six-degree-of-freedom equations of motion of the vehicle have been programmed. A spherical rotating earth model is used. The aerodynamics incorporated into the simulation are valid for a cleanly configured vehicle in subsonic flight. More specifically, the aerodynamics are programmed as nonlinear polynomial functions valid over an envelope of  $\pm 15$  degrees in sideslip angle, and up to 30 degrees in angle of attack. This large envelope allows a great deal of flexibility in the use of the simulation, without any extensive reprogramming.

Three longitudinal and three lateral-directional structural modes have been added to the rigid-body equations of motion. A stability and control augmentation system has also been included to improve the handling qualities of the vehicle. Structural-mode filters are also included in the augmentation system. It is possible to enter time-history profiles into the simulation to generate typical aircraft maneuvers. The effects of winds and turbulence on the vehicle are another feature of the simulation.

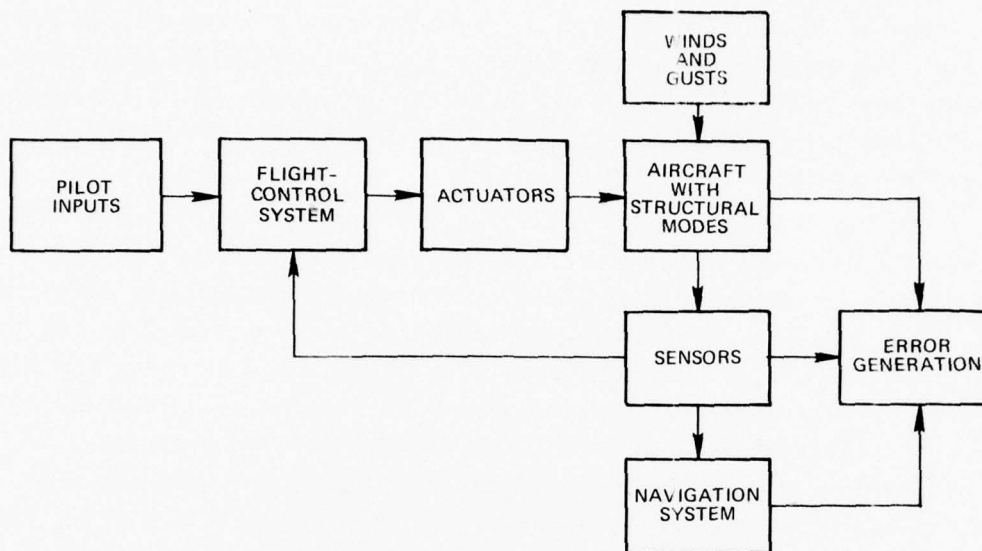


Figure 3-1. MIRA simulation block diagram.

Models of flight-control sensors, and navigation-system laser rate gyros and quartz-flexure accelerometers are incorporated into the MIRA simulation. It is possible to independently locate each of these sensors, and to use the navigation sensors for flight control. An onboard Local Vertical Wander Azimuth (LVWA) navigation-system model has also been programmed. This model was obtained from the Standardized Software Development Program.<sup>(5)\*</sup> Errors between vehicle and navigation-system parameters are also generated for the purpose of evaluating different MIRA configurations. A detailed discussion of each of these aspects of the MIRA simulation is presented in the following sections of the report so that a better understanding of its overall capability can be obtained.

One flight condition has been selected for development, demonstration, and evaluation of the MIRA simulation capability. The vehicle is at an altitude of 5,000 feet and Mach 0.5. The trim velocity is 549 feet/second, and the trim angle of attack is 2.06 degrees. Selection of this point in the flight envelope was dictated primarily by the fact

\* Superscript numerals refer to similarly numbered items in the List of References.

that consistent data are available for each portion of the simulation at this flight condition, while simultaneously allowing the goals of the MIRA program to be satisfied. The availability of time histories, vehicle-model parameters, and other data useful for system checkout, also dictated the choice of this flight condition as the nominal one. The reader is cautioned that some of the data given in this report apply specifically to the nominal flight condition, and will have to be modified should another flight condition be considered.

### 3.3 Vehicle Six-Degree-of-Freedom Nonlinear Equations of Motion

This section contains a development of the six-degree-of-freedom nonlinear equations of motion of the vehicle. The development closely follows that given in Reference 6.

Four orthogonal-axes systems must be defined to develop the appropriate equations of vehicle motion. They are depicted in Figures 3-2, 3-3, and 3-4, and are defined as:

- (1) The inertial frame which is taken as fixed in space, and for which Newton's Laws of Motion are valid.
- (2) An earth-centered frame which rotates with the earth.
- (3) An earth-surface frame which is parallel to the earth's surface, and whose origin is at the vehicle's center of gravity (cg) defined in north, east, and down directions. This frame moves with the vehicle, and its center is defined with respect to the earth-centered frame by the longitude, latitude, and altitude of the vehicle.
- (4) The conventional body axes are selected to represent the vehicle. The center of this frame is at the cg of the vehicle and its components are forward, out of the right wing, and down.

Several major assumptions have been made in the basic development of the vehicle equations of motion. These assumptions are:

- (1) The vehicle equations are written in the body-axes coordinate frame.
- (2) A spherical earth rotating at a constant angular velocity is assumed.
- (3) The vehicle aerodynamics are nonlinear.



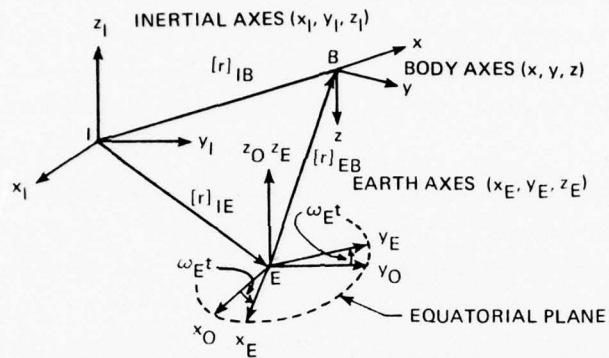


Figure 3-2. Inertial, earth, and body coordinate systems.

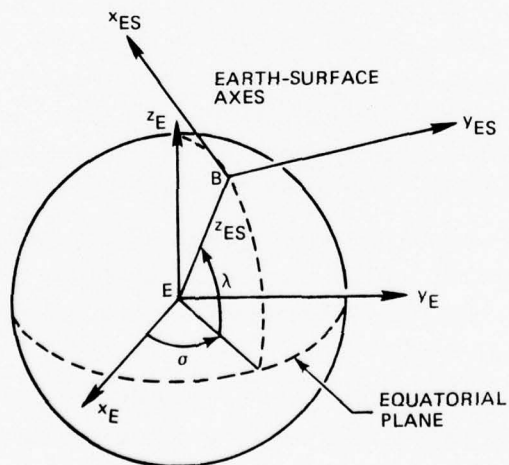


Figure 3-3. Coordinates for relative motion over the earth.

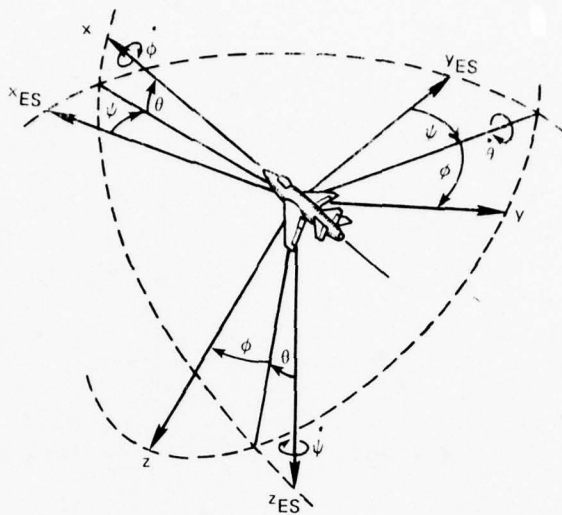


Figure 3-4. Orientation angles.

- (4) The undisturbed atmosphere rotates with the earth.
- (5) The winds are defined with respect to the earth.
- (6) The gusts are defined with respect to the vehicle.
- (7) An inverse-square gravitational law is used for the spherical-earth model.
- (8) The mass of the vehicle is constant.
- (9) Flight over the poles is excluded due to the use of latitude as a variable.
- (10) The gradients of the low-frequency winds are small enough to be neglected.

Other assumptions which have been made during the development of the MIRA simulation are mentioned as they arise during the discussion.

The force equations of the vehicle, with respect to the inertial reference, are given in vector form as:

$$[\dot{\mathbf{V}}] = \frac{1}{m} [\mathbf{F}] - [\omega \chi] \cdot [\mathbf{V}] \quad (3-1)$$

while the moment equations are written as

$$[\mathbf{I}] [\dot{\omega}] = [\mathbf{M}] - [\omega \chi] [\mathbf{I}] [\omega] \quad (3-2)$$

where

$$\begin{aligned}
 [V] &= \begin{bmatrix} u \\ v \\ w \end{bmatrix}, \quad [\omega] = \begin{bmatrix} p \\ q \\ r \end{bmatrix}, \quad [F] = \begin{bmatrix} F_x \\ F_y \\ F_z \end{bmatrix} \\
 [M] &= \begin{bmatrix} M_x \\ M_y \\ M_z \end{bmatrix}, \quad [I] = \begin{bmatrix} I_x & 0 & -I_{xz} \\ 0 & I_y & 0 \\ -I_{xz} & 0 & I_z \end{bmatrix} \\
 [\omega\chi] &= \begin{bmatrix} 0 & -r & q \\ r & 0 & -p \\ -q & p & 0 \end{bmatrix} \quad (3-3)
 \end{aligned}$$

Expansion of these vector equations leads to the following familiar scalar equations.

$$\dot{u} = \frac{F_x}{m} + rv - qw \quad (3-4)$$

$$\dot{v} = \frac{F_y}{m} - ru + pw \quad (3-5)$$

$$\dot{w} = \frac{F_z}{m} + qu - pv \quad (3-6)$$

$$\dot{p} = \frac{1}{I_x} \left[ I_{xz} \dot{r} + qr(I_y - I_z) + pqI_{xz} + M_x \right] \quad (3-7)$$

$$\dot{q} = \frac{1}{I_y} \left[ I_{xz} (r^2 - p^2) + pr(I_z - I_x) + M_y \right] \quad (3-8)$$

$$\dot{r} = \frac{1}{I_z} \left[ I_{xz} \dot{p} - I_{xz} qr + (I_x - I_y) pq + M_z \right] \quad (3-9)$$

The vehicle force vector may be further defined in terms of the aerodynamic structural mode and gravitational forces, and the thrust of the right and left engines as

$$[F] = [F_{aero}] + [F_{grav}] + [F_{SM}] + [F_{TR}] + [F_{TL}] \quad (3-10)$$

The aerodynamic force vector is defined as

$$[F_{aero}] = \bar{q}S \begin{bmatrix} C_x \\ C_y \\ C_z \end{bmatrix} \quad (3-11)$$

where  $\bar{q} = \frac{1}{2} \rho V_A^2$ . The gravitational force vector is given by

$$[F_{\text{grav}}] = [T_{\text{ESB}}] \begin{bmatrix} 0 \\ 0 \\ mg \end{bmatrix} = mg \begin{bmatrix} -\sin \theta \\ \sin \phi \cos \theta \\ \cos \phi \cos \theta \end{bmatrix} \quad (3-12)$$

An inverse-square law is used to compute  $g$ , i.e.,

$$g = g_0 \left( \frac{R_0}{R_E} \right)^2 \quad (3-13)$$

The force components due to the engine thrust and the structural modes are developed in more detail in a latter section. Expansion of the force vector results in the following scalar equations.

$$F_x = \bar{q} S C_{x_0} - mg \sin \theta + F_{R_x} + F_{L_x} + F_{SM_x} \quad (3-14)$$

$$F_y = \bar{q} S C_{y_0} + mg \sin \phi \cos \theta + F_{R_y} + F_{L_y} + F_{SM_y} \quad (3-15)$$

$$F_z = \bar{q} S C_{z_0} + mg \cos \phi \cos \theta + F_{R_z} + F_{L_z} + F_{SM_z} \quad (3-16)$$

The vehicle moment vector may also be defined in terms of the aerodynamic structural mode and thrust moments as

$$[M] = [M_{\text{aero}}] + [M_{T_R}] + [M_{T_L}] + [M_{SM}] \quad (3-17)$$

$[M_{\text{aero}}]$  is given by

$$[M_{\text{aero}}] = \bar{q} S \begin{bmatrix} b C_{\ell} \\ \bar{c} (C_m - C_z \Delta c g) \\ b (C_n + C_y \Delta c g \frac{\bar{c}}{b}) \end{bmatrix} \quad (3-18)$$

where

$$\Delta c g = c g_{\text{pos}} - 0.33 \quad (3-19)$$

The incremental terms,  $C_z \Delta c g$  subtracted from  $C_m$  and  $C_y \Delta c g \frac{\bar{c}}{b}$  added to  $C_n$ , account for the location of the aircraft  $c g$  at a position different from the nominal value of  $0.33 \bar{c}$ , at which the aerodynamic data are defined. A development of the thrust and structural-mode moments is detailed in a later section of this discussion. However, the moment vector can be expanded in terms of the components of these vectors as

$$M_x = \bar{q} S b C_{\ell} + M_{R_x} + M_{L_x} + M_{SM_x} \quad (3-20)$$



$$M_Y = \bar{q} S \bar{C} (C_m - C_z \Delta c g) + M_{R_Y} + M_{L_Y} + M_{SM_Y} \quad (3-21)$$

$$M_Z = \bar{q} S b \left( C_n + C_Y \Delta c g \frac{\bar{C}}{b} \right) + M_{P_Z} + M_{L_Z} + M_{SM_Z} \quad (3-22)$$

The aerodynamic forces and moments are computed using the total velocity of the aircraft cg relative to the local atmosphere, which is given by

$$V_A = \left( V_{A_x}^2 + V_{A_y}^2 + V_{A_z}^2 \right)^{1/2} \quad (3-23)$$

The vector equation for the body-axes velocity with respect to the local atmosphere is

$$[V_A] = [V_{rel}] - [V_{wind}] - [V_{gust}] \quad (3-24)$$

In terms of the x, y, and z components of each of these vectors, the atmosphere relative-velocity components are defined by

$$V_{A_x} = u_{rel} - u_{wind} - u_g \quad (3-25)$$

$$V_{A_y} = v_{rel} - v_{wind} - v_g \quad (3-26)$$

$$V_{A_z} = w_{rel} - w_{wind} - w_g \quad (3-27)$$

where  $u_{rel}$ ,  $v_{rel}$ , and  $w_{rel}$  are the linear body-axes components of the velocity of the aircraft cg with respect to the earth-centered frame. They are the difference between the body-axes components of the linear inertial velocities and the linear earth velocities, i.e.,

$$[V_{rel}] = [V] - [V_{EI}] \quad (3-28)$$

$$[V_{EI}] = [T_{ESB}] [V_E] \quad (3-29)$$

or

$$\begin{bmatrix} u_{rel} \\ v_{rel} \\ w_{rel} \end{bmatrix} = \begin{bmatrix} u \\ v \\ w \end{bmatrix} - [T_{ESB}] \begin{bmatrix} 0 \\ R_E \omega_E \cos \lambda \\ 0 \end{bmatrix} \quad (3-30)$$

The winds are defined with respect to the earth with components emanating from the north, east, and below the vehicle. Thus, a north wind blows from north to south, etc. The body-axes wind components are then given by

$$[V_{\text{wind}}] = [T_{\text{ESB}}][W] \quad (3-31)$$

or

$$\begin{bmatrix} u_{\text{wind}} \\ v_{\text{wind}} \\ w_{\text{wind}} \end{bmatrix} = [T_{\text{ESB}}] \begin{bmatrix} -N_{\text{wind}} \\ -E_{\text{wind}} \\ -D_{\text{wind}} \end{bmatrix} \quad (3-32)$$

Angle of attack and sideslip angle are used in the definition of the vehicle aerodynamics. These variables are given by the expressions

$$\alpha = \tan^{-1} \left( \frac{V_{A_z}}{V_{A_x}} \right) \quad (3-33)$$

$$\beta = \sin^{-1} \left( \frac{V_{A_y}}{V_A} \right) \quad (3-34)$$

The angular velocities of the vehicle with respect to the local atmosphere also have to be computed for the vehicle aerodynamics. They, however, do not turn out to be as complicated as the linear velocities with respect to the local atmosphere. The assumption that the spatial gradients of the low-frequency winds are small enough to be neglected, implies that the angular components of the wind can be neglected. A similar assumption is made regarding the angular velocities of the gusts. The overall result is that the angular velocities of the body axes with respect to the atmosphere are the angular velocities of the body axes with respect to the earth. They are given by the angular velocities of the body axes with respect to inertial space, less the angular velocities of the earth-centered frame with respect to the inertial reference in the body-axes coordinate system. In equation form, the result is

$$[\omega_A] = [\omega_{\text{rel}}] = [\omega] - [\omega_{\text{EI}}] \quad (3-35)$$

where

$$[\omega_{\text{EI}}] = [T_{\text{ESB}}][\omega_E] \quad (3-36)$$

$$\text{or} \quad [\omega_A] = \begin{bmatrix} p_A \\ q_A \\ r_A \end{bmatrix} = \begin{bmatrix} p_{\text{rel}} \\ q_{\text{rel}} \\ r_{\text{rel}} \end{bmatrix} = \begin{bmatrix} p \\ q \\ r \end{bmatrix} - [T_{\text{ESB}}] \begin{bmatrix} \omega_E \cos \lambda \\ 0 \\ -\omega_E \sin \lambda \end{bmatrix} \quad (3-37)$$

It is necessary to compute the variable  $\dot{\alpha}$ , since the coefficient  $M_{\dot{\alpha}}$  is present in the aerodynamics of the vehicle, and strongly affects its short-period response. Several techniques can be used to obtain  $\dot{\alpha}$ .

One is by back-differencing  $\alpha$ . This is an unacceptable method when high-frequency components are present in the  $\alpha$  response, such as due to structural modes and/or gusts. An alternate technique is to compute  $\dot{\alpha}$  from the expression

$$\dot{\alpha} = \frac{d}{dt}\alpha = \frac{d}{dt} \tan^{-1} \left( \frac{V_{A_z}}{V_{A_x}} \right) \quad (3-38)$$

$$= \frac{\dot{V}_{A_z} V_{A_x} - \dot{V}_{A_x} V_{A_z}}{V_{A_z}^2 + V_{A_x}^2} \quad (3-39)$$

Use of this latter expression presents an additional problem in that it necessitates the computation of  $\dot{V}_{A_x}$  and  $\dot{V}_{A_z}$ . These latter variables can be obtained from the vector differentiation of Eq. (3-24). However, fairly complicated expressions result. Simplifications to the true expressions for  $\dot{V}_{A_x}$  and  $\dot{V}_{A_z}$  are discussed in Reference 6. It is shown that an acceptably accurate solution for  $\dot{V}_{A_x}$  and  $\dot{V}_{A_z}$  may be obtained if it is assumed that the earth is rotating slowly, and that these acceleration variables are used only to compute  $\dot{\alpha}$  and not integrated to obtain  $V_{A_x}$ ,  $V_{A_z}$ , or  $\alpha$ . Neither of these assumptions is prohibitive in this particular case.

The expression resulting from the vector differentiation of Eq. (3-24), and the incorporation of the assumptions just discussed is

$$[\dot{V}_A] = [\dot{V}] + [\omega_{rel} \chi] [T_{ESB}]^{-1} \{ [V_E] + [W] - [\dot{V}_{gust}] \} \quad (3-40)$$

It is indicated in Reference 6 that the effect of the gusts on the terms of the previous expression is only on the order of 10 percent, and that neglecting  $[\dot{V}_{gust}]$  will not cause serious errors. This assumption is made in the MIRA simulation since it is desired to avoid the differentiation of the gust signals. The matrix equation for the components of  $[\dot{V}_A]$  are then given by

$$\begin{bmatrix} \dot{V}_{A_x} \\ \dot{V}_{A_y} \\ \dot{V}_{A_z} \end{bmatrix} = \begin{bmatrix} \dot{u} \\ \dot{v} \\ \dot{w} \end{bmatrix} + \begin{bmatrix} 0 & -r_{rel} & q_{rel} \\ r_{rel} & 0 & -p_{rel} \\ -q_{rel} & p_{rel} & 0 \end{bmatrix} [T_{ESB}]^{-1} \left\{ \begin{bmatrix} 0 \\ R_E \omega_E \cos \lambda \\ 0 \end{bmatrix} + \begin{bmatrix} -N_{wind} \\ -E_{wind} \\ -D_{wind} \end{bmatrix} \right\} \quad (3-41)$$

$$\begin{bmatrix} \dot{V}_{A_x} \\ \dot{V}_{A_y} \\ \dot{V}_{A_z} \end{bmatrix} = \begin{bmatrix} \dot{u} \\ \dot{v} \\ \dot{w} \end{bmatrix} + \begin{bmatrix} 0 & -r_{rel} & q_{rel} \\ r_{rel} & 0 & -p_{rel} \\ -q_{rel} & p_{rel} & 0 \end{bmatrix} \left\{ \begin{bmatrix} u_{EI} \\ v_{EI} \\ w_{EI} \end{bmatrix} + \begin{bmatrix} u_{wind} \\ v_{wind} \\ w_{wind} \end{bmatrix} \right\} \quad (3-42)$$

The specific expressions programmed are

$$\dot{V}_{A_x} = \dot{u} - r_{rel}(v_{EI} + v_{wind}) + q_{rel}(w_{EI} + w_{wind}) \quad (3-43)$$

$$\dot{V}_{A_z} = \dot{w} - q_{rel}(u_{EI} + u_{wind}) + p_{rel}(v_{EI} + v_{wind}) \quad (3-44)$$

The motions of the vehicle relative to the earth (the trajectory kinematics) are described by the motion of the earth-surface axes. The earth relative velocities are given by

$$[\dot{X}] = [T_{ESB}]^{-1}[V] - [V_E] \quad (3-45)$$

$$\begin{bmatrix} \dot{X} \\ \dot{Y} \\ \dot{Z} \end{bmatrix} = [T_{ESB}]^{-1} \begin{bmatrix} u \\ v \\ w \end{bmatrix} - \begin{bmatrix} 0 \\ R_E \omega_E \cos \lambda \\ 0 \end{bmatrix} \quad (3-46)$$

Making use of Eq. (3-30) leads to an alternate definition in terms of the vehicle velocities relative to earth, which is

$$\begin{bmatrix} \dot{X} \\ \dot{Y} \\ \dot{Z} \end{bmatrix} = [T_{ESB}]^{-1} \begin{bmatrix} u_{rel} \\ v_{rel} \\ w_{rel} \end{bmatrix} \quad (3-47)$$

The position of the vehicle is described by its latitude, longitude, and altitude. These quantities are obtained by integrating the earth velocities of the vehicle in spherical coordinates. The appropriate equations for integration are

$$\dot{h} = -\dot{Z} \quad (3-48)$$

$$\dot{\lambda} = \frac{\dot{X}}{R_E} \quad (3-49)$$

$$\dot{\sigma} = \frac{\dot{Y}}{R_E \cos \lambda} \quad (3-50)$$

An auxiliary variable, the flightpath angle  $\gamma$ , is defined as

$$\gamma = \sin^{-1} \frac{\dot{h}}{v_{rel}} \quad (3-51)$$



$$V_{rel} = \left( u_{rel}^2 + v_{rel}^2 + w_{rel}^2 \right)^{1/2} \quad (3-52)$$

The Euler angles defining the earth surface to body-axes transformation are defined in Figure 3-4 and obtained by integration of the following equations.

$$\dot{\phi} = \omega_x + \dot{\psi} \sin \theta \quad (3-53)$$

$$\dot{\theta} = \omega_y \cos \phi - \omega_z \sin \phi \quad (3-54)$$

$$\dot{\psi} = \omega_y \frac{\sin \phi}{\cos \theta} + \omega_z \frac{\cos \phi}{\cos \theta} \quad (3-55)$$

The angular velocity components of the vehicle about its body axes with respect to the earth-surface axes system ( $\omega_x$ ,  $\omega_y$ , and  $\omega_z$ ) are given by

$$\begin{bmatrix} \omega_x \\ \omega_y \\ \omega_z \end{bmatrix} = \begin{bmatrix} p_{rel} \\ q_{rel} \\ r_{rel} \end{bmatrix} - [T_{ESB}] \begin{bmatrix} \dot{\sigma} \cos \lambda \\ -\dot{\lambda} \\ -\dot{\sigma} \sin \lambda \end{bmatrix} \quad (3-56)$$

This expression is nothing more than the angular body rates of the vehicle with respect to the earth, less the angular rates of the earth-surface axes system with respect to the earth in body axes.

The transformation from the earth-surface axes system to the body-axes frame is achieved by a yaw, pitch, and roll about the longitudinal, lateral, and normal axes, respectively. The resultant matrix is

$$[T_{ESB}] = \begin{bmatrix} \cos \theta \cos \psi & \cos \theta \sin \psi & -\sin \theta \\ \sin \phi \sin \theta \cos \psi & \sin \phi \sin \theta \sin \psi & \sin \phi \cos \theta \\ -\cos \phi \sin \theta & +\cos \phi \cos \theta & \\ \cos \phi \sin \theta \cos \psi & \cos \phi \sin \theta \sin \psi & \cos \phi \cos \theta \\ +\sin \phi \sin \theta & -\sin \phi \cos \theta & \end{bmatrix} \quad (3-57)$$

### 3.4 Vehicle Aerodynamics

Expressions for the aerodynamic coefficients of the vehicle are presented in Reference 1 in polynomial form. These polynomials are functions of  $\dot{\alpha}$ ,  $\alpha$ ,  $\beta$ ,  $V_A$ , the body-axes angular rates relative to the atmosphere, and the aerodynamic control surfaces. The control surfaces consist of a combined spoiler and aileron deflection with 1.5 degrees of spoiler deflection for each degree of aileron deflection ( $\delta_a$ ), the horizontal tail or stabilator ( $\delta_e$ ), and the rudder ( $\delta_r$ ).

Expressions are available for three angle-of-attack ranges ( $\alpha \leq 15$  degrees,  $15 \text{ degrees} \leq \alpha \leq 30$  degrees, and  $30 \text{ degrees} \leq \alpha \leq 45$  degrees), since the intent of the study<sup>(1)</sup> was to identify the high angle-of-attack aerodynamic coefficients of the vehicle. The first two sets of these polynomials have been programmed into the MIRA simulation since the vehicle stalls at an angle of attack of approximately 23 degrees, and a definition beyond this boundary is felt to be unnecessary at this time. The aerodynamic expressions follow.

$\alpha$ -range:  $\alpha \leq 15^\circ$

$$\begin{aligned} C_x = & -0.0434 + 2.39 \times 10^{-3} \alpha + 2.53 \times 10^{-5} \beta^2 - 1.07 \times 10^{-6} \alpha \beta^2 \\ & + 9.5 \times 10^{-4} \delta_e - 8.5 \times 10^{-7} \delta_e \beta^2 \\ & + \bar{c}/(2V_A) \left\{ 8.73 \times 10^{-3} q_{rel} + 0.001 q_{rel} \alpha - 1.75 \times 10^{-4} q_{rel} \alpha^2 \right\} \end{aligned} \quad (3-58)$$

$$\begin{aligned} C_y = & -0.012\beta + 1.55 \times 10^{-3} \delta_r - 3 \times 10^{-6} \delta_r \alpha \\ & + b/(2V_A) \left\{ 2.25 \times 10^{-3} p_{rel} + 0.0117 r_{rel} - 3.67 \times 10^{-4} r_{rel} \alpha \right. \\ & \left. + 1.75 \times 10^{-4} r_{rel} \delta_e \right\} \end{aligned} \quad (3-59)$$

$$\begin{aligned} C_z = & -0.131 - 0.0538\alpha - 4.76 \times 10^{-3} \delta_e - 3.3 \times 10^{-5} \delta_e \alpha \\ & - 7.5 \times 10^{-5} \delta_a^2 \\ & + \bar{c}/(2V_A) \left\{ -0.111 q_{rel} + 5.17 \times 10^{-3} q_{rel} \alpha - 1.1 \times 10^{-3} q_{rel} \alpha^2 \right\} \end{aligned} \quad (3-60)$$

$$\begin{aligned} C_\ell = & -5.98 \times 10^{-4} \beta - 2.83 \times 10^{-4} \alpha \beta + 1.51 \times 10^{-5} \alpha^2 \beta \\ & - 6.1 \times 10^{-4} \delta_a - 2.5 \times 10^{-5} \delta_a \alpha + 2.6 \times 10^{-6} \delta_a \alpha^2 \\ & + 2.3 \times 10^{-4} \delta_r - 4.5 \times 10^{-6} \delta_r \alpha \\ & + b/(2V_A) \left\{ -4.12 \times 10^{-3} p_{rel} - 5.24 \times 10^{-4} p_{rel} \alpha \right. \\ & + 4.36 \times 10^{-5} p_{rel} \alpha^2 + 4.36 \times 10^{-4} r_{rel} + 1.05 \times 10^{-4} r_{rel} \alpha \\ & \left. + 5.24 \times 10^{-5} r_{rel} \delta_e \right\} \end{aligned} \quad (3-61)$$

$$\begin{aligned}
C_m = & -6.61 \times 10^{-3} - 2.67 \times 10^{-3}\alpha - 6.48 \times 10^{-5}\beta^2 \\
& - 2.65 \times 10^{-6}\alpha\beta^2 - 6.54 \times 10^{-3}\delta_e - 8.49 \times 10^{-5}\delta_e\alpha \\
& + 3.74 \times 10^{-6}\delta_e\beta^2 - 3.5 \times 10^{-5}\delta_a^2 \\
& + \bar{c}/(2V_A) \left\{ -0.0473q_{rel} - 1.57 \times 10^{-3}q_{rel}\alpha - 0.0273\dot{\alpha} \right. \\
& \left. - 0.87 \times 10^{-3}\dot{\alpha}\alpha \right\} \quad (3-62)
\end{aligned}$$

$$\begin{aligned}
C_n = & 2.28 \times 10^{-3}\beta + 1.79 \times 10^{-6}\beta^3 + 1.4 \times 10^{-5}\delta_a \\
& + 7.0 \times 10^{-6}\delta_a\alpha - 9.0 \times 10^{-4}\delta_r + 4.0 \times 10^{-6}\delta_r\alpha \\
& + b/(2V_A) \left\{ -6.63 \times 10^{-5}p_{rel} - 1.92 \times 10^{-5}p_{rel}\alpha \right. \\
& + 5.06 \times 10^{-6}p_{rel}\alpha^2 - 6.06 \times 10^{-3}r_{rel} - 8.73 \times 10^{-5}r_{rel}\delta_e \\
& \left. + 8.7 \times 10^{-6}r_{rel}\delta_e\alpha \right\} \quad (3-63)
\end{aligned}$$

$\alpha$ -range:  $15^\circ \leq \alpha \leq 30^\circ$

$$\begin{aligned}
C_x = & 0.141 - 0.0154\alpha + 2.96 \times 10^{-4}\alpha^2 - 3.72 \times 10^{-4}\beta^2 \\
& + 4.14 \times 10^{-5}\alpha\beta^2 - 9.12 \times 10^{-7}\alpha^2\beta^2 + 1.82 \times 10^{-3}\delta_e \\
& - 7.3 \times 10^{-5}\delta_e\alpha \\
& + \bar{c}/(2V_A) \left\{ -0.0602q_{rel} + 2.04 \times 10^{-3}q_{rel}\alpha \right\} \quad (3-64)
\end{aligned}$$

$$\begin{aligned}
C_y = & -2.08 \times 10^{-2}\beta + 6.07 \times 10^{-4}\alpha\beta + 2.37 \times 10^{-6}\beta^3 \\
& - 3.64 \times 10^{-7}\alpha\beta^3 + 2.3 \times 10^{-3}\delta_r - 5.9 \times 10^{-5}\delta_r\alpha \\
& + b/(2V_A) \left\{ -1.62 \times 10^{-3}p_{rel} + 3.32 \times 10^{-4}p_{rel}\alpha \right. \\
& + 0.0311r_{rel} - 1.4 \times 10^{-3}r_{rel}\alpha + 1.75 \times 10^{-4}r_{rel}\delta_e \left. \right\} \quad (3-65)
\end{aligned}$$

$$\begin{aligned}
C_z = & -0.608 - 0.022\alpha - 6.77 \times 10^{-3}\delta_e + 9.7 \times 10^{-5}\delta_e\alpha \\
& - 7.5 \times 10^{-5}\delta_a^2 \\
& + \bar{c}/(2V_A) \left\{ 1.136q_{rel} - 0.1418q_{rel}\alpha + 3.11 \times 10^{-3}q_{rel}\alpha^2 \right\} \quad (3-66)
\end{aligned}$$

$$\begin{aligned}
C_{\ell} = & -1.29 \times 10^{-2} \beta + 1.04 \times 10^{-3} \alpha \beta - 2.02 \times 10^{-5} \alpha^2 \beta \\
& + 1.36 \times 10^{-5} \beta^3 - 1.13 \times 10^{-6} \alpha \beta^3 + 2.01 \times 10^{-8} \alpha^2 \beta^3 \\
& - 7.74 \times 10^{-4} \delta_a + 1.9 \times 10^{-5} \delta_a \alpha + 2.0 \times 10^{-4} \delta_r \\
& - 5.0 \times 10^{-6} \delta_r \beta \\
& + b/(2V_A) \left\{ 2.78 \times 10^{-3} p_{rel} - 2.79 \times 10^{-4} p_{rel} \alpha - 6.81 \times 10^{-3} r_{rel} \right. \\
& \left. + 6.46 \times 10^{-4} r_{rel} \alpha + 5.24 \times 10^{-5} r_{rel} \delta_e \right\} \quad (3-67)
\end{aligned}$$

$$\begin{aligned}
C_m = & 0.0549 - 6.08 \times 10^{-3} \alpha - 1.69 \times 10^{-4} \beta^2 + 5.64 \times 10^{-7} \alpha \beta^2 \\
& - 8.14 \times 10^{-3} \delta_e + 1.1 \times 10^{-4} \delta_e \alpha - 3.5 \times 10^{-5} \delta_a^2 \\
& + \bar{c}/(2V_A) \left\{ -0.0951 q_{rel} + 1.4 \times 10^{-3} q_{rel} \alpha - 0.0479 \dot{\alpha} \right. \\
& \left. + 6.9 \times 10^{-4} \alpha \dot{\alpha} \right\} \quad (3-68)
\end{aligned}$$

$$\begin{aligned}
C_n = & 1.02 \times 10^{-2} \beta - 5.12 \times 10^{-4} \alpha \beta - 5.27 \times 10^{-6} \beta^3 \\
& + 3.79 \times 10^{-7} \alpha \beta^3 + 9.1 \times 10^{-5} \delta_a + 3.0 \times 10^{-6} \delta_a \alpha \\
& - 1.37 \times 10^{-3} \delta_r + 3.8 \times 10^{-5} \delta_r \alpha \\
& + b/(2V_A) \left\{ 0.0236 p_{rel} - 2.5 \times 10^{-3} p_{rel} \alpha + 6.25 \times 10^{-5} p_{rel} \alpha^2 \right. \\
& + 6.2 \times 10^{-4} r_{rel} - 4.89 \times 10^{-4} r_{rel} \alpha - 8.73 \times 10^{-5} r_{rel} \delta_e \\
& \left. + 8.7 \times 10^{-6} r_{rel} \alpha \delta_e \right\} \quad (3-69)
\end{aligned}$$

These data are valid only for a vehicle in the clean configuration; landing gear, flap effects, etc., are not accounted for. In addition, the aerodynamic model is valid only for subsonic flight with  $M = 0.7$  about the upper limit.

A few words of caution are in order concerning the use of these polynomials defining the aerodynamics of the vehicle. The transition between the angle-of-attack ranges is not smooth, and discontinuities are present at the boundaries for some of the variables. The time histories obtained for those cases where a transition from one angle-of-attack range to another exists may exhibit discontinuities. The implication of these unwanted and unrealistic responses should be investigated to assess their effect on the validity of the study being conducted.



### 3.5 Thrust Forces and Moments

Each of the force and moment equations contains thrust terms due to the fact that the engines are located on the sides of the fuselage and are inclined at an angle with respect to the vehicle body axes. As discussed in Reference 1, the orientation of the thrust is defined by two angles,  $\lambda_T$  and  $\phi_T$ . By definition,  $\lambda_T$  is the angle between the thrust vector and a line parallel to the x body axis, measured in a plane parallel to the x axis and containing the thrust vector; and  $\phi_T$  is the angle between the x-y plane and the plane parallel to the x axis, and containing the thrust vector. For the selected model,  $\lambda_T = 5.25$  degrees, and  $\phi_T = 87.28$  degrees. Solving for the thrust forces along the body axes by resolving vector components leads to the following expressions.

$$\begin{bmatrix} F_{T_R} \end{bmatrix} = \begin{bmatrix} F_{R_x} \\ F_{R_y} \\ F_{R_z} \end{bmatrix} = \begin{bmatrix} T_R \cos \lambda_T \\ -T_R \sin \lambda_T \cos \phi_T \\ -T_R \sin \lambda_T \sin \phi_T \end{bmatrix} = \begin{bmatrix} 0.9958 T_R \\ -0.00434 T_R \\ -0.0914 T_R \end{bmatrix} \quad (3-70)$$

$$\begin{bmatrix} F_{T_L} \end{bmatrix} = \begin{bmatrix} F_{L_x} \\ F_{L_y} \\ F_{L_z} \end{bmatrix} = \begin{bmatrix} T_L \cos \lambda_T \\ T_L \sin \lambda_T \cos \phi_T \\ -T_L \sin \lambda_T \sin \phi_T \end{bmatrix} = \begin{bmatrix} 0.9958 T_L \\ 0.00434 T_L \\ -0.0914 T_L \end{bmatrix} \quad (3-71)$$

The thrust moments are generated because the point of thrust application is offset from the vehicle cg. For the right engine, the point of application is defined by the following body-axes moment arms.

$$\Delta x_R = 0.608 + (cg_{pos} - 0.33)\bar{c} \text{ ft} \quad (3-72)$$

$$\Delta y_R = 1.985 \text{ ft} \quad (3-73)$$

$$\Delta z_R = -0.391 \text{ ft} \quad (3-74)$$

That is, the point of application is 0.608 foot in front of  $0.33 \bar{c}$  along the x body axis, 1.985 feet out the right wing along the y body axis, and 0.391 foot above the x-y plane along the z body axis. The increment  $(cg_{pos} - 0.33)\bar{c}$  in the  $\Delta x_R$  term accounts for cg location. For the left engine, the appropriate moment arms are

$$\Delta x_L = 0.608 + (cg_{pos} - 0.33)\bar{c} \text{ ft} \quad (3-75)$$

$$\Delta y_L = -1.985 \text{ ft} \quad (3-76)$$

$$\Delta z_L = -0.391 \text{ ft} \quad (3-77)$$

The expressions for the thrust moments using these moment arms, and the expressions for the thrust forces given previously are

$$\begin{bmatrix} M_{T_R} \end{bmatrix} = \begin{bmatrix} M_{R_x} \\ M_{R_y} \\ M_{R_z} \end{bmatrix} = \begin{bmatrix} -F_{R_y} \Delta z_R + F_{R_z} \Delta y_R \\ F_{R_x} \Delta z_R - F_{R_z} \Delta x_R \\ -F_{R_x} \Delta y_R + F_{R_y} \Delta x_R \end{bmatrix} \quad (3-78)$$

$$\begin{bmatrix} M_{T_L} \end{bmatrix} = \begin{bmatrix} M_{L_x} \\ M_{L_y} \\ M_{L_z} \end{bmatrix} = \begin{bmatrix} F_{L_z} \Delta y_L - F_{R_y} \Delta z_L \\ F_{L_x} \Delta z_L - F_{L_z} \Delta x_L \\ F_{L_y} \Delta x_L - F_{L_x} \Delta y_L \end{bmatrix} \quad (3-79)$$

### 3.6 Trim Algorithm

The MIRA simulation includes an automatic trim routine in which  $\alpha$ ,  $\beta$ ,  $\theta$ ,  $\psi$ , and the control deflections are calculated so that the vehicle body-axes accelerations and side and normal velocities with respect to the earth surface are ideally zero or, in the practical case, very small. An iterative scheme is used to adjust these parameters to the required trim values. Initialization of each of the sub-routines of the simulation also occurs during the automatic trim mode. The vehicle is always trimmed with wings level, so that if a crosswind is present the nose of the vehicle is turned into the wind at trim.

The section includes a brief discussion of the trim algorithm included in the MIRA simulation to present the basic ideas which it incorporates. A discussion of the initialization aspect of the simulation is not included since this is felt to be unnecessary, in addition to being very unwieldy.

A desired altitude and Mach number are selected for the vehicle, as well as initial estimates for the control deflections,  $\alpha$  and  $\beta$ . Then,  $V_{A_t}$  is computed from the speed of sound and Mach number by

$$V_{A_t} = V_s \cdot M \quad (3-80)$$

$V_{A_{x_t}}$ ,  $V_{A_{y_t}}$ , and  $V_{A_{z_t}}$  are then calculated.

$$v_{A_{z_t}} = v_{A_t} \tan \alpha_t \quad (3-81)$$

$$v_{A_{y_t}} = v_{A_t} \sin \beta_t \quad (3-82)$$

$$v_{A_{x_t}} = \left( v_{A_t}^2 - v_{A_{y_t}}^2 - v_{A_{z_t}}^2 \right)^{1/2} \quad (3-83)$$

The earth-relative linear velocities are then calculated from the aforementioned parameters using the equations

$$u_{rel_t} = v_{A_{x_t}} + u_{wind} + u_g \quad (3-84)$$

$$v_{rel_t} = v_{A_{y_t}} + v_{wind} + v_g \quad (3-85)$$

$$w_{rel_t} = v_{A_{z_t}} + w_{wind} + w_g \quad (3-86)$$

and  $p_{rel}$ ,  $q_{rel}$ , and  $r_{rel}$  are fixed at zero.

The trim pitch angle is chosen so that  $\dot{z} = 0.0$  by the formula

$$\theta_t = \tan^{-1} \left( \frac{w_{rel_t}}{u_{rel_t}} \right) \quad (3-87)$$

and the trim heading angle is chosen so that  $\dot{y} = 0.0$  by the formula

$$\psi_t = -\tan^{-1} \left( \frac{v_{rel_t}}{u_{rel_t}} \right) \quad (3-88)$$

Both of these expressions assume wings level flight so that  $\phi_t = 0.0$ . Furthermore, the expression for  $\psi_t$  assumes that  $\cos \theta_t \approx 1$ .

The vehicle equations of motion are used to calculate  $\dot{w}$ , and  $\alpha_t$  is adjusted so that  $\dot{w}_t = 0.0$ . An iterative scheme is used

$$\alpha_{t_k} = \alpha_{t_{k-1}} + 0.0003\dot{w} \quad (3-89)$$

until  $\dot{w}_t$  is sufficiently small. A similar scheme is used to zero  $\dot{v}_t$  by adjusting  $\beta_t$  according to the relationship

$$\beta_{t_k} = \beta_{t_{k-1}} + 0.0001\dot{v} \quad (3-90)$$

$V_{A_{x_t}}$ ,  $V_{A_{y_t}}$ , and  $V_{A_{z_t}}$  are then recalculated using Eq. (3-81), (3-82), and (3-83).

The control deflections are now adjusted to null the other body-axis accelerations, and  $\dot{u}_t$  is zeroed by adjustment of each throttle using the expression

$$\delta_{T_k} = \delta_{T_{k-1}} - 0.1\dot{u} \quad (3-91)$$

The horizontal tail, aileron, and rudder deflections are adjusted in a similar fashion to null out  $\dot{p}$ ,  $\dot{q}$ , and  $\dot{r}$ , respectively, according to the formulae

$$\delta_{e_k} = \delta_{e_{k-1}} + 0.8\dot{q} \quad (3-92)$$

$$\delta_{a_k} = \delta_{a_{k-1}} + 0.1\dot{p} \quad (3-93)$$

$$\delta_{r_k} = \delta_{r_{k-1}} + 0.1\dot{r} \quad (3-94)$$

With the completion of this phase of the algorithm, control reverts back to the beginning of the trim routine, and the whole cycle continuously repeats until the initiation of the compute mode.

### 3.7 Structural Modes

The equations of motion include the effects of three longitudinal and three lateral directional aeroelastic modes. References 2 and 3 contain the appropriate equations and coefficients valid for small perturbations of the aircraft from straight and level flight.

Consider the longitudinal modes first. Modes involving strong fuselage-stabilator coupling were selected because they are excited by the stabilator-control inputs, and contribute significantly to the sensor responses. Additionally, vibration modes were selected which adequately define the stabilator static (as well as dynamic) aerodynamic stability characteristics. The three longitudinal modes accounted for are:

- (1) A stabilator-bending mode, denoted by the variable  $\eta_1$ , which has a nominal frequency in the vicinity of 71.0 radians/second, and a nominal damping ratio of 0.012.
- (2) The first vertical-bending mode, designated by the variable  $\eta_2$ , with a nominal frequency of approximately 87.5 radians/second and a nominal damping ratio of about 0.021.

- (3) A stabilator-rotation mode, denoted by the variable  $\eta_3$ , at a nominal frequency of about 141.0 radians/second and a nominal damping ratio of 0.058.

Each of these modes is defined by a second-order differential equation with additional terms which couple in the basic airframe responses, the other modes, and the stabilator deflections. In addition, the effect of the modes on the pitching-moment and lift equations is available. The effect of the structural modes on the longitudinal equation of motion is not considered in References 2 and 3 and, therefore, is not considered in the present simulation mechanization.

The longitudinal structural-mode data are available in terms of dimensional derivatives. For the MIRA simulation, the coefficients of the aeroelastic equations have been nondimensionalized, and the equations programmed with constant coefficients as a function of dynamic pressure and true airspeed. In addition,  $I_y$  has been factored out of the aeroelastic terms of the pitching-moment equation, and  $m$  has been factored out of the aeroelastic terms of the lift equation. This has been done for two reasons. First, the coefficients of the structural-mode terms in the pitching-moment and lift equations are strongly affected by changes in  $I_y$  and  $m$ , respectively. Nondimensionalizing the coefficients provides a means of compensating for changes in these parameters easily and properly. Second, the simulation is more flexible and allows the investigation of a wider flight regime. While it is realized that some of the nondimensional coefficients of the structural-mode equations change with flight condition, they are also not available for all flight conditions. It may be possible to obtain an indication of the true results in these latter cases due to the nondimensionalization.

The longitudinal rigid-body modes and the fuselage and stabilator elastic modes are widely separated in frequency. For this reason, the static effects of the elastic modes on the rigid-body coefficients are negligible, and the latter parameters can be used without modification. Furthermore, changes in the vehicle cg do not affect the structural-mode coefficients significantly; it is sufficient to account for cg variations in the rigid-body coefficients as indicated in Section 3.3.

The equations given in References 2 and 3 are in the stability-axes coordinate system. At the nominal flight condition selected for the MIRA simulation, the pertinent coefficients of these equations



have been used directly in the body-axes equation of the simulator. Since the trim angle of attack at this flight condition is about 2 degrees, the effect is insignificant.

The resultant longitudinal structural-mode equations programmed in the MIRA simulation are:

$$\begin{aligned}\ddot{\eta}_1 = & -1.33\dot{\eta}_1 - 4436.46\eta_1 - 22.80\ddot{\delta}_e \\ & - \bar{q} \{ 1.95\eta_1 + 2.56\eta_2 + 13.60\eta_3 + 239.43\Delta\delta_e \} \\ & - \frac{\bar{q}}{V_A} \{ 10.90\Delta V_{A_z} + 321.22q_{rel} + 0.690\dot{\eta}_1 + 0.500\dot{\eta}_2 + 1.98\dot{\eta}_3 \\ & + 50.90\dot{\delta}_e \} \quad (3-95)\end{aligned}$$

$$\begin{aligned}\ddot{\eta}_2 = & -3.59\dot{\eta}_2 - 7518.5\eta_2 - 5.61\ddot{\delta}_e \\ & - \bar{q} \{ 0.279\eta_1 + 0.433\eta_2 + 0.767\eta_3 + 11.876\Delta\delta_e \} \\ & - \frac{\bar{q}}{V_A} \{ 0.540\Delta V_{A_z} + 17.664q_{rel} + 0.100\dot{\eta}_1 + 0.123\dot{\eta}_2 + 0.09318\dot{\eta}_3 \\ & + 4.246\dot{\delta}_e \} \quad (3-96)\end{aligned}$$

$$\begin{aligned}\ddot{\eta}_3 = & -16.240\dot{\eta}_3 - 20775.726\eta_3 - 23.43\ddot{\delta}_e \\ & - \bar{q} \{ -0.337\eta_1 - 0.405\eta_2 - 2.516\eta_3 - 62.751\Delta\delta_e \} \\ & - \frac{\bar{q}}{V_A} \{ -2.856\Delta V_{A_z} - 64.867q_{rel} - 0.0541\dot{\eta}_1 + 0.0210\dot{\eta}_2 + 0.481\dot{\eta}_3 \\ & + 5.972\dot{\delta}_e \} \quad (3-97)\end{aligned}$$

$$\begin{aligned}M_{SM_y} = & -\frac{\bar{q}}{V_A} \{ 11.664\dot{\eta}_1 + 5.596\dot{\eta}_2 + 45.809\dot{\eta}_3 + 1061.10\dot{\delta}_e \} \\ & - \bar{q} \{ 33.267\eta_1 + 39.049\eta_2 + 303.843\eta_3 \} - 135.705\ddot{\delta}_e \quad (3-98)\end{aligned}$$

$$\begin{aligned}F_{SM_z} = & -\frac{\bar{q}}{V_A} \{ 0.451\dot{\eta}_1 + 0.201\dot{\eta}_2 + 1.750\dot{\eta}_3 + 40.623\dot{\delta}_e \} \\ & - \bar{q} \{ 1.302\eta_1 + 1.512\eta_2 + 12.112\eta_3 \} - 3.910\ddot{\delta}_e \quad (3-99)\end{aligned}$$

It is noted that the aeroelastic equations are a function of  $\dot{\delta}_e$  and  $\ddot{\delta}_e$ . In the first mechanization of these equations,  $\dot{\delta}_e$  was obtained from a first-order lag present in the flight-control system,

and  $\ddot{\delta}_e$  obtained by back-differencing  $\dot{\delta}_e$ . It was determined that the amplitudes of  $\dot{\delta}_e$  and  $\ddot{\delta}_e$  achieved in this fashion were inversely proportional to the sampling interval, and very sharply peaked for step inputs. Unrealistic results were obtained. A more realistic simulation has been achieved by lagging  $\dot{\delta}_e$ , and then back-differencing the lagged  $\dot{\delta}_e$  to obtain  $\ddot{\delta}_e$ . The time constant of the lag is 50 milliseconds. The responses are smoother and much less dependent upon the computation interval.

The lateral-directional aeroelastic modes are now considered. The modes judged to be most significant in References 2 and 3, and for which data are available are:

- (1) The fuselage first torsion mode, designated by the variable  $\eta_4$ , with a nominal frequency of 39.7 radians/second and a nominal damping ratio of 0.011.
- (2) The wing first asymmetric-bending mode, designated by the variable  $\eta_5$ , with a nominal frequency of 67.6 radians/second and a nominal damping ratio of 0.0165.
- (3) The fuselage first lateral-bending mode, designated by the variable  $\eta_6$ , with a nominal frequency of 80.8 radians/second and a nominal damping ratio of 0.033.

Each of these modes is represented by a coupled linear second-order differential equation. However, unlike the longitudinal modes, there are no aeroelastic terms in the rigid-body equations.

In general, the same approach and assumptions which applied to the longitudinal-directional mode equations were also applied to the lateral-directional mode equations (e.g., the equations are in non-dimensional form). The three lateral-directional modes do not include all of the airframe elastic modes through the control-system cutoff frequency needed to define the flexibility of the primary surfaces and control surfaces. In References 2 and 3, this fact was accounted for by modifying the control-surface input coefficients of the rigid-body equations of motion to include static aeroelastic effects. The directional flight-control system used for the MIRA simulation includes a rudder-flexibility gain to account for this phenomenon (see Section 3.8). However, similar information is not available for  $\delta_a$ , and the unmodified data are used as presented in Section 3.4.

The final equations defining the three lateral-directional modes included in the MIRA simulation are given in Eq. (3-100), (3-101), and

(3-102). The  $\dot{\delta}_a$  and  $\dot{\delta}_r$  terms present in these equations are obtained in the same fashion as the  $\dot{\delta}_e$  term of the longitudinal aeroelastic equations.

$$\begin{aligned}\ddot{\eta}_4 = & -0.831\dot{\eta}_4 - 1566.176\eta_4 \\ & - \frac{\bar{q}}{V_A} \left\{ -48.867p_{rel} - 50.649r_{rel} + 0.0669\dot{\eta}_4 + 0.0755\dot{\eta}_5 \right. \\ & + 0.242\dot{\eta}_6 - 4.661\dot{\delta}_a - 2.543\dot{\delta}_r + 1.478V_{A_Y} \left. \right\} \\ & - \bar{q} \left\{ 0.0351\eta_4 + 0.0939\eta_5 + 0.442\eta_6 - 9.359\delta_a - 13.273\delta_r \right\}\end{aligned}\quad (3-100)$$

$$\begin{aligned}\ddot{\eta}_5 = & -2.139\dot{\eta}_5 - 4519.272\eta_5 \\ & - \frac{\bar{q}}{V_A} \left\{ -61.009p_{rel} - 59.879r_{rel} + 0.0874\dot{\eta}_4 + 0.155\dot{\eta}_5 \right. \\ & + 0.610\dot{\eta}_6 - 1.287\dot{\delta}_a - 4.467\dot{\delta}_r + 1.511V_{A_Y} \left. \right\} \\ & - \bar{q} \left\{ 0.0579\eta_4 + 0.187\eta_5 + 0.880\eta_6 + 0.692\delta_a - 17.253\delta_r \right\}\end{aligned}\quad (3-101)$$

$$\begin{aligned}\ddot{\eta}_6 = & -4.625\dot{\eta}_6 - 6167.393\eta_6 \\ & - \frac{\bar{q}}{V_A} \left\{ -65.984p_{rel} + 61.117r_{rel} + 0.0410\dot{\eta}_4 + 0.118\dot{\eta}_5 + 1.311\dot{\eta}_6 \right. \\ & - 7.670\dot{\delta}_a + 5.326\dot{\delta}_r - 1.420V_{A_Y} \left. \right\} \\ & - \bar{q} \left\{ 0.0558\eta_4 + 0.155\eta_5 + 1.176\eta_6 - 0.0253\delta_a + 18.290\delta_r \right\}\end{aligned}\quad (3-102)$$

### 3.8 Flight-Control System

The flight-control system implemented in the MIRA simulation was derived from that developed for the Survivable Flight Control System (SFCS) Program.<sup>(2)</sup> Although the goals of the SFCS program were significantly different from those of the MIRA program, the flight-control system developed is suitable for the MIRA investigation, and was selected as a representative system. The flight-control system developed for the SFCS program is an adaptive system designed for use over the whole flight envelope of the vehicle. The adaptive portion of this flight-control

system has not been programmed in the MIRA system, but reduced to a fixed-gain system suitable for operation in the region of the nominal flight condition.

Figures 3-5 and 3-6 depict the flight-control system programmed in the MIRA simulation. The longitudinal flight-control system was designed to provide good vehicle handling qualities, and used a combination of  $\Delta n_z$  and  $q$  feedback to achieve this goal. The lateral-directional system is fairly conventional with roll-rate feedback to the ailerons, and washed-out yaw-rate and lateral-acceleration feedback to the rudder. A roll-to-yaw crossfeed network is also included for turn coordination. In addition, it is possible to select an open-loop backup flight-control system, should it be desirable to investigate this mode of operation. The flight-control system includes structural-mode filters. A second-order notch filter centered at 84 radians/second, followed by a first-order lag with a corner frequency of 120 radians/second, is included in the longitudinal channel. Additional phase compensation is also needed. The roll channel includes a second-order notch filter centered at 40 radians/second. In the directional channel, the only structural-mode filter included is a first-order lag with a corner frequency of 40 radians/second on the lateral-accelerometer signal.

The longitudinal SFCS includes a model of a special-purpose secondary activator which has been deemed to be overly complex for the MIRA task. In order to achieve some simplification of the system, it has been replaced by a second-order model which is identical to those included in the roll and yaw channels. The stick force gain was also modified because of this change to produce a more desirable stick force per  $g$ . In all three channels, the power cylinder is represented by a first-order lag. The three pilot-input activating signals are a center stick for longitudinal control with a maximum amplitude of 50 pounds, a center stick for roll control with limits of  $\pm 12$  pounds, and the rudder pedals with a maximum force input of 150 pounds. A feel system was not mechanized, thus breakout, nonlinearities, etc., are not present in the MIRA simulation.

The position limits of the aerodynamic control surfaces are also indicated in Figures 3-5 and 3-6. They are  $+8$  degrees and  $-20$  degrees for the stabilator,  $\pm 30$  degrees for the combined aileron-spoiler surface, and  $\pm 30$  degrees for the rudder. The surfaces are also rate-limited;  $\pm 24$  degrees/second for the stabilator,  $\pm 193$  degrees/second for the aileron, and  $\pm 34$  degrees/second for the rudder.

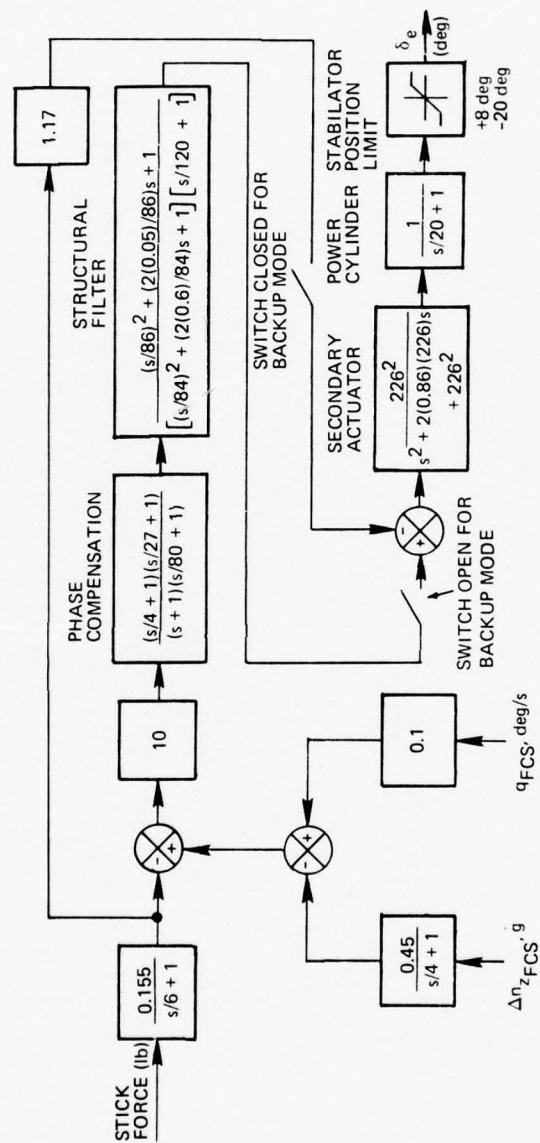


Figure 3-5. Longitudinal flight-control system.



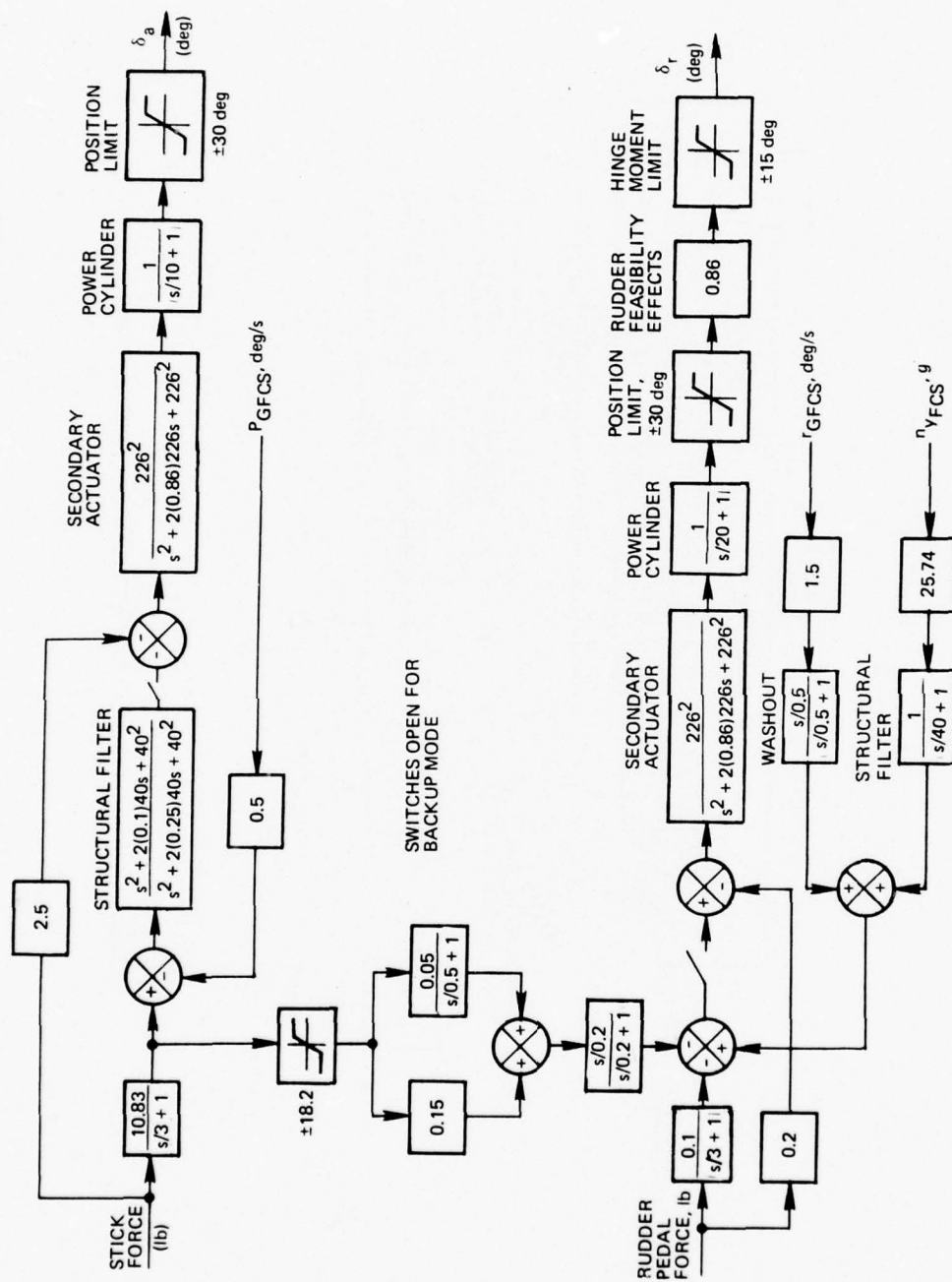


Figure 3-6. Lateral-directional flight-control system.

The effect of rudder flexibility and hinge-moment limiting is also included in the block diagram of the directional system. This phenomenon is modeled by a gain less than 1, and a position limit less than or equal to the physical limit of the rudder surface. The net effect of this is to reduce the rudder input to the aircraft aerodynamic and structural-mode equations. At the nominal flight condition, the rudder-flexibility gain is 0.86 and the hinge-moment limit is  $\pm 15$  degrees, rather than the  $\pm 30$ -degree actual position limit.

Separate control channels are mechanized for the right and left engines. A block diagram of the right throttle system is given in Figure 3-7. The control input is throttle position, which is limited to values between 0 and 100 degrees. A gain of 350 pounds/degree follows. The thrust of the right and left engines is limited between 0 and 35,000 pounds in each case. A first-order lag with a time constant of 0.5 second follows to simulate the thrust buildup due to engine lags following a throttle-command input.

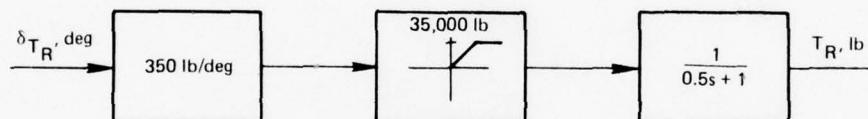


Figure 3-7. Block diagram of right-engine control section.

### 3.9 Simulation Inputs

The ability to input profile time histories of up to four signals has been programmed into the MIRA simulation. These signals can be any system inputs—such as the pilot inputs, the gusts, and winds, etc. This capability is achieved by generating a series of up to 10 points in time, and the amplitudes of the input variables at the corresponding points in time. The computer program linearly interpolates the amplitude of the input variables between the time points to achieve the desired profiles. With this capability, it is possible to apply different kinds and combinations of inputs to the simulation, and approximate those present in actual flight.

### 3.10 Turbulence Simulation

A fairly conventional approach to the simulation of turbulence is used in the MIRA simulation. The technique used is to linearly filter zero mean Gaussian noise to generate gust signals with a Dryden spectrum. These signals are easy to generate, and show a reasonable agreement with measured spectra.<sup>(7)</sup> Inherent in the generation of gust signals in this fashion are the commonly made assumptions that the gusts are stationary (the statistical properties are independent of time), and homogeneous (the statistical properties of the turbulence field are not changed by a translation of the coordinate system used to describe the turbulence).

Since a digital program is available which generates only two independent Gaussian signals, it was decided to generate only  $V_g$  and  $w_g$  in the MIRA simulation. The  $u_g$  signal has been dropped since it has the least important effect of the three on the aircraft responses. The side and vertical gust spectra are generated by passing the independent Gaussian signals through filters with the following transfer functions

$$T_{w_g} = K_g \sqrt{\frac{3V_A \sigma_w^2}{L_w \pi}} \frac{\left(s + \frac{V_A}{\sqrt{3}L_w}\right)}{\left(s + \frac{V_A}{L_w}\right)^2} \quad (3-103)$$

$$T_{V_g} = K_g \sqrt{\frac{3V_A \sigma_v^2}{L_v \pi}} \frac{\left(s + \frac{V_A}{\sqrt{3}L_v}\right)}{\left(s + \frac{V_A}{L_v}\right)^2} \quad (3-104)$$

$V_A$  is presently fixed at the trim air speed for the MIRA simulation. The constant  $K_g$  is needed because of the generation of the gust spectra by digital methods. A gain of  $K_g = \sqrt{\frac{\pi}{\Delta t}}$  must be included so that the variance of the gust signals is correct. This assumes that the variance of the Gaussian generator signal is unity. For the nominal flight condition, the turbulence scales,  $L_v$  and  $L_w$ , are fixed at 1,750 feet.

In order to generate stationary random-gust signals, it is necessary to independently operate the gust-generation scheme before applying the signals to the vehicle. This allows the system transients due to the filter to die out, and is accomplished in the MIRA simulation by switching to a standby mode prior to using the gust signals for the first time.

Several statistical analyses subroutines are also included in the MIRA simulation. It is possible to compute the mean, standard deviation and mean-square value of desired signals. Histograms of system variables can also be generated.

### 3.11 Sensor Models

In its simplest and most basic terms, the MIRA concept involves the use of aircraft sensors for both navigation and flight-control purposes. This is perhaps the most important and unique capability incorporated into the MIRA simulation. The sensor signals generated in this simulation take into account the effect of location on the acceleration measurements, gyro inclination effects, and aeroelasticity. Flight-control-system sensor models are available to generate signals for flight-control purposes along with navigation-sensor models whose outputs can be used for navigation, as well as flight-control, purposes. At present, the navigation sensors modeled include laser gyros and quartz flexure accelerometers. This section contains a discussion of the sensor effects and models incorporated into the MIRA simulation.

The rigid-body accelerations at a particular body-station location relative to the cg are given by the following matrix equation.

$$[n] = \frac{1}{g_0} \begin{Bmatrix} [\dot{V}] + [\omega_X][V] - \frac{1}{m}[F_{grav}] \\ + [\omega_X][1] + [\omega_X][\omega_X][1] \end{Bmatrix} \quad (3-105)$$

Expansion of this equation to allow for the independent location of the three accelerometers leads to

$$n_x = \frac{1}{g_0} \left[ \frac{F_x}{m} + g \sin \theta - x_{n_x}(r^2 + q^2) + y_{n_x}(pq) + z_{n_x}(rp) \right] \quad (3-106)$$

$$n_y = \frac{1}{g_0} \left[ \frac{F_y}{m} - g \cos \theta \sin \phi + x_{n_y}(\dot{r} + pq) - y_{n_y}(r^2 + p^2) + z_{n_y}(rq - \dot{p}) \right] \quad (3-107)$$

$$n_z = \frac{1}{g_0} \left[ \frac{F_z}{m} - g \cos \theta \cos \phi + x_{n_z}(pr - \dot{q}) + y_{n_z}(\dot{p} + qr) - z_{n_z}(q^2 + p^2) \right] \quad (3-108)$$

The flight-control signal uses the incremental normal acceleration from trim, and the initial value is subtracted from  $n_z$  to form the signal  $\Delta n_z$  for this purpose.

The capability to independently locate lateral and normal accelerometers for flight control and all three accelerometers for navigation has been programmed into the MIRA simulation. In practice, it is desired to locate the flight-control normal accelerometer forward of the cg so that the stabilizing effect of the pitch-acceleration component can be used to increase the short period damping. The location of the accelerometers is also dictated by a desire to not measure unwanted accelerations. For example, if the lateral accelerometer is located a significant vertical distance from the waterline, it will sense unwanted roll accelerations in addition to the true side accelerations.

The rigid-body rate-gyro signals are not affected by position, as in the case of the accelerometer signals. However, the roll-rate and yaw-rate gyros sense pitch, roll, and yaw rates due to gyro inclination effects. To minimize cross-axes sensing, the roll- and yaw-rate gyro sensitive axes are located parallel to and perpendicular to the average longitudinal principal axis, respectively. The longitudinal principal axis is oriented an average of 1.5 degrees below the aircraft waterline about which the body-axes equations are written.<sup>(3)</sup> In order to obtain the roll-rate and yaw-rate signals about the principal axis, it is necessary to transform p and r through a rotation of -1.5 degrees, thus

$$p_G = p \cos \alpha_G - r \sin \alpha_G \quad (3-109)$$

$$r_G = p \sin \alpha_G + r \cos \alpha_G \quad (3-110)$$

Bending effects are incorporated into the sensor signals by the addition of appropriate terms to the rigid-body signals. Acceleration signals are corrupted by the product of the displacement due to the mode and the second derivative of the generalized mode shape. Accelerometers are optimally located at the nodes of the modes to eliminate the effects of aeroelasticity. On the other hand, rate gyros are affected by the product of the slope of the mode shape and the rate of the generalized mode shape. Their optimum location is at the anti-nodes of the mode shapes. In practice, it is generally impossible to locate sensors at their optimum locations because of physical constraints and the need to satisfy the constraints of each mode simultaneously.

Based on the data presented in References 2 and 3, the following equations result (for the sensor signals which include the effects of bending).



$$q_{GB} = q_G + \frac{\partial \theta}{\partial \eta_1} \dot{\eta}_1 + \frac{\partial \theta}{\partial \eta_2} \dot{\eta}_2 + \frac{\partial \theta}{\partial \eta_3} \dot{\eta}_3 \quad (3-111)$$

$$n_{z_B} = n_z + \frac{1}{g_0} \left[ \frac{\partial h}{\partial \eta_1} \ddot{\eta}_1 + \frac{\partial h}{\partial \eta_2} \ddot{\eta}_2 + \frac{\partial h}{\partial \eta_3} \ddot{\eta}_3 \right] \quad (3-112)$$

$$p_{GB} = p_G + \frac{\partial \phi}{\partial \eta_4} \dot{\eta}_4 + \frac{\partial \phi}{\partial \eta_5} \dot{\eta}_5 + \frac{\partial \phi}{\partial \eta_6} \dot{\eta}_6 \quad (3-113)$$

$$r_{GB} = r_G + \frac{\partial \psi}{\partial \eta_6} \dot{\eta}_6 \quad (3-114)$$

$$n_{y_B} = n_y + \frac{1}{g_0} \left[ \frac{\partial h}{\partial \eta_6} \dot{\eta}_6 \right] \quad (3-115)$$

The coefficients of the bending terms in the previous equations are a function of the location of the sensors. The yaw-rate-gyro signal and the lateral-accelerometer signal are affected only by  $\eta_6$ , the fuselage first lateral-bending mode, and not by the fuselage first torsion mode and the wing first asymmetric-bending mode. The roll-rate signal is affected by all three lateral-directional modes. Each of the three longitudinal modes also corrupts the pitch-rate-gyro and normal-acceleration signals. The longitudinal-accelerometer signal is not affected by any mode signals for reasons discussed previously.

The flight-control-system sensor models incorporated into the MIRA simulation are those used for the SFCS simulation and analysis.<sup>(3)</sup> In the case of the flight-control-system accelerometers, a first-order lag represents the dynamics of the sensors. The corner frequency of the lag is 200 radians/second for the normal accelerometer, and 220 radians/second for the lateral accelerometer. Second-order systems are used to represent the flight-control-system rate gyros. The frequency of these systems is 150 radians/second, and the damping ratio is 0.6. These sensor models operate on the signals given by Eq. (3-111) through (3-115) to produce the input signals to the flight-control system.

Limits are imposed on the rates which the flight-control-system gyros sense. The limits are  $\pm 200$  degrees/second for the roll-rate gyro,  $\pm 50$  degrees/second for the pitch-rate gyro, and  $\pm 150$  degrees/second for the yaw-rate gyro.<sup>(1)</sup> The flight-control lateral accelerometer is limited to  $\pm 2$  g, while the normal accelerometer is limited to 10 g up and 4 g down.

More sophisticated models are incorporated into the MIRA simulation for the navigation gyros and accelerometers. Error models for three orthogonal ring-laser gyros are programmed. Each has a maximum rate of 400 degrees/second and a maximum pulse rate of 916,000 pulses/second.

Figure 3-8 is a block diagram of the roll-rate gyro, which is typical of the other two as well. The first operation undertaken in the model is the integration of the roll-rate-gyro signal, including bending effects. This is done by rectangular integration, i.e.

$$P_{GI} = \frac{P_{GB_k} + P_{GB_{k-1}}}{2} \cdot \Delta t \quad (3-116)$$

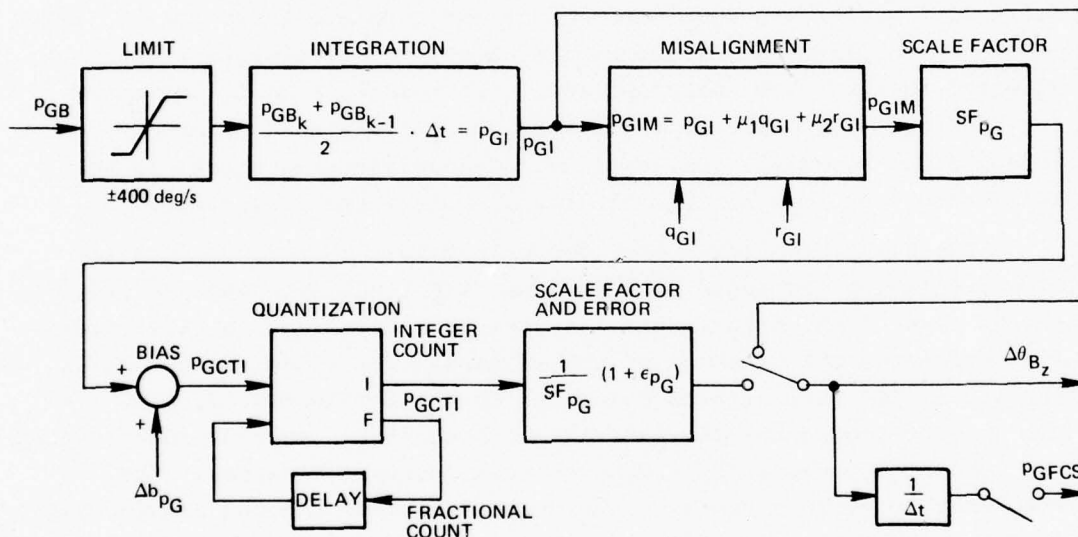


Figure 3-8. Block diagram of ring-laser roll-rate gyro.

The resultant signal represents the output of a perfect gyro. Next, misalignment errors are introduced with the addition of terms proportional to the integrated pitch-rate and yaw-rate signals.

$$P_{GIM} = P_{GI} + \mu_1 q_{GI} + \mu_2 r_{GI} \quad (3-117)$$

Multiplication by a scale factor converts the signal to pulses and a bias-error signal is added in. The computational algorithm is

$$P_{GCT} = SF_{P_G} (P_{GIM}) + \Delta b_{P_G} \quad (3-118)$$

It has been determined that it is not necessary to model the random-walk effects which characterize laser-gyro sensors for this phase of the MIRA project because it is a long-term phenomenon. When it is decided to incorporate this effect, it will be summed in at this juncture in the model. Quantization effects are represented by adding the fractional part of the pulse count remaining from the previous iteration to the present pulse count, and integerizing the sum. The result is called  $P_{GCTI}$ . The navigation-system signal is obtained by introducing the effects of the scale factor and its error, i.e.

$$\Delta \theta_{B_z} = \frac{1}{SF_{P_G}} (1 + \epsilon_{P_G}) P_{GCTI} \quad (3-119)$$

An option is included in the simulation to obtain the error between the perfect navigation sensor and that corrupted by all of the errors discussed. The flight-control roll-rate signal is obtained from this sensor model by dividing  $\Delta \theta_{B_z}$  by the computation time increment.

Three orthogonal quartz-flexure-type accelerometers, are modeled in the MIRA simulation. Each instrument can sense a maximum linear acceleration of 10 g. A maximum pulse rate of 320,000 pulses/second, and correspondingly relatively fine quantization is achieved through the use of the Sigma-Delta Modulation technique. Figure 3-9 is a block diagram of the lateral-accelerometer model, which is typical of the other two instruments. First, the lateral acceleration including bending is rectangularly integrated to produce a perfect accelerometer signal, i.e.

$$n_{y_{BI}} = \frac{n_{y_{B_k}} + n_{y_{B_{k-1}}}}{2} \cdot \Delta t \quad (3-120)$$

Misalignment errors are modeled by adding terms proportional to the integrated normal- and longitudinal-accelerometer signals to the integrated lateral-accelerometer signal. That is

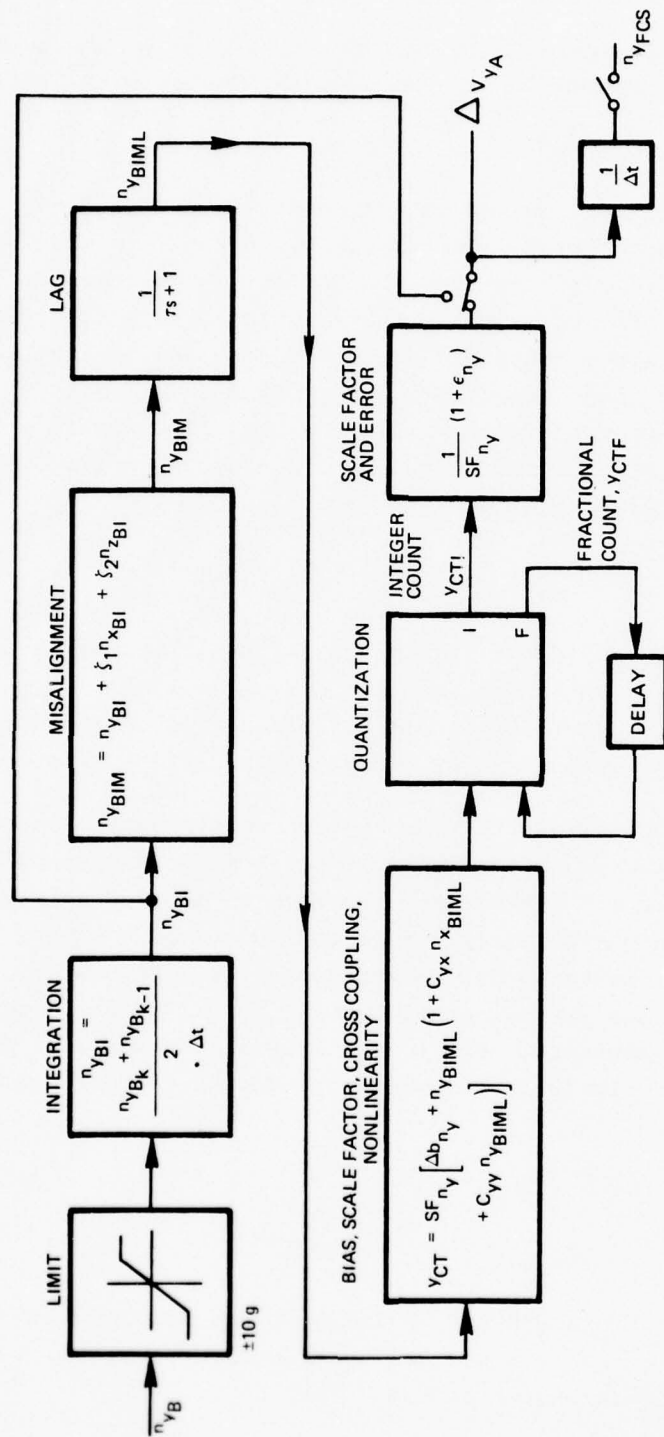


Figure 3-9. Block diagram of quartz-flexure lateral accelerometer.

$$n_{Y_{BIM}} = n_{Y_{BI}} + \zeta_1 n_{x_{BI}} + \zeta_2 n_{z_{BI}} \quad (3-121)$$

The resultant signal is then passed through a first-order lag to represent delays in the instrument

$$n_{Y_{BIML}} = \frac{n_{Y_{BIM}}}{\tau s + 1} \quad (3-122)$$

Crosscoupling effects are introduced by adding a constant times the product of the integrated lagged longitudinal-accelerometer signal, including misalignment effects, and the latest lateral-accelerometer signal to the lateral-accelerometer signal. Nonlinearities are taken into account by summing in a constant times the square of the integrated lagged lateral-acceleration signal. A term representing the bias error is also introduced, and the resultant signal converted to a pulse count by multiplying by a scale factor. The algorithm representing these operations is

$$Y_{CT} = SF_{n_Y} \left[ \Delta b_{n_Y} + n_{Y_{BIML}} (1 + C_{YX} n_{x_{BIML}} + C_{YY} n_{Y_{BIML}}) \right] \quad (3-123)$$

Quantization effects are handled by summing in the fractional part of the pulse count remaining from the previous iteration to the present pulse count and integerizing the sum, to produce a signal designated as  $Y_{CTI}$ . The navigation signal is obtained by reintroducing the effects of the scale factor along with its error, i.e.

$$\Delta V_{Y_A} = \frac{1}{SF_{n_Y}} (1 + \epsilon_{n_Y}) Y_{CTI} \quad (3-124)$$

An option is included in the simulation to obtain the error between the perfect navigation signal and the one corrupted by all of the errors discussed. The acceleration signal for flight control is obtained by dividing the navigation acceleration signal by  $\Delta t$ .

### 3.12 Navigation System Model

Presented in this section is the algorithm programmed in the MIRA simulation representing a strapdown Local Vertical Wander Azimuth (LVWA) navigation system. Reference 5 should be consulted for a more detailed description of the derivation of the algorithm and the assumptions involved in its generation. The navigation model can be divided into two major submodules; a high-speed loop computed at 50 hertz, and a low-speed loop computed at 5 hertz.



The high-speed navigation loop involves the generation of the body-to-computational or LVWA transformation matrix, the transformation of the navigation sensor velocities from the body frame to the computational frame and their subsequent accumulation over the low-speed computation time interval. A first-, second- or third-order quaternion update can be used to generate the body-to-computational-frame transformation matrix. As recommended in Reference 5, the generation of the body-to-computational-frame transformation matrix and the transformation of the velocity signals are staggered in time. The body-to-computational-frame transformation matrix is computed midway between the times at which the velocity transformation occurs. The attitude angles are extracted from the body-to-computational-frame transformation matrix for comparison with the corresponding true angles generated in the vehicle portion of the simulation.

The function of the low-speed portion of the navigation-system model is the integration of the fundamental equation of inertial navigation for a navigator employing an earth-relative computational frame. This equation is

$$[\dot{V}_{NC}] = [f] + [g] - \left\{ [\omega_{EC}\chi] + 2[\omega_{EI}\chi] \right\} [V_{NC}] \quad (3-125)$$

All signals are defined in the computational frame. A second integration follows to obtain the earth-relative position of the vehicle. Since the earth-relative position is expressed in angular coordinates (latitude, longitude, and wander angle), it is necessary to convert the level components of linear velocity from the *first* integration into angular velocity by dividing by the radius of curvature. The result is the angular velocities of the computational frame with respect to the earth. The computation-frame-to-earth transformation matrix is then obtained by integrating the following matrix differential equation

$$[\dot{T}_{CE}] = [T_{CE}][\omega_{CE}\chi] \quad (3-126)$$

and latitude, longitude, and wander angle extracted from  $[T_{CE}]$  via inverse trigonometric functions.

Altitude is obtained by integrating the vertical component of the earth-relative velocity. Third-order damping is included to stabilize the system. The navigation algorithm of Reference 5 has been modified to reflect the fact that a spherical earth is used in the vehicle equations of motion. This step involved the use of a gravity model different from that given in the reference, and the use of a constant earth radius to compute the angular velocities about level axes.

A transformation of the navigation-sensor signals is required before use in the navigation algorithm. This is due to the use of a different coordinate frame for the definition of the navigation algorithm from that used to define the vehicle equations of motion. The  $x$ ,  $y$ ,  $z$  coordinates of the navigation system are defined in an up, east, north sense—while those of the vehicle are in a nominal north, east, down sense. Thus, the required transformation from the body frame to the navigation frame is

$$x_N = -z_B \quad (3-127)$$

$$y_N = y_B \quad (3-128)$$

$$z_N = x_B \quad (3-129)$$

The airframe equations with bending and the sensor equations are solved at 400 hertz, while the high-speed navigation loop is solved at 50 hertz. It is necessary to sum the sensor outputs over the navigation system computation interval to account for this difference in the frequency of computation.

The equations of the high-speed navigation loop are now considered in detail. The integral of the angular rate of the body frame with respect to the computational frame is approximated by taking the integrated angular rates of the body frame with respect to the inertial reference (the outputs of the navigation sensors), and subtracting the integrated angular rates of the computational frame with respect to the inertial reference in body-frame coordinates. The integrated angular rates of the computational frame with respect to the inertial reference are obtained from the low-speed navigation loop, and are the sum of the inertial earth-rate signals and the computation-frame signals with respect to earth times the high-speed computation time. These signals must then be transformed from the computational frame to the body frame. This formulation assumes that the angular accelerations of the computation frame with respect to the inertial reference are zero. In the simulation, the following equations are solved.

$$[\Delta\theta] = [\Delta\theta_B] - [T_{BC}]^T [\omega_{CI}] \Delta t_{HI} \quad (3-130)$$

$$\begin{bmatrix} \Delta\theta_x \\ \Delta\theta_y \\ \Delta\theta_z \end{bmatrix} = \begin{bmatrix} \Delta\theta_{B_x} \\ \Delta\theta_{B_y} \\ \Delta\theta_{B_z} \end{bmatrix} - \begin{bmatrix} T_{BC11} & T_{BC12} & T_{BC13} \\ T_{BC21} & T_{BC22} & T_{BC23} \\ T_{BC31} & T_{BC32} & T_{BC33} \end{bmatrix} \begin{bmatrix} \omega_{CI_x} \\ \omega_{CI_y} \\ \omega_{CI_z} \end{bmatrix} \Delta t_{HI} \quad (3-131)$$

Next, the parameters of the quaternion update are computed using the integrated angular rates of the body frame with respect to the computational frame just obtained. Either a first-, second-, or third-order update can be used, and the appropriate set of the following parameters computed.

First-order update

$$p_0 = 1 \quad (3-132)$$

$$p_1 = \frac{\Delta\theta_x}{2} \quad (3-133)$$

$$p_2 = \frac{\Delta\theta_y}{2} \quad (3-134)$$

$$p_3 = \frac{\Delta\theta_z}{2} \quad (3-135)$$

Second-order update

$$p_0 = 1 - \frac{1}{2}(\Delta\theta^2) \quad (3-136)$$

$$\Delta\theta^2 = \left(\frac{\Delta\theta_x}{2}\right)^2 + \left(\frac{\Delta\theta_y}{2}\right)^2 + \left(\frac{\Delta\theta_z}{2}\right)^2 \quad (3-137)$$

$$p_1 = \frac{\Delta\theta_x}{2} \quad (3-138)$$

$$p_2 = \frac{\Delta\theta_y}{2} \quad (3-139)$$

$$p_3 = \frac{\Delta\theta_z}{2} \quad (3-140)$$

Third-order update

$$p_0 = 1 - \frac{1}{2}(\Delta\theta^2) \quad (3-141)$$

$$p_1 = \left[ 1 - \frac{1}{6}(\Delta\theta^2) \right] \left( \frac{\Delta\theta x_n}{2} \right) + \frac{1}{6} \left[ \left( \frac{\Delta\theta z_n}{2} \right) \left( \frac{\Delta\theta y_{n-1}}{2} \right) - \left( \frac{\Delta\theta y_n}{2} \right) \left( \frac{\Delta\theta z_{n-1}}{2} \right) \right] \quad (3-142)$$

$$p_2 = \left[ 1 - \frac{1}{6}(\Delta\theta^2) \right] \left( \frac{\Delta\theta y_n}{2} \right) + \frac{1}{6} \left[ \left( \frac{\Delta\theta x_n}{2} \right) \left( \frac{\Delta\theta z_{n-1}}{2} \right) - \left( \frac{\Delta\theta z_n}{2} \right) \left( \frac{\Delta\theta x_{n-1}}{2} \right) \right] \quad (3-143)$$

$$p_3 = \left[ 1 - \frac{1}{6}(\Delta\theta^2) \right] \left( \frac{\Delta\theta z_n}{2} \right) + \frac{1}{6} \left[ \left( \frac{\Delta\theta y_n}{2} \right) \left( \frac{\Delta\theta x_{n-1}}{2} \right) - \left( \frac{\Delta\theta x_n}{2} \right) \left( \frac{\Delta\theta y_{n-1}}{2} \right) \right] \quad (3-144)$$

The subscript  $n$  in the previous equations denotes that the values from the present iteration are used, while the variables with a subscript  $n-1$  are those from the previous iteration. When subscripts are not used, the present values are used. The updated quaternion parameters are then given by

$$\begin{bmatrix} q_{0n} \\ q_{1n} \\ q_{2n} \\ q_{3n} \end{bmatrix} = \begin{bmatrix} p_0 & -p_1 & -p_2 & -p_3 \\ p_1 & p_0 & p_3 & -p_2 \\ p_2 & -p_3 & p_0 & p_1 \\ p_3 & p_2 & -p_1 & p_0 \end{bmatrix} \begin{bmatrix} q_{0n-1} \\ q_{1n-1} \\ q_{2n-1} \\ q_{3n-1} \end{bmatrix} \quad (3-145)$$

Once every second, the  $q$  terms are normalized by multiplying each one by

$$\tilde{q} = 1 - \frac{1}{2}(q_0^2 + q_1^2 + q_2^2 + q_3^2 - 1) \quad (3-146)$$

The initial values of the  $q$  terms are obtained from the expressions

$$q_{0t} = -\cos\left(\frac{\theta_t}{2}\right) \cos\left(\frac{\phi_t}{2}\right) \cos\left(\frac{\psi_t}{2}\right) - \sin\left(\frac{\theta_t}{2}\right) \sin\left(\frac{\phi_t}{2}\right) \sin\left(\frac{\psi_t}{2}\right) \quad (3-147)$$

$$q_{1t} = \cos\left(\frac{\theta_t}{2}\right) \cos\left(\frac{\phi_t}{2}\right) \sin\left(\frac{\psi_t}{2}\right) - \sin\left(\frac{\theta_t}{2}\right) \sin\left(\frac{\phi_t}{2}\right) \cos\left(\frac{\psi_t}{2}\right) \quad (3-148)$$

$$q_{2t} = -\sin\left(\frac{\theta_t}{2}\right) \cos\left(\frac{\phi_t}{2}\right) \cos\left(\frac{\psi_t}{2}\right) - \cos\left(\frac{\theta_t}{2}\right) \sin\left(\frac{\phi_t}{2}\right) \sin\left(\frac{\psi_t}{2}\right) \quad (3-149)$$

$$q_{3_t} = -\cos\left(\frac{\theta_t}{2}\right) \sin\left(\frac{\phi_t}{2}\right) \cos\left(\frac{\psi_t}{2}\right) + \sin\left(\frac{\theta_t}{2}\right) \cos\left(\frac{\phi_t}{2}\right) \sin\left(\frac{\psi_t}{2}\right) \quad (3-150)$$

where  $\phi_t$ ,  $\theta_t$ , and  $\psi_t$  are the trim values of the roll, pitch, and yaw angles; and the initial wander angle is assumed to be zero.

With respect to the  $q$  terms, the transformation from body to computational coordinates is given by

$$[T_{CB}] = \begin{bmatrix} 1 - 2(q_2^2 + q_3^2) & 2(q_1q_2 - q_0q_3) & 2(q_3q_1 + q_0q_2) \\ 2(q_1q_2 + q_0q_3) & 1 - 2(q_3^2 + q_1^2) & 2(q_2q_3 - q_0q_1) \\ 2(q_3q_1 - q_0q_2) & 2(q_2q_3 + q_0q_1) & 1 - 2(q_1^2 + q_2^2) \end{bmatrix} \quad (3-151)$$

whereas, in terms of the Euler angles this matrix is

$$[T_{CB}] = \begin{bmatrix} \cos \theta_N \cos \phi_N & -\cos \theta_N \sin \phi_N & \sin \theta_N \\ \cos \psi' \sin \phi_N & \cos \psi' \cos \phi_N & \sin \psi' \cos \theta_N \\ -\sin \psi' \sin \theta_N \cos \phi_N & +\sin \psi' \sin \theta_N \sin \phi_N & \\ -\sin \psi' \sin \phi_N & -\sin \psi' \cos \phi_N & \cos \psi' \cos \theta_N \\ -\cos \psi' \sin \theta_N \cos \phi_N & +\cos \psi' \sin \theta_N \sin \phi_N & \end{bmatrix} \quad (3-152)$$

and  $\psi' = \psi_N - w_{AN}$ . The navigation Euler angles can then be obtained by the following formulae, for comparison with the vehicle's Euler angles.

$$\phi_N = \tan^{-1} \left( \frac{-T_{CB12}}{T_{CB11}} \right) \quad (3-153)$$

$$\theta_N = \tan^{-1} \left( \frac{T_{CB13}}{T_{CB11}^2 + T_{CB12}^2} \right) \quad (3-154)$$

$$\psi_N = \tan^{-1} \left( \frac{T_{CB23}}{T_{CB33}} \right) + w_{AN} \quad (3-155)$$

A transformation of the integrated linear accelerations from the body frame to the computational frame is performed next, using the body-to-computational-frame transformation matrix just defined. The appropriate equations are



$$\Delta V_{N_x} = \Delta V_{x_A} T_{CB_{11}} + \Delta V_{y_A} T_{CB_{12}} + \Delta V_{z_A} T_{CB_{13}} \quad (3-156)$$

$$\Delta V_{N_y} = \Delta V_{x_A} T_{CB_{21}} + \Delta V_{y_A} T_{CB_{22}} + \Delta V_{z_A} T_{CB_{23}} \quad (3-157)$$

$$\Delta V_{N_z} = \Delta V_{x_A} T_{CB_{31}} + \Delta V_{y_A} T_{CB_{32}} + \Delta V_{z_A} T_{CB_{33}} \quad (3-158)$$

Then, these signals are summed over the low-speed navigation-system computation interval before being fed to the low-speed portion of the navigation system, i.e.

$$\Delta V_x = \sum_{n=1}^{10} \Delta V_{N_{x_n}} \quad (3-159)$$

$$\Delta V_y = \sum_{n=1}^{10} \Delta V_{N_{y_n}} \quad (3-160)$$

$$\Delta V_z = \sum_{n=1}^{10} \Delta V_{N_{z_n}} \quad (3-161)$$

This completes the discussion of the high-speed portion of the navigation-system model.

A detailed discussion of the algorithms of the low-speed portion of the navigation model follows. The first step is the updating of the computational-frame velocities. The equations coded are

$$V_{NC_{x_m}} = V_{NC_{x_{m-1}}} + \Delta V_x + \omega_1 + g_x \Delta t_{LO} \quad (3-162)$$

$$V_{NC_{y_m}} = V_{NC_{y_{m-1}}} + \Delta V_y + \omega_2 + g_y \Delta t_{LO} \quad (3-163)$$

$$V_{NC_{z_m}} = V_{NC_{z_{m-1}}} + \Delta V_z + \omega_3 + g_z \Delta t_{LO} \quad (3-164)$$

The  $\omega_1$ ,  $\omega_2$ , and  $\omega_3$  are the elements of the matrix  $-\{[\omega_{CEX}] + 2[\omega_{EIX}]\} [V_{NC}] \cdot \Delta t_{LO}$ , which results from the fundamental equation of the navigation system. The initial values of  $V_{NC_x}$ ,  $V_{NC_y}$ , and  $V_{NC_z}$  are obtained by transforming the initial values of  $u_{rel}$ ,  $v_{rel}$ , and  $w_{rel}$  to the computational frame.

Damping of the vertical velocity is accomplished by recalculating the vertical-vector component according to the equation

$$V_{NC_x}^{(d)} = V_{NC_{x_m}} + (C_2 \delta h_{m-1} + \overline{\delta a}_{m-1}) \Delta t_{LO} \quad (3-165)$$

Where  $\delta h = h - h_N$  is the altitude error, and  $\overline{\delta a}$  is defined later in the discussion of the low-speed navigation system when the altitude is calculated.

The calculation of the angular velocities about the level axes occurs next. For a spherical earth, the appropriate equations are

$$\omega_{CE_Y} = \frac{-V_{NC_{z_m}}}{R_0} \left[ 1 - \frac{h_{m-1}}{R_0} \right] \quad (3-166)$$

$$\omega_{CE_Z} = \frac{V_{NC_{y_m}}}{R_0} \left[ 1 - \frac{h_{m-1}}{R_0} \right] \quad (3-167)$$

and  $\omega_{CE_X} = 0$ .

An updating of the computational-frame-to-earth direction cosine matrix follows. This is accomplished by solving the equation

$$[T_{CE}]_m = [T_{CE}]_{m-1} + [T_{CE}]_{m-1} [\omega_{CE}^X] \Delta t_{LO} \quad (3-168)$$

The matrix  $[T_{CE}]$  is given, in terms of latitude, longitude, and wander angle by

$$[T_{CE}] = \begin{bmatrix} \cos \sigma_N \cos \lambda_N & \cos \sigma_N \sin \lambda_N \sin w_{AN} & -\cos \sigma_N \sin \lambda_N \cos w_{AN} \\ & -\sin \sigma_N \cos w_{AN} & +\sin \sigma_N \sin w_{AN} \\ \sin \sigma_N \cos \lambda_N & \sin \sigma_N \sin \lambda_N \sin w_{AN} & -\sin \sigma_N \sin \lambda_N \cos w_{AN} \\ & +\cos \sigma_N \cos w_{AN} & +\cos \sigma_N \sin w_{AN} \\ \sin \lambda_N & -\cos \lambda_N \sin w_{AN} & \cos \lambda_N \cos w_{AN} \end{bmatrix} \quad (3-169)$$

and is initialized at  $w_{A_t} = 0.0$ ,  $\lambda_t$ , and  $\sigma_t$ . Every 30 seconds, the direction cosine matrix is orthonormalized according to the formula

$$[T_{CE}]_{ortho} = [T_{CE}] - \frac{1}{2} [T_{CE}] \left\{ [T_{CE}]^T [T_{CE}] - [I_0] \right\} \quad (3-170)$$

The computation of the earth-rate signals occurs next in the navigation model, using the equations

$$[\omega_{EI}] = \begin{bmatrix} \omega_{EI_x} \\ \omega_{EI_y} \\ \omega_{EI_z} \end{bmatrix} = \omega_E \begin{bmatrix} T_{CE_{31}} \\ T_{CE_{32}} \\ T_{CE_{33}} \end{bmatrix} \quad (3-171)$$

The gyro-torquing signals required for the generation of the integrated angular rates of the body frame, with respect to the computational frame in the high-speed-navigation loop, can now be obtained. These signals are generated from the equation

$$[\omega_{CI}] = [\omega_{EI}] + [\omega_{CE}] \quad (3-172)$$

or more explicitly

$$\omega_{CI_x} = \omega_{EI_x} \quad (3-173)$$

$$\omega_{CI_y} = \omega_{EI_y} + \omega_{CE_y} \quad (3-174)$$

$$\omega_{CI_z} = \omega_{EI_z} + \omega_{CE_z} \quad (3-175)$$

The integrated angular-rate terms, crosscoupled with the computational-frame velocity terms present in the velocity update equation ( $\omega_1$ ,  $\omega_2$ , and  $\omega_3$ ), are now calculated using the expression

$$- \{ [\omega_{CE}^x] + 2[\omega_{EI}^x] \} [V_{NC}] \Delta t_{LO} \quad (3-176)$$

The specific expressions for the elements of this matrix are

$$\omega_1 = \left[ \left( \omega_{CE_z} + 2\omega_{EI_z} \right) V_{NC_y} - \left( \omega_{CE_y} + 2\omega_{EI_y} \right) V_{NC_z} \right] \Delta t_{LO} \quad (3-177)$$

$$\omega_2 = \left[ - \left( \omega_{CE_z} + 2\omega_{EI_z} \right) V_{NC_x}^{(d)} + 2\omega_{EI_x} V_{NC_z} \right] \Delta t_{LO} \quad (3-178)$$

$$\omega_3 = \left[ \left( \omega_{CE_y} + 2\omega_{EI_y} \right) V_{NC_x}^{(d)} - 2\omega_{EI_x} V_{NC_y} \right] \Delta t_{LO} \quad (3-179)$$

Computation of the navigation-system altitude is accomplished by integrating the vertical-velocity component. Including the effects of vertical damping, the appropriate equations are

$$h_{N_m} = h_{N_{m-1}} + \left( V_{NC_{x_{m-1}}}^{(d)} + C_1 \delta h_{m-1} \right) \Delta t_{LO} \quad (3-180)$$

$$\delta \bar{a}_m = \delta \bar{a}_{m-1} + C_3 \delta h_m \Delta t_{LO} \quad (3-181)$$

The altitude error is also updated in this portion of the model for use in the next cycle of the damping of the vertical-velocity term.

Next, the gravity terms included in the velocity-update equation are calculated from expressions which include the central and centrifugal forces because of the spherical-earth approximation. The appropriate equations are

$$g_x = -g_0 \left[ 1 - 2 \left( \frac{h_N}{R_0} \right) + 3 \left( \frac{h_N}{R_0} \right)^2 \right] + \omega_E^2 R_0 \left( 1 + \frac{h_N}{R_0} \right) (1 - T_{CE31}^2) \quad (3-182)$$

$$g_y = -\omega_E^2 R_0 \left( 1 + \frac{h_N}{R_0} \right) T_{CE31} T_{CE32} \quad (3-183)$$

$$g_z = -\omega_E^2 R_0 \left( 1 + \frac{h_N}{R_0} \right) T_{CE31} T_{CE33} \quad (3-184)$$

Latitude, longitude, and wander angle can be extracted from the elements of the direction cosine matrix, viz

$$\lambda_N = \tan^{-1} \left\{ \frac{T_{CE31}}{(T_{CE11}^2 + T_{CE21}^2)^{1/2}} \right\} \quad (3-185)$$

$$\sigma_N = \tan^{-1} \left\{ \frac{T_{CE21}}{T_{CE11}} \right\} \quad (3-186)$$

$$w_{AN} = \tan^{-1} \left\{ \frac{-T_{CE32}}{T_{CE33}} \right\} \quad (3-187)$$

Last of all, the sine and cosine of the wander angle are used to transform the navigation velocities in the computational frame to the local-vertical north-pointing frame, according to the formulae

$$V_{L_x} = V_{NC_x} (d) \quad (3-188)$$

$$V_{L_y} = V_{NC_y} \cos w_{AN} + V_{NC_z} \sin w_{AN} \quad (3-189)$$

$$V_{L_z} = -V_{NC_y} \sin w_{AN} + V_{NC_z} \cos w_{AN} \quad (3-190)$$

To aid in the evaluation of different MIRA concepts, error signals between vehicle and navigation-system variables are generated in the simulation. The errors generated are those of the Euler angles, latitude, longitude, wander angle, altitude, and the earth-relative

velocities. This completes the discussion of the computations performed in the LVWA navigation-system mode of the MIRA simulation.

### 3.13 A General Description of the Navigation and Attitude-Error Propagation Model

This section contains a general description of an algorithm developed to generate the error in:

- (1) Position - latitude, longitude, altitude.
- (2) Velocity - north, east, vertical.
- (3) Attitude - roll, pitch, heading.

for a strapdown system. It is assumed that the incremental velocity and incremental angular errors are available from cascaded inertial-sensor models and compensation, or inertial-sensor error models, together with the usual flight-profile data. This technique (described in detail in Reference 8) will replace that presently incorporated into the MIRA simulation, which includes the strapdown-navigation model and subsequent differencing of its outputs with the aircraft equations-of-motion model in order to generate the errors discussed in Section 3.12. The approach currently implemented in the MIRA simulation more accurately reflects the expected performance of an actual INS, since it includes the effects of computational errors in the overall navigator performance. However, it also introduces more stringent computational requirements than are necessary to evaluate the effects of the flight environment on the inertial-sensor performance and the overall system performance. In the proposed program, the only differencing remaining is that between the simulated inertial sensors and the "ideal" sensors. This feature renders the proposed scheme different from any existing error-propagation program.

The following assumptions are made in the development of the navigation-error equations:

- (1) The earth is spherical.
- (2) The aircraft equations-of-motion model provides a nominal trajectory, consisting of the body-to-local-vertical transformation, the body specific forces, the body angular rates, the latitude, the longitude, and the altitude of the vehicle, and the local vertical with respect to earth velocities.
- (3) The inertial-sensor models provide the errors in the angular rates and specific forces.



Since the earth model used in both the equations of motion and the strapdown-navigation model is spherical, a space-stabilized computational frame is employed for the navigation-error equations. This has the great advantage that the navigation equations, including vertical damping, are perfectly symmetrical with respect to each of the three axes of the position and velocity variables. Therefore, only one axis of the three need be considered in developing the error equations, and the results extended to the remaining two axes by symmetry. The result is that the state errors are arranged in a  $2 \times 3$ -matrix form rather than as a  $6 \times 1$ -column vector, and the state transition matrix becomes  $2 \times 2$ , instead of  $6 \times 6$ . Similarly, the attitude-error equations become a single  $(3 \times 3) \times (3 \times 1)$  matrix-vector equation.

The attitude computations for a strapdown system consist merely of extracting the three Euler angles from the body-to-local-vertical-north (LVN) transformation via appropriate inverse trigonometric functions.

Attitude errors arise from two different, but not independent, sources. First, any errors in initial alignment or gyro-drift compensation will produce angular errors in the knowledge of the motion of the body frame. Second, accelerometer- and gyro-compensation, initial-alignment, and mechanization errors all integrate into latitude and longitude errors. These are angular errors in the knowledge of the LVN frame. Since the computed attitude matrix is a function of both where the computer "thinks" the body frame is and where it "thinks" the LVN frame is, the attitude-error vector is a function of these two factors, as well as the attitude angles. Naturally, the attitude-error computations are singular for a pitch angle of  $\pm 90$  degrees. In deriving the attitude-error equations, the position errors must first be interpreted as errors in the transformation from the inertial frame to the computed LVN frame. Then, the errors in the LVN transformation must be interpreted as attitude errors. Finally, the matrix of the resulting system of equations must be inverted to obtain the attitude errors explicitly.

The main savings resulting from the error-propagation approach are the elimination of the strapdown "velocity/attitude" algorithm, and the elimination of the attitude extraction. In addition, the navigation-like computations for a strapdown system are more efficiently performed

in the inertial frame. Finally, computational-accuracy requirements are reduced, since errors are the only forcing functions.

In addition to the efficiency resulting from this approach, it isolates the effects of sensor errors from all other navigation effects (truncation, roundoff, model limitations), and thus is ideally suited for the MIRA application.

## SECTION 4

### DEMONSTRATION OF MIRA SIMULATION CAPABILITY AND COMPARISON OF RESULTS

#### 4.1 Introduction

This section deals with a demonstration of the simulation capability developed to evaluate the MIRA concept. First, a description of the sensor configurations selected for evaluation is given. Then, associated data (such as the structural-mode sensor coefficients, the pilot inputs to the simulation, the turbulence levels, the navigation-sensor parameters, etc.) are discussed. A general comparison of the results obtained for the various cases follows.

The data contained in this section should not be viewed as representative of a recommended MIRA configuration, but as a demonstration of the capability of the simulation. Several configurations were chosen which, at this point, appear to be valid candidates for MIRA systems (i.e., both dispersed and colocated inertial instruments, and both separate and common navigation and flight-control instruments) to demonstrate the feasibility of using the simulation for a wide class of MIRA systems. In general, the test cases included in this report are not of sufficient duration to permit the drawing of substantial conclusions concerning the navigation performance of the various configurations. The test run times were limited to allow a wide range of cases to be investigated in this phase with the non-real-time simulation. Within this context, however, some limited conclusions are drawn about the MIRA configurations considered, and about the MIRA approach in general as it impacts navigation and flight-control performance. The importance of the bending-mode data in this performance evaluation, particularly in the area of flight control, is clearly indicated by the data to be presented herein.

#### 4.2 Data for MIRA Simulation Runs

Three basic sensor configurations have been selected for evaluation in this phase of the project. The configuration used to check out

the simulation, as well as to demonstrate the MIRA simulation capability, had sensors dispersed along the fuselage at locations selected for the flight test of the Survivable Flight Control System.<sup>(2)(3)</sup> This is denoted as the SFCS configuration. The sensor locations for this configuration were chosen based upon space available on the test aircraft to mount the sensors, and a desire to minimize the effect of the aero-elastic modes on the sensor responses given these physical constraints. The sensor locations for this configuration are given in Table 4-1. As a point of reference, the cg for the nominal-vehicle configuration is located at 30.6 percent  $\bar{c}$ , or 320 inches behind the nose of the aircraft along the waterline (FS320), and 27.65 inches up from the waterline of the vehicle (WL27.65).

Table 4-1. SFCS sensor locations.

Sensor	Fuselage Station (FS) (in.)	Water-Line (WL) (in.)	Butt-line (in.)	Direction of Sensing Axis
Pitch-Rate Gyro	383	6	47.5 L	Parallel to the y axis, positive aircraft nose up
Roll-Rate Gyro	77	11.5	00	Forward in the x-z plane and 1.5 degrees below waterline
Yaw-Rate Gyro	383	6	47.5 R	Down, parallel to x-z plane and perpendicular to the roll-rate-gyro sensing axis
Lateral Accelerometer	186.3	19.8	00	Perpendicular to x-z plane, positive to pilot's right
Normal Accelerometer	77	22.5	00	Perpendicular to the waterline, positive down

The other two configurations selected for evaluation assume that all of the sensors are colocated. One sensor package was chosen to be located slightly forward of the cg at FS313 on the x body axis, and 27.65 inches up from the waterline. This location was selected because it was one of the candidate positions for locating sensors on the SFCS program, and presumably there is some available space there. The third sensor location selected for evaluation in this phase of the program



assumes that all of the sensors are located just forward of the pilot's station at FS77. The pilot's station is located at about FS119. Relative to the waterline, this package is assumed to be located at WL22.5. For all configurations, the roll rate gyro sensing axis is inclined  $1.5^\circ$  below the waterline. The yaw rate gyro sensing axis is perpendicular to the roll rate gyro sensing axis.

This selection of sensor configurations allows many different cases to be evaluated. It is possible to investigate system performance using any one of the three configurations for the flight-control sensors, while simultaneously using any one of the configurations for the navigation sensors. The use of common sensors for both navigation and flight-control purposes can also be investigated for each of the three selected configurations. Furthermore, perfect sensors can be selected, and the level of turbulence varied.

Table 4-2 contains a list of the configurations evaluated using the MIRA simulation. The quantity of data gathered from these runs was quite vast. In order to reasonably limit the amount of data contained herein, while at the same time demonstrating the capability of the MIRA simulation, results are presented to allow a comparison of the selected sensor configurations from two points of view. In the first instance, a basic-sensor configuration is selected; e.g., the sensors are at the SFCS locations. A comparison is then made for three different conditions. The first is an ideal situation where perfect sensors are used for navigation and flight-control, and the vehicle is flying in a non-turbulent environment. In the second, the perfect-sensor models are replaced by realistic models, and the vehicle is flying in a turbulent environment. For the third condition, the navigation sensors are used for both navigation and flight control, and the vehicle is flying in gusts. More specifically, the basic responses of the vehicle and navigation system for configurations 11, 12, and 13 (see Table 4-2) are compared. In addition, configurations 8, 9, and 10 (see Table 4-2) are compared with regard to their structural-mode responses.

A comparison is also made of the vehicle responses obtained with a conventional sensor configuration (in which the flight-control sensors are located at the SFCS stations on the vehicle, and the navigation sensors are located close to the cg of the vehicle at FS313). These responses are compared with those obtained for three sensor configurations using common sensors for both navigation and flight-control purposes. In one case, the sensors are at FS313; in another, forward of the pilot's station at FS77; and, in the third, at the SFCS location. Configurations 3, 7, 10, and 13 (see Table 4-2) are the specific ones compared in this report.



Table 4-2. Configurations evaluated using MIRA simulation.

Configuration Number	Navigation Sensor Location	Flight-Control Sensor Location	Turbulence (Nominal rms Value of 1 ft/s)	Perfect Sensors	Common Navigation and Flight-Control Sensors
1	SFCS	FS313	No	Yes	No
2	SFCS	FS313	No	No	No
3	SFCS	FS313	Yes	No	No
4	SFCS	FS313	Yes*	No	No
5	FS313	FS313	No	Yes	No
6	FS313	FS313	Yes	No	No
7	FS313	FS313	Yes	No	Yes
8	FS77	FS77	No	Yes	No
9	FS77	FS77	Yes	No	No
10	FS77	FS77	Yes	No	Yes
11	SFCS	SFCS	No	Yes	No
12	SFCS	SFCS	Yes	No	No
13	SFCS	SFCS	Yes	No	Yes

\* rms value of 10 ft/s.

A fairly simple maneuver is used for the purpose of demonstrating the capability of the MIRA simulation. The specific pilot inputs to the simulation are shown in Figure 4-1. A right lateral-stick pulse input of 1.33 pounds is applied to the vehicle in order to achieve a banked right turn. A bank angle of approximately 32.5 degrees results. Simultaneously, a pitch-stick step input of 0.915 pound is applied to keep the nose of the aircraft up. These are the inputs to the vehicle until a heading change of approximately 37.5 degrees is achieved, at which time, the pitch-stick input is removed and a left lateral-stick pulse of 1.33 pounds is applied to achieve wings-level flight. After a short period to allow the system transients to die out, a pitch-stick step input of 5 pounds is applied to pull the nose of the aircraft up.

The coefficients defining the effect of the aeroelastic modes of the F-4 on the sensor responses were determined for each of the sensor configurations discussed previously. Tables 4-3 and 4-4 contain the pertinent parameters, along with the distances from the accelerometer locations to the vehicle cg. These data were obtained from References 2 and 3, but no information is given about the location of the longitudinal accelerometer, since it is not needed for flight-control purposes. However, for the SFCS sensor configuration, it is assumed that the longitudinal accelerometer is located at FS313, so that each of the three accelerometers has a different physical location.

Table 4-3. Aeroelastic coefficients of acceleration responses.

Normal Accelerometer					
Sensor Configuration	$x_{n_z}$ (ft)	$z_{n_z}$ (ft)	$\partial h/\partial \eta_1$ (ft)	$\partial h/\partial \eta_2$ (ft)	$\partial h/\partial \eta_3$ (ft)
FS77	20.25	0.429	$4.775(10^{-3})$	$-1.467(10^{-2})$	$-8.333(10^{-4})$
SFCS (FS77)	20.25	0.429	$4.775(10^{-3})$	$-1.467(10^{-2})$	$-8.333(10^{-4})$
FS313	0.583	0.0	$-1.840(10^{-3})$	$5.006(10^{-3})$	$-3.075(10^{-3})$
Lateral Accelerometer					
Sensor Configuration	$x_{n_y}$ (ft)	$z_{n_y}$ (ft)	$\partial h/\partial \eta_6$ (ft)		
FS77	20.25	0.429	$-3.885(10^{-4})$		
SFCS (FS186)	11.142	0.654	$5.181(10^{-4})$		
FS313	0.583	0.0	$9.066(10^{-5})$		
Longitudinal Accelerometer					
Sensor Configuration	$x_{n_x}$ (ft)	$z_{n_x}$ (ft)			
FS77	20.25	0.429			
SFCS (FS313)	0.583	0.0			
FS313	0.583	0.0			

\* Estimated coefficient.

Table 4-4. Aeroelastic coefficients of gyro responses.

Pitch-Rate Gyro			
Sensor Configuration	$\partial\theta/\partial\eta_1$ (rad)	$\partial\theta/\partial\eta_2$ (rad)	$\partial\theta/\partial\eta_3$ (rad)
FS77	$-3.608(10^{-4})$	$2.239(10^{-3})$	$-1.14(10^{-4})^*$
SFCS(FS383)	0.0	$-7.11(10^{-4})$	$1.14(10^{-4})$
FS313	$-2.33(10^{-4})$	$-2.64(10^{-4})$	0.0
Roll-Rate Gyro			
Sensor Configuration	$\partial\phi/\partial\eta_4$ (rad)	$\partial\phi/\partial\eta_5$ (rad)	$\partial\phi/\partial\eta_6$ (rad)
FS77	$-5.5(10^{-4})$	$6.3(10^{-4})$	$2.9(10^{-3})$
SFCS(FS77)	$-5.5(10^{-4})$	$6.3(10^{-4})$	$2.9(10^{-3})$
FS313	$-3.33(10^{-4})$	$5.333(10^{-4})$	$2.267(10^{-3})$
Yaw-Rate Gyro			
Sensor Configuration	$\partial\psi/\partial\eta_6$ (rad)		
FS77	$-1.4(10^{-3})$		
SFCS(FS383)	$6.0(10^{-5})$		
FS313	$-3.5(10^{-4})$		

\* Estimated coefficient.

The normal accelerometer is located at either FS77 or FS313, and the coefficient of the first longitudinal-structural mode changes sign between these two locations, with its magnitude at FS77 about three times greater than that at FS313. This is also true of the coefficient of the second longitudinal-structural mode. The coefficient of the third longitudinal-structural mode at FS313 is estimated from data given in References 2 and 3, since the generalized shape of this mode is not given. The coefficient of the third longitudinal-structural mode has the same sign at both accelerometer locations; however, its magnitude is four times greater near the cg.

Three different lateral-accelerometer locations exist for the three sensor locations; FS77, FS186, and FS313. This sensor is affected only by the first fuselage lateral-bending mode,  $\eta_6$ : its coefficient is negative when located forward, and positive when located near the cg. The longitudinal-accelerometer is not affected by the structural modes (as discussed previously).

The pitch-rate gyro is located differently for each of the three sensor configurations investigated; FS77, FS313, or FS383. The first longitudinal-directional mode coefficient is negative or equal to zero, but becomes more positive for distances further from the nose of the aircraft. A negative slope with increasing aft distances characterizes the second mode coefficient, and with a sign change occurring between FS77 and FS313. The slope of the third mode coefficient is positive with increasing aft distances, and with a sign change at FS313. This coefficient is estimated for FS77, due to a lack of data in References 2 and 3.

All three lateral-directional modes affect the roll-rate gyro, which is either at FS77 or FS313. No sign changes are encountered among the mode coefficients, but in each case the magnitude decreases with increasing aft distances. Only the first fuselage lateral-bending mode,  $\eta_6$ , affects the yaw-rate gyro, and the coefficient of its effect becomes more positive with increasing aft distances. A change in the sign of this variable occurs between FS313 and FS383.

The parameters selected for the roll-rate gyro and lateral-accelerometer navigation models are given in Tables 4-5 and 4-6. Refer to Figures 3-8 and 3-9 to ascertain where these parameters apply in the sensor models. The time constant of the lag in the accelerometer model,  $\tau$ , is selected to be very small, ( $10^{-6}$ ), to essentially eliminate the lag from the sensor model. The parameters for all of the navigation gyros and accelerometers are the same as those listed in Tables 4-5 and 4-6 for the computer runs which demonstrate the MIRA simulation capability.

Table 4-5. Ring-laser roll-rate-gyro nominal parameters.

Parameter	Symbol	Value
Misalignment Coefficients	$\mu_1, \mu_2$	$5(10^{-5})$ rad
Scale Factor	$SF_{PG}$	131,328.387 pulses/rad
Bias	$\Delta b_{PG}$	0.006367 $\Delta t$ pulses [0.01°/h]
Scale Factor Error	$\epsilon_{PG}$	$5(10^{-6})$ rad/pulse

Table 4-6. Quartz-flexure lateral-accelerometer nominal parameters.

Parameter	Symbol	Value
Misalignment Coefficients	$\zeta_1, \zeta_2$	$5(10^{-5})$ rad
Time Constant of Lag	$\tau$	$1(10^{-6})$ s
Scale Factor	$SF_{n_y}$	1000 pulses/ft/s
Bias	$\Delta b_{n_y}$	0.0016 $\Delta t$ ft/s [50 $\mu g$ ]
Crosscoupling Coefficients	$C_{yx}$	$\frac{6.1(10^{-6})}{\Delta t}$ 1/ft/s [19.6(10 <sup>-5</sup> )* $\frac{\text{rad}}{g}$ ]
Nonlinearity Coefficient	$C_{yy}$	$1.25(10^{-6})$ 1/ft/s
Scale-Factor Error	$\epsilon_{n_y}$	0.0001 ft/s/pulse

#### 4.3 MIRA Simulation Results

Figures 4-2, 4-3, and 4-4 contain the first set of results which demonstrates the MIRA simulation capability. In each case, the sensors are located at the stations recommended for the SFCS program, as indicated in Table 4-1. The figures differ in that the results shown in Figure 4-2 assume perfect sensors with the vehicle flying in a nonturbulent environment, while those presented in Figure 4-3 are obtained using realistic models for the navigation and flight-control sensors with the vehicle flying in a lightly turbulent environment. Figure 4-4 shows the results obtained when common sensors are used for both navigation and flight control. Again the vehicle is flying in light turbulence.

\* This value is about 10 times larger than that of state-of-the-art equipment.



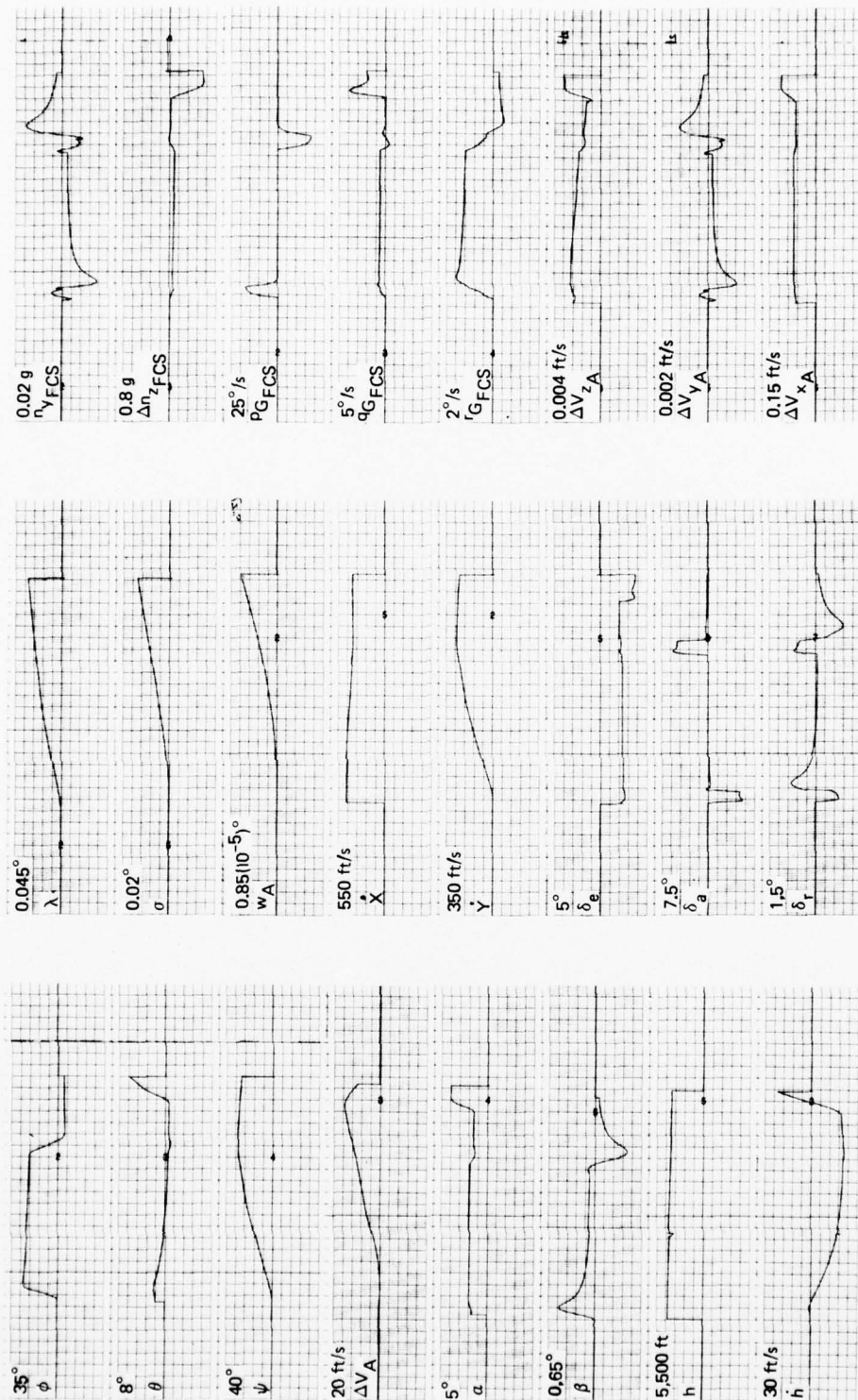


Figure 4-2. MIRA simulation responses—perfect sensors at SFCS location (no turbulence).

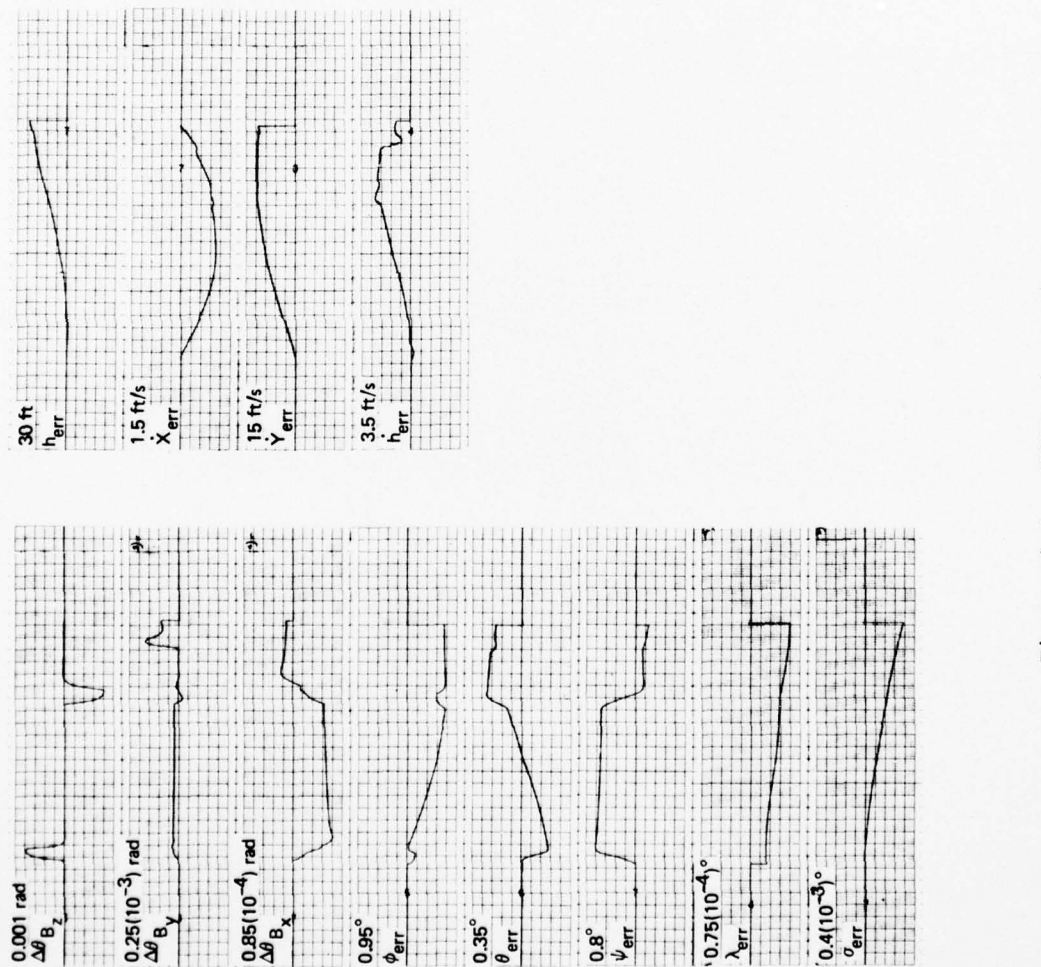


Figure 4-2. MIRA simulation responses—perfect sensors at SFCS location (no turbulence) (cont.).

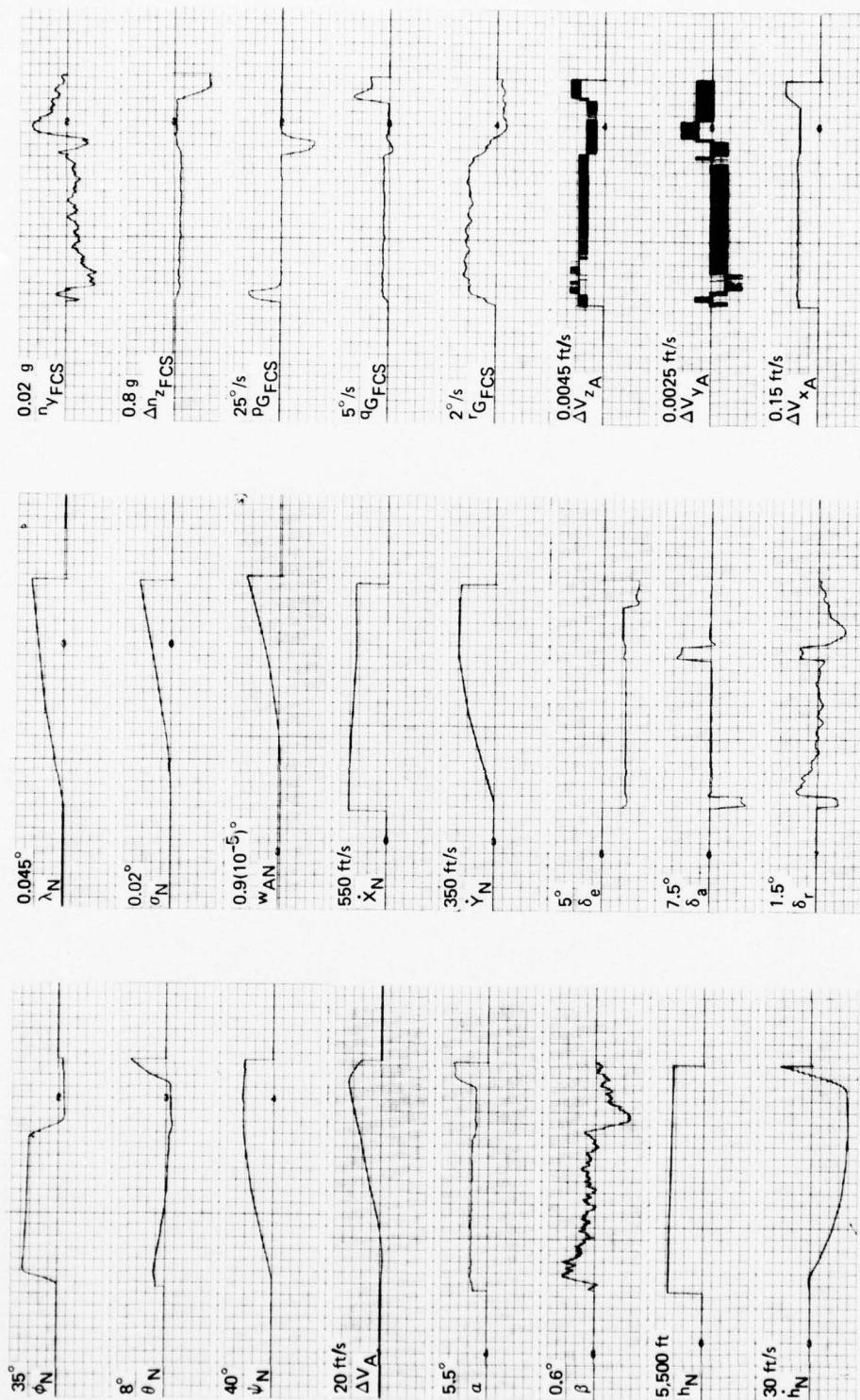


Figure 4-3. MIRA simulation responses—sensors at SFCS locations (turbulent environment).

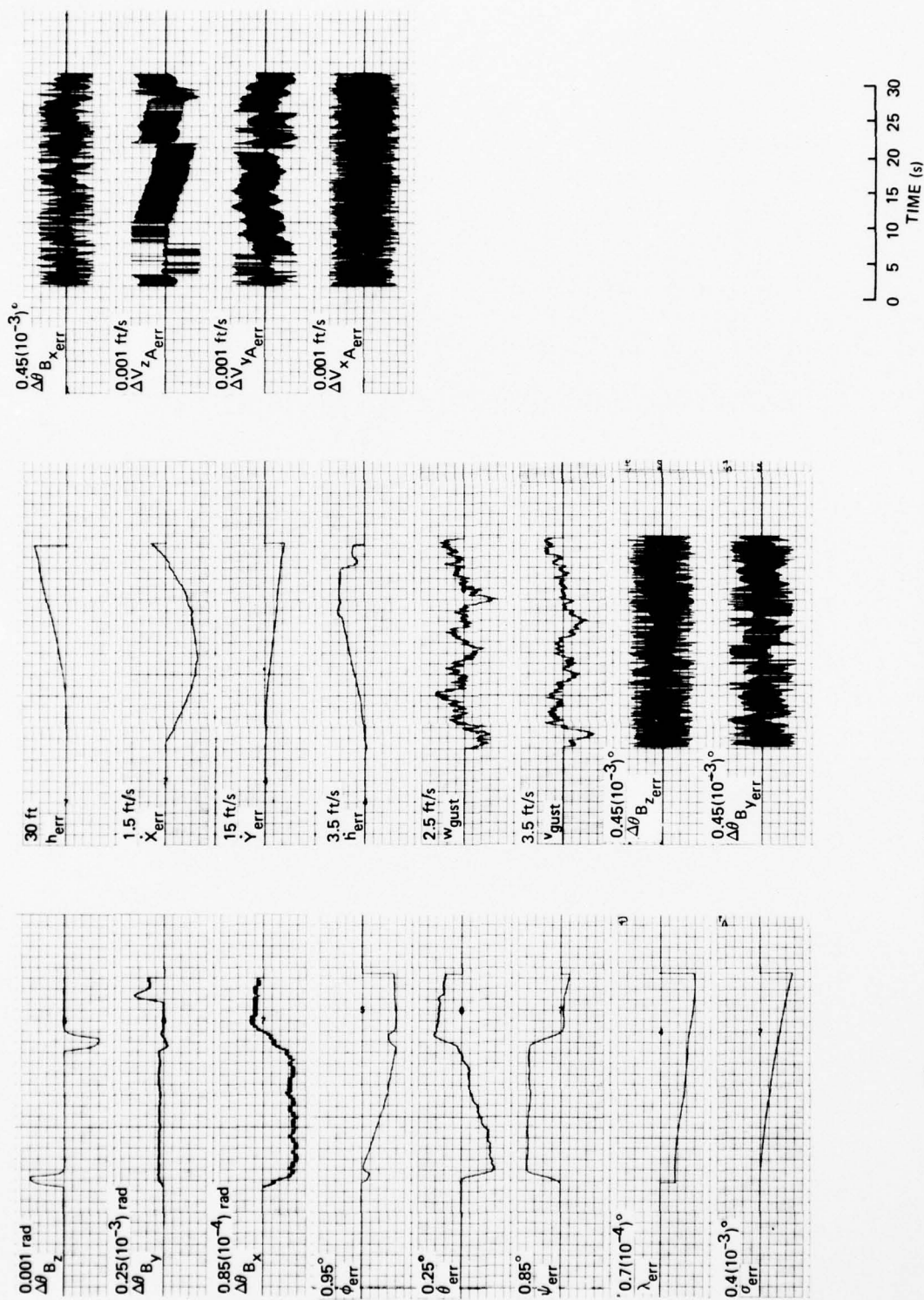


Figure 4-3. MIRA simulation responses—sensors at SFCS locations (turbulent environment) (cont.).



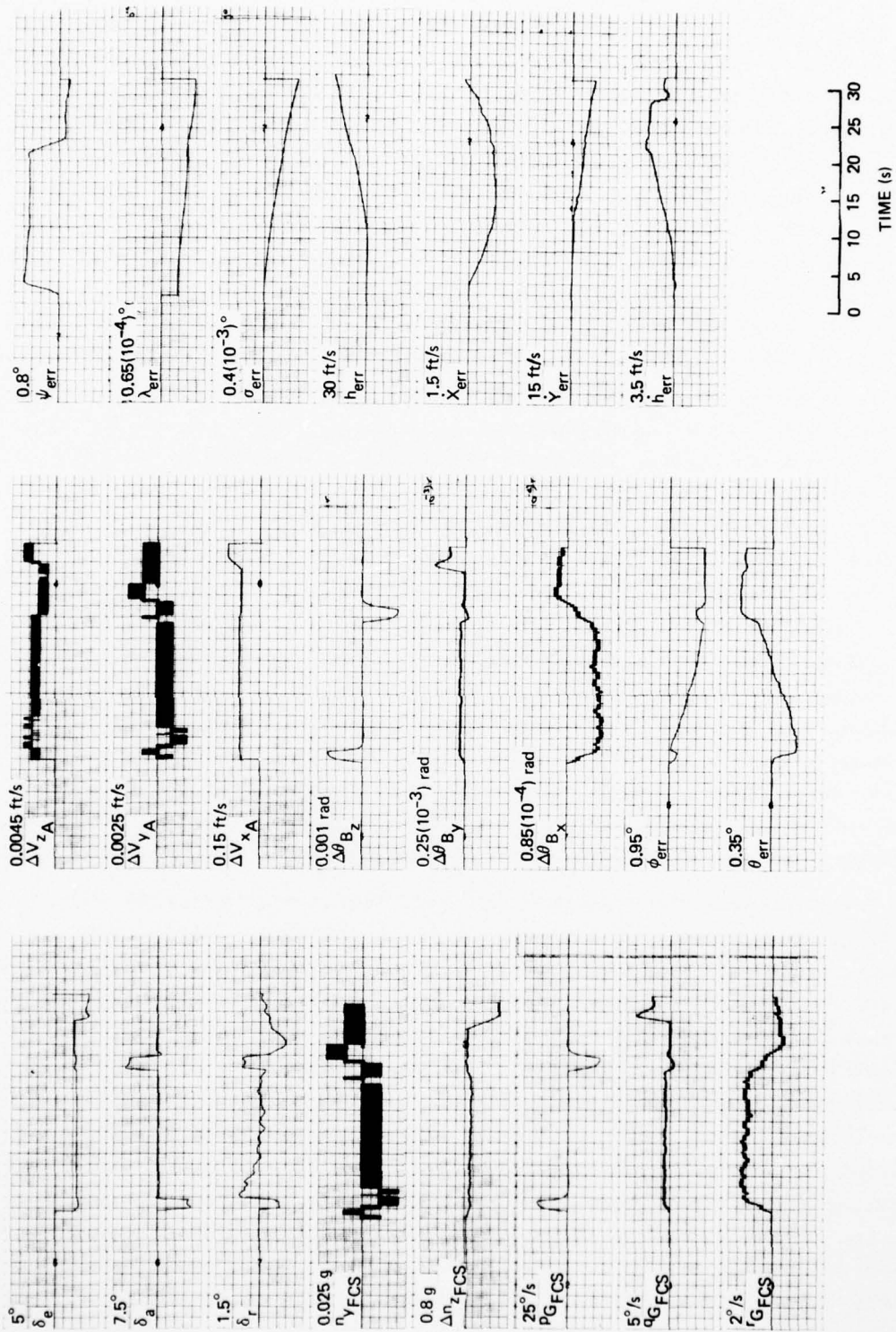


Figure 4-4. MIRA simulation responses—common navigation and flight-control sensors at SFCS locations (turbulent environment).



The basic vehicle responses for the inputs of Figure 4-1, are shown in Figure 4-2. The vehicle achieves a bank angle of approximately 32.5 degrees due to the application of the positive roll-stick pulse. This variable bleeds off slightly from this value until the negative lateral-stick pulse is applied after which it becomes slightly negative. The yaw angle gradually builds up to about 37.5 degrees, and remains essentially constant after the negative lateral stick is applied. The pitch angle decreases slightly from its trim value due to a loss of lift. The longitudinal-stick input is not large enough to maintain a constant  $\theta$  during the turning portion of flight. However,  $\theta$  increases substantially with the application of the longitudinal-stick step input. A gradual buildup in velocity occurs as the pitch angle decreases until the longitudinal-stick step input is applied, at which time this variable decreases slightly. The angle of attack is essentially constant at its trim value, until the longitudinal-stick step input, when it undergoes a step change. During most of the simulation run,  $\beta$  is approximately zero, and achieves its largest values when the lateral-pulse inputs are applied. A decrease in altitude and negative rate of altitude change results during the turning portion of flight. The application of the longitudinal-stick step input causes a positive  $\dot{h}$ , and a subsequent slight increase in altitude at the end of the run. The latitude, longitude, and wander angle undergo positive ramp increases with time. The north-pointing earth velocity of the vehicle decreases slightly from its trim value, while the east component of the velocity of the vehicle, with respect to the earth, increases with time during the turning portion of flight, and then levels off.

The control-surface deflections and flight-control-system sensor signals are also presented in Figure 4-2. A pulse-aileron-surface deflection and a corresponding pulse-roll-rate-gyro sensor signal are produced by the lateral-stick input. A well-damped roll mode is evident from these responses. The roll-to-yaw crossfeed and feedback system provides a rudder-surface deflection which, in turn, results in an essentially constant yaw rate during the initial portion of the time history. The initial negative rudder deflection causes an initial negative lateral-acceleration transient. After this, the rudder-surface deflection reflects the envelope of the lateral-accelerometer signal, until the negative lateral-stick input, when the time history repeats. From these responses, the Dutch Roll mode appears to be well-damped. The effects of the structural-mode signals are evident in the  $n_{yFCS}$  signal to a small extent. Longitudinally, a constant pitch rate

and a constant upward normal acceleration are produced by the longitudinal-stick command during the initial portion of the time history. The application of the large longitudinal-stick step input then excites the short-period mode. The high damping of the short-period mode is evident from these responses.

The input variables to the navigation-system model are considered next. Since perfect-sensor models are used in this case, these signals are repeats of the flight-control-system sensor time histories with the appropriate axes transformation between the vehicle equations of motion and the navigation-system model. The errors in the Euler angles are presented in Figure 4-2. The bank-angle error increases linearly during the turning portion of flight, and then levels off near the end of the simulation run. On the other hand, the yaw-angle error remains essentially constant during the time when the vehicle is turning, and then becomes approximately zero when the wings are leveled off. The pitch-angle error goes negative initially, and increases linearly with time until the longitudinal-stick input is removed. After this, it jumps to a constant value. The errors in longitude, latitude, and altitude all increase with time. The initial offset in the latitude error is due to the fact that the initial value of the navigation-system latitude is obtained by inverse trigonometric functions; thus, truncation and round-off effects are present. The error in wander angle is not presented in Figure 4-2, because it is of such a small magnitude. A parabolic shape characterizes the error in the north component of the earth-relative velocity, while the east component of the earth-relative velocity increases with time. The effects of the low frequency of the navigation-system computations is evident in the step-like responses present in the error in  $\dot{h}$  time history.

A set of time histories, corresponding to those of Figure 4-2, is presented in Figure 4-3 for the case where the vehicle is flying in lightly turbulent air and the navigation and flight-control sensors are not perfect. Furthermore, the variables computed by the navigation-system model are presented in lieu of the corresponding vehicle variables.

The major differences between the responses of Figures 4-2 and 4-3 are evident in the navigation-system input variables which show the effect of the quantization occurring in the sensor models and the turbulence. The turbulence input signals are also presented in Figure 4-3. A measure of their impact on the sensor signals can be obtained by

comparing the flight-control-system sensor responses of Figures 4-2 and 4-3. Other time histories, greatly affected by the turbulence, are the sideslip angle and the rudder deflection. The navigation-system-model output variables are presented in Figure 4-3 in lieu of the corresponding vehicle signals. These variables, as well as the MIRA simulation-error variables, closely resemble the corresponding variables of Figure 4-2. Perhaps the major differences are evident in the  $\dot{h}$  signal, where the effect of the low navigation-system computation frequency manifests itself, and in the pitch-attitude error signal which is corrupted by turbulence. The error signals in Figure 4-3 are either of the same or smaller magnitude than the corresponding signals of Figure 4-2.

Additional variables reflecting the errors between the navigation perfect-sensor signals and their realistic model counterparts are also presented in Figure 4-3 to give the reader an idea as to the magnitude and shape of these differences.

Figure 4-4 contains the responses obtained when the navigation sensors are used for both navigation and flight-control functions. The sensors are located at the positions determined for the SFCS program; light turbulence is also present here. The most striking aspect of Figure 4-4 is evident in the flight-control-system signals, which are now the same as the navigation-sensor signals, except for the appropriate coordinate transformation. The flight-control sensor signals now reflect the effects of the sensor-model errors and, in particular, the quantization which takes place. However, the control-surface deflections do not noticeably reflect the quantization effects present in the flight-control signals which drive the surfaces. The flight-control system filters these high-frequency effects out. Once again, the navigation error signals have the same characteristic shapes and magnitudes previously evident in Figure 4-3. The use of common sensors (Figure 4-4) resulted in slightly smaller errors in latitude, altitude, and  $\dot{X}$  when compared to the responses of Figure 4-3 which were obtained with independent sensors. Conversely, smaller errors in  $\phi$ ,  $\theta$ , longitude, and  $\dot{Y}$  are achieved using independent sensors. The errors in  $\psi$  and  $\dot{h}$  are about the same in both cases. These results reinforce the feasibility of the MIRA concept when considered from a navigation-error point of view, although only limited conclusions can be drawn due to the short duration of the simulation runs.

Structural-mode excitation is considered in Figures 4-5, 4-6, and 4-7. For these cases, the sensors are all located at FS77. Figure 4-5 resulted from a nonturbulent environment, and the use of perfect-sensor models. A turbulent environment and nonperfect-sensor models led to the results presented in Figure 4-6. The results shown in Figure 4-7 are obtained with navigation sensors used for both navigation and flight-control purposes with the vehicle flying in gusty air.

In Figure 4-5, the structural modes are excited only by the control-surface deflections with the lowest frequency longitudinal- and lateral-directional modes excited most. The generalized bending-mode coefficients (i.e.,  $\eta_1, \eta_2, \dots$ ) take on the shape of the dominant control-surface deflection exciting them. For example, all of the longitudinal-bending-mode coefficients have the shape of the incremental horizontal-stabilator deflection. The fuselage first torsion mode,  $\eta_4$ , has the shape of the aileron surface deflection, while the wing first asymmetric-bending mode,  $\eta_5$ , and the fuselage first lateral-bending mode,  $\eta_5$ , and the fuselage first lateral-bending mode,  $\eta_6$ , both reflect the shape of the rudder-surface deflection.

The time histories of Figure 4-6 correspond to those already presented in Figure 4-5. A more constant excitation of the structural modes occurs because of the turbulent environment in which the vehicle is flying. In the majority of cases, the excitation due to the turbulence is much less than that due to the control-surface deflections. However, this is not true in the case of  $\ddot{\eta}_5$  and  $\dot{\eta}_5$ , where the excitation due to turbulence nearly exceeds that due to the control-surface deflections.

Figure 4-7 contains the time histories for the third member of this group of results which were obtained using common sensors for both the navigation and flight-control systems. In general, the results of Figure 4-7 are quite similar to those of Figure 4-6. The most noticeable difference is an increase in the level of the structural-mode excitation, which is particularly evident in the mode rates and accelerations. This is believed to be due to quantization occurring in the navigation-sensor models. The structural modes are excited by the derivatives of the control-surface deflections, and the effects of the quantization are more pronounced in these signals than in the control-surface deflections themselves. This result could have a significant effect on the feasibility of the MIRA concept for vehicles which tend



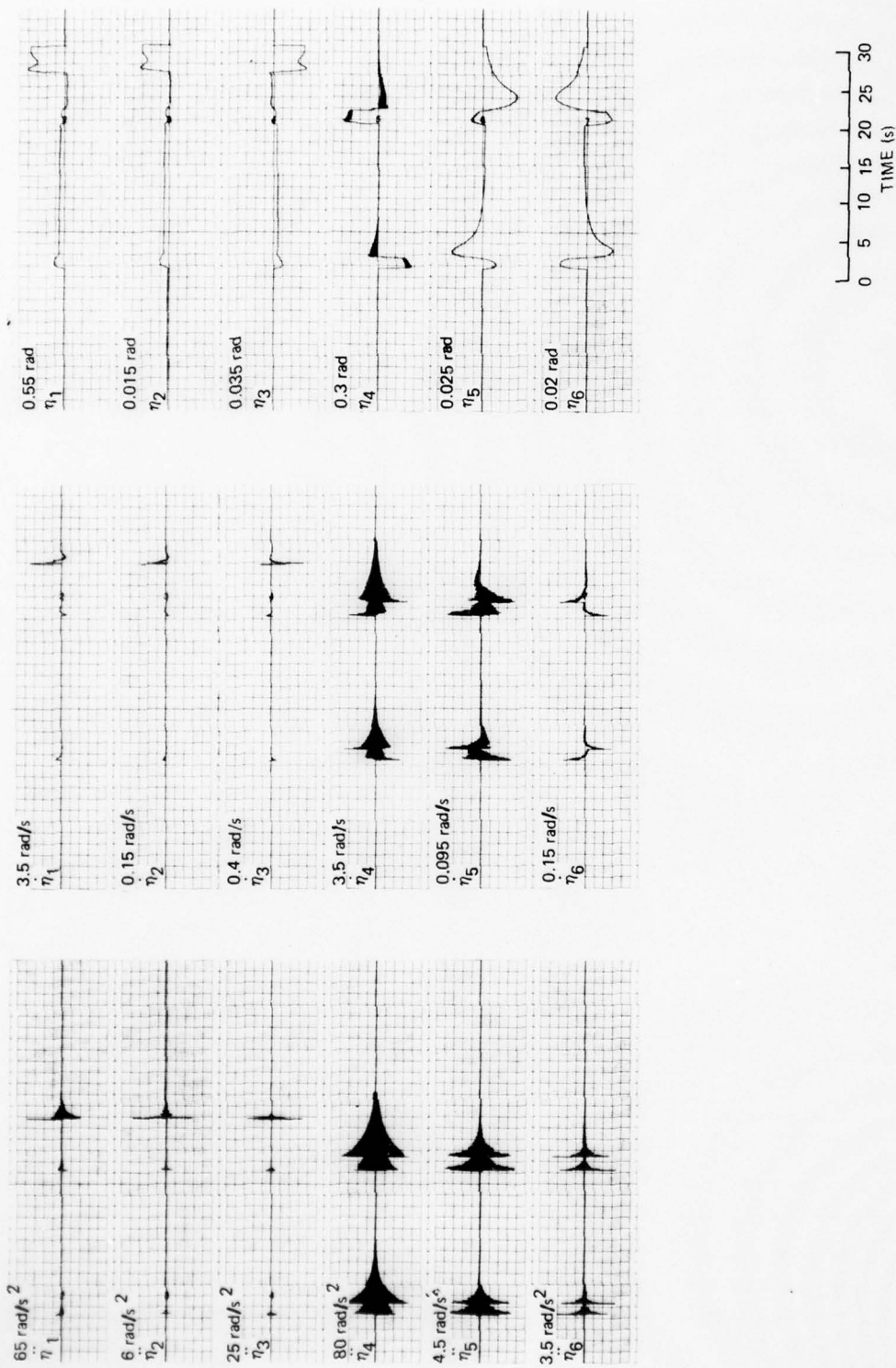


Figure 4-5. Structural-mode responses—perfect sensors at FS77 (no turbulence).



AD-A044 849

CHARLES STARK DRAPER LAB INC CAMBRIDGE MASS  
DEVELOPMENT OF CAPABILITY FOR MULTIFUNCTION INTEGRATED REFERENC--ETC(U)  
JUL 77 K DALY, R NURSE, G SCHMIDT, P MOTYKA F33615-76-C-1216

F/G 1/3

UNCLASSIFIED

R-1042

AFAL-TR-77-64

NL

2 OF 2  
ADA  
044849



END  
DATE  
FILMED

10-77  
DDC

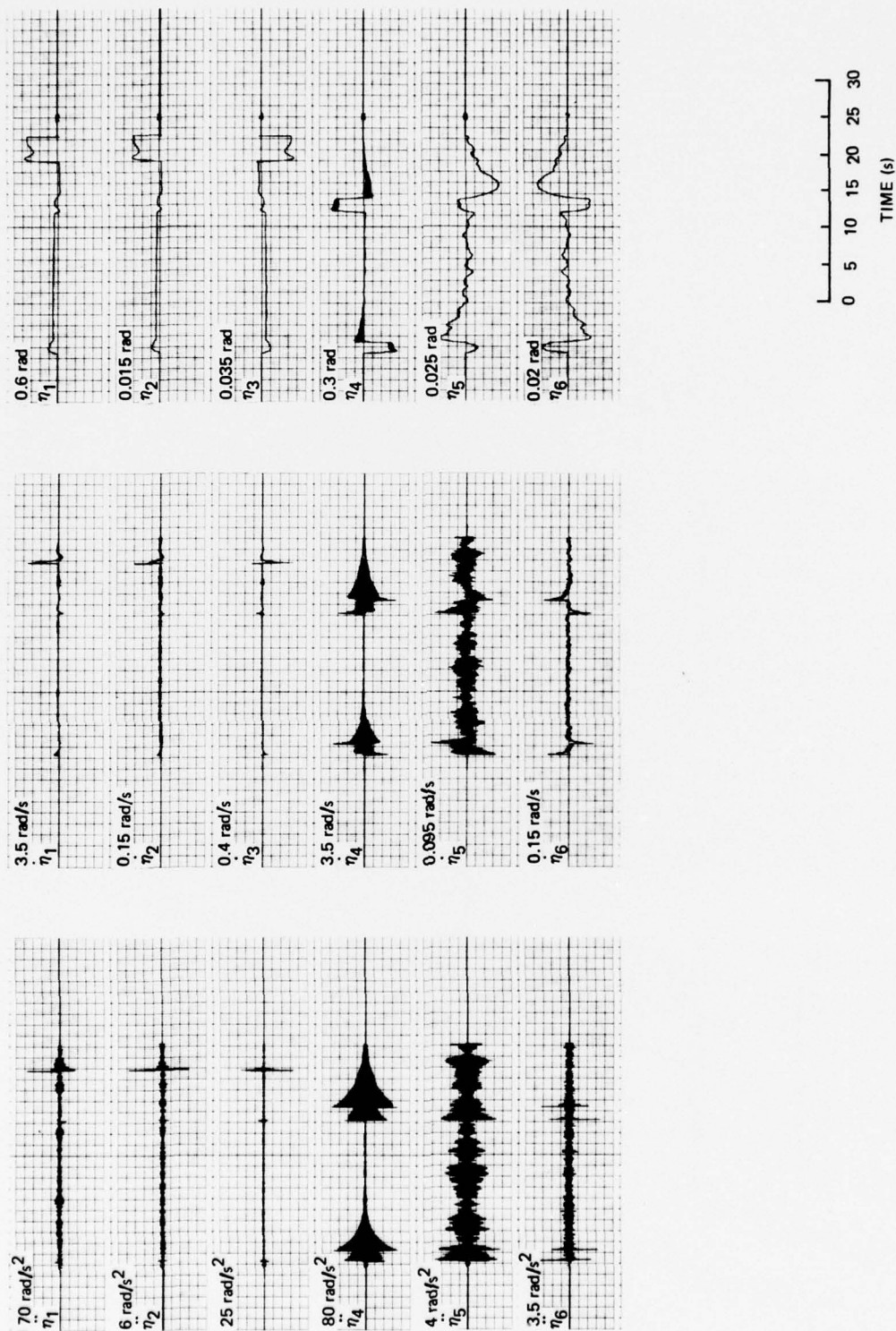


Figure 4-6. Structural-mode responses—sensors at FS77 (turbulent environment).

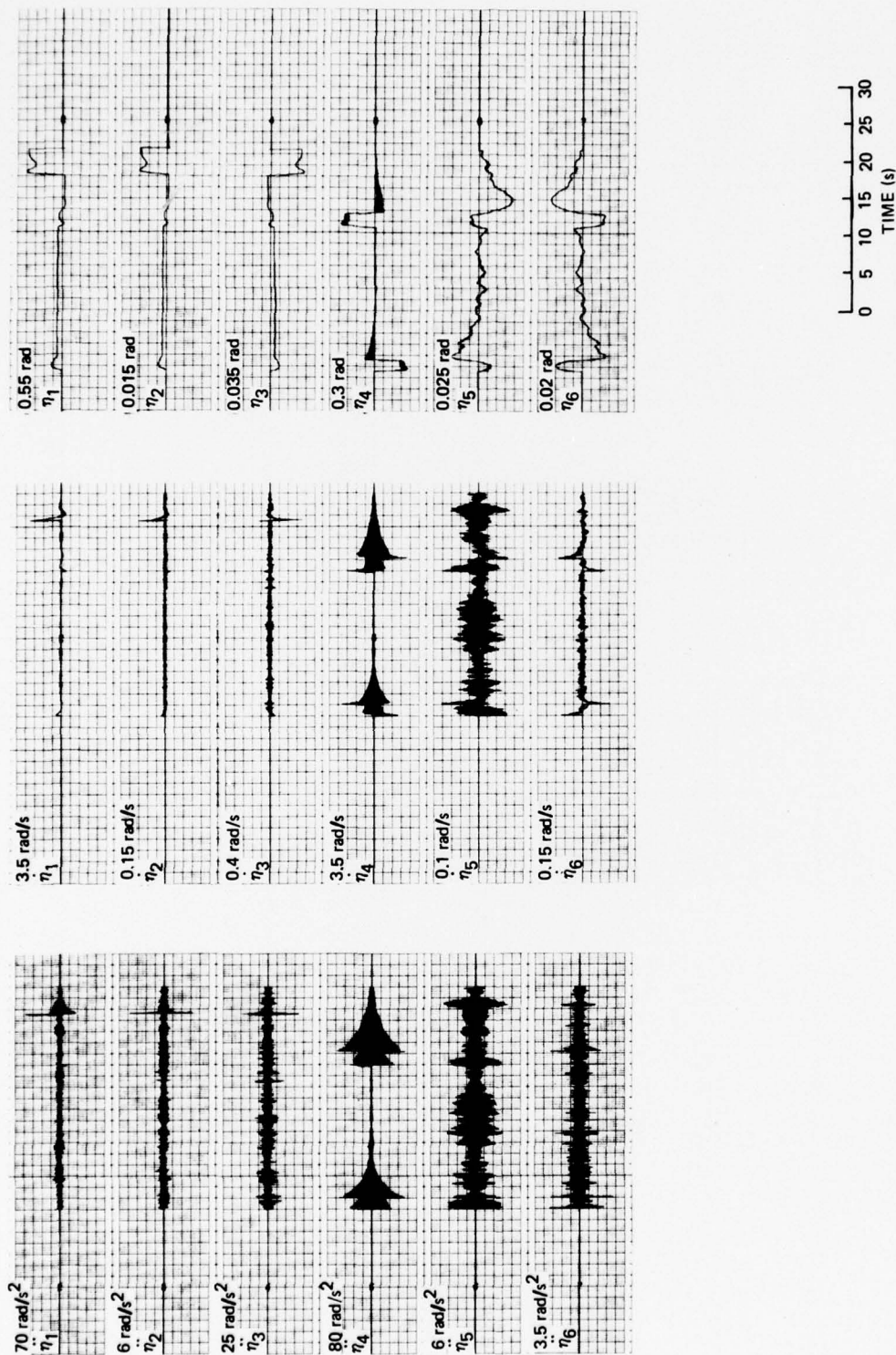


Figure 4-7. Structural-mode responses—common navigation and flight-control sensors at FS77 (turbulent environment).

to be more flexible since the structural-mode rates and accelerations directly affect the sensor signals.

The last set of data included herein, and which demonstrates the capability of the MIRA simulation, is presented in Figures 4-8, 4-9, and 4-10. All of these responses have been obtained with the vehicle flying in a turbulent environment. The responses of Figure 4-8 provide a basis for the present discussion, and have been obtained with the flight-control sensors located at the SFCS locations and the navigation sensors located at FS313, just forward of the vehicle cg. For Figure 4-9, common navigation and flight-control sensors located at FS313 have been used, while for Figure 4-10, the common navigation and flight-control sensors are located at FS77. The responses of Figure 4-4, obtained with common navigation and flight-control sensors located at the SFCS stations, are also pertinent to the present discussion.

One difference among the responses of the four cases just mentioned is in the rudder-control-surface deflection. The initial peak of this signal becomes less sharply defined as the sensor is located farther forward of the cg. The lateral-accelerometer signal is also different among these cases in that the initial portion of the transient has different signs. A difference also exists in the yaw-rate-gyro output. These differences arise because of  $\dot{r}$  and  $\dot{p}$  contributions to the lateral acceleration, which are measured by sensors at locations different from the vehicle cg. The lateral-acceleration signal drives the rudder surface through the augmentation system which, in turn, affects the yaw-rate response. Certainly, the lateral-directional handling qualities will be affected by a change in the location of the lateral accelerometer. However, this subject has not been explored during the course of this effort. It should be pointed out that the designer of the flight-control system for a MIRA configured vehicle also has the liberty of adjusting the roll-to-yaw crossfeed network of the augmentation system in order to help improve the handling qualities of the vehicle.

A comparison of the  $\delta_e$ ,  $q$ , and  $\Delta n_z$  responses of Figures 4-8 and 4-9 (for which the normal accelerometer is located at FS313) with those of Figure 4-4 and 4-10 (for which the normal accelerometer is located at FS77) reveals that the responses of the system with the more aft-located normal accelerometer are more lightly damped than the others. The difference in damping is due to the  $\dot{q}$  contribution to the normal acceleration, which is sensed by an accelerometer located in a position



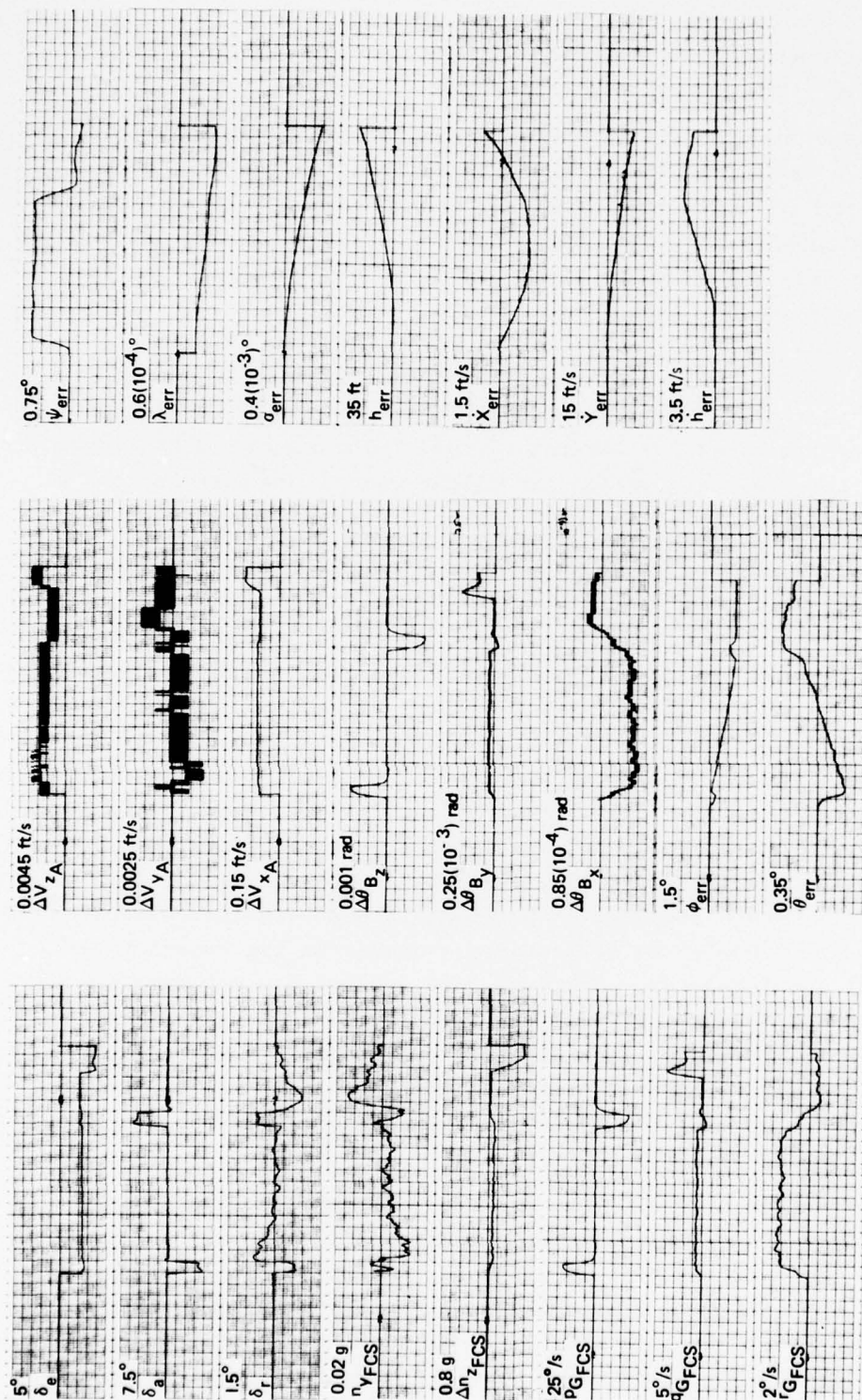


Figure 4-8. MIRA simulation responses—navigation sensors at FS313, and flight-control sensors at SFCs locations (turbulent environment).



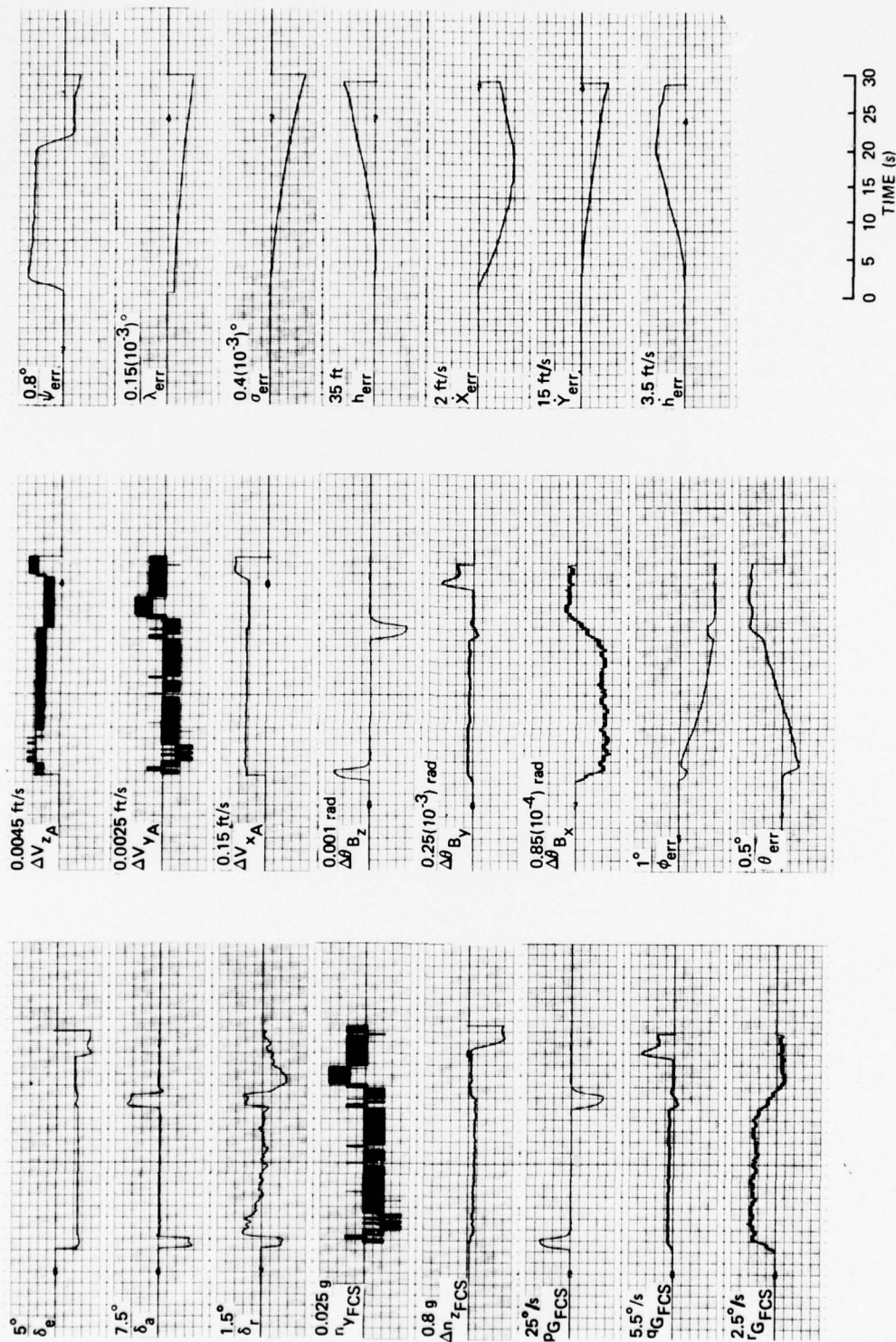


Figure 4-9. MIRA simulation responses—common navigation and flight-control sensors FS313 (turbulent environment).

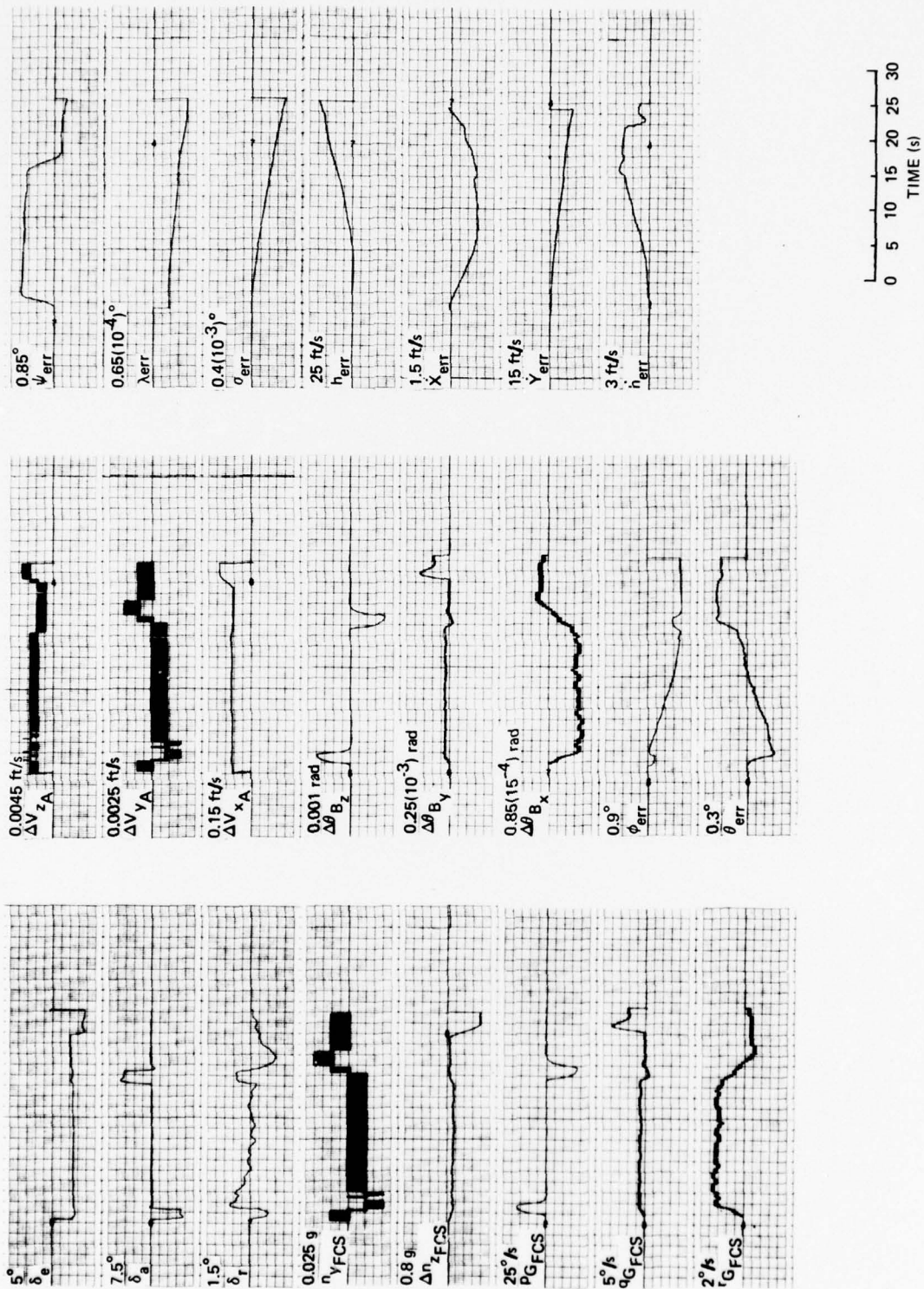


Figure 4-10. MIRA simulation responses—common navigation and flight-control sensors at FS77 (turbulent environment).

forward of the aircraft cg. From the point of view of handling qualities, it is desirable to locate the normal accelerometer forward of the cg in order to take advantage of the increase in short-period damping which results. The fact that the normal-accelerometer location selected for the SFCS configuration is far forward of the cg reinforces the idea that this is the best general location for this sensor.

A noticeable difference is not evident among the roll-rate response of the vehicle for the four cases under consideration. This is undoubtedly due to the fact that the roll-rate-gyro signal is not affected by location to the extent that the accelerometer signals are. The effects of location manifest themselves in the roll-rate-gyro signal only through the structural-mode contributions, which are nearly negligible for the model vehicle.

Although it is dangerous to draw hard and fast conclusions from the limited amount of data presented herein, a comparison of the errors obtained with the four sensor configurations under consideration is made in an attempt to reach some meaningful conclusions. A simple criterion is used in this investigation. The magnitudes of the maximum errors and errors at the final time are compared. Equal weight is given to each parameter. Tables 4-7 and 4-8 contain the pertinent error data.

Table 4-7. Magnitude of maximum errors of MIRA simulation runs.

		Sensor Configuration			
Flt. Ctl. Sens. Loc.		SFCS	FS313	FS77	SFCS
Nav. Sens. Loc.		FS313	FS313	FS77	SFCS
Error	Units	NCS*	CS*	CS*	CS*
$\dot{h}$	ft/s	3.1215	3.0161	2.7541	3.1446
$\dot{Y}$	ft/s	11.4163	11.7031	10.2139	10.6445
$\dot{X}$	ft/s	1.1621	1.9081	1.1576	1.0860
$\phi$	deg	1.0013	0.9585	0.8815	0.9411
$\theta$	deg	0.3370	0.4799	0.2666	0.3078
$\psi$	deg	0.7475	0.7805	0.8000	0.7744
$\lambda$	deg	$5.905(10^{-5})$	$1.054(10^{-4})$	$6.427(10^{-5})$	$6.155(10^{-5})$
$\sigma$	deg	$3.942(10^{-4})$	$3.956(10^{-4})$	$3.990(10^{-4})$	$3.896(10^{-4})$
h	ft.	31.6284	30.6637	23.7087	27.2142

\* CS = Common sensors for navigation and flight control.  
NCS = No common sensors for navigation and flight control.



Figure 4-8. Magnitude of final errors MIRA simulation runs.

		Sensor Configuration			
Flt. Ctl. Sens. Loc.		SFCS	FS313	FS77	SFCS
Nav. Sens. Loc.		FS313	FS313	FS77	SFCS
Error	Units	NCS*	CS*	CS*	CS*
$\dot{h}$	ft/s	2.1651	2.0373	0.8269	1.1269
$\dot{Y}$	ft/s	11.4163	11.7031	10.2139	10.6445
$\dot{X}$	ft/s	0.7339	1.1114	0.1489	0.2453
$\phi$	deg	0.9765	0.9309	0.8388	0.8957
$\theta$	deg	0.2145	0.4336	0.2191	0.2470
$\psi$	deg	0.2171	0.3436	0.2843	0.2249
$\lambda$	deg	5.660(10 <sup>-5</sup> )	1.054(10 <sup>-4</sup> )	6.386(10 <sup>-5</sup> )	6.087(10 <sup>-5</sup> )
$\sigma$	deg	3.942(10 <sup>-4</sup> )	3.956(10 <sup>-4</sup> )	3.991(10 <sup>-4</sup> )	3.896(10 <sup>-4</sup> )
h	ft	31.6284	30.6637	23.7087	27.2142

\* CS = Common sensors for navigation and flight control.  
 NCS = No common sensors for navigation and flight control.

An investigation of the data contained in these tables indicates that the navigation errors are smallest for the cases where the sensors are located at FS77 and the SFCS stations. For example, the errors in  $\dot{h}$  and h are significantly smaller for the case with the sensors colocated at FS77. This configuration also resulted in the smallest errors in  $\phi$  and  $\dot{X}$  for the four cases being considered. These advantages are counterbalanced because longitude, latitude, and yaw-angle errors are the worst, or close to it. On the other hand, the errors obtained for the SFCS configured vehicle are the most consistent of those obtained, being neither the best nor the worst, in most cases. These advantages are obtained for the cases with the sensors located at FS77 and the SFCS stations are so close in nature that it is quite possibly due to the location of the normal accelerometer at FS77 in both cases, and the location of the lateral accelerometer close to FS77 in the SFCS configuration.

The configuration with independent flight-control sensors at the SFCS locations and the navigation sensors colocated at the cg appears to be the next best system of those four considered. The smallest

errors in latitude and heading angle are obtained with this configuration. It is offset by the fact that this configuration resulted in the worst altitude and roll-angle errors, and the next to the worst errors in  $\dot{h}$ ,  $\dot{Y}$ , and  $\dot{X}$ .

The configuration with the common-navigation and flight-control sensors located at FS313 faired worst of all. The largest or next to the largest errors are obtained with this configuration in most of the variables considered (e.g., the Euler angles, longitude,  $\dot{h}$ , and  $\dot{Y}$ ). Significantly larger errors in latitude and  $\dot{X}$  also resulted. This sensor arrangement did not result in the smallest errors for any of the variables considered.

The results of the investigation indicate that a forward location is best for the accelerometers from both a navigation and a handling qualities standpoint. It is better if the accelerometers are colocated; however, some freedom is allowed in the placement of these sensors to minimize the structural-mode pickup with minor or no degrading effects. Although proven in this study, there is also a tendency to believe that the steady-state long-term navigation accuracy will be affected relatively little by the placement of the sensors in the forward portions of the fuselage. That is, the  $\dot{q}$ ,  $\dot{r}$ , and  $\dot{p}$  terms measured by forward-placed accelerometers over a long mission would be expected to be negligible. More flexibility is allowed in the placement of the rate gyros since the quantity that they measure is dependent upon location only to the extent that the structural modes affect them.

#### 4.4 Conclusions from MIRA Simulation Results

In summary, the following major conclusions can be drawn from the data thus far presented.

- (1) The capability of the MIRA simulation developed by CSDL has been demonstrated.
- (2) The feasibility of the MIRA concept is reinforced, since nearly identical results are obtained using independent and common sensors for navigation and flight control.
- (3) Forward fuselage locations appear best for the accelerometers from both a navigation and handling-qualities standpoint based upon the simulation runs performed for this study. Some freedom is allowed in locating these sensors with regard to their structural-mode contamination.



- (4) Flexibility is allowed in the placement of the rate gyros, since the signals that they sense are location-dependent only to the extent that the structural modes affect them.
- (5) The quantization present in the navigation sensor models affects the level of structural-mode excitation. However, for a fairly rigid vehicle this effect does not manifest itself to a great extent in the sensor signals, control-surface activity, or basic vehicle responses.

## SECTION 5

### LIFE-CYCLE COST MODELING AND MECHANIZATION RESULTS

#### 5.1 Introduction

Life-cycle cost (LCC) is defined as the total cost of acquiring a product, establishing the necessary logistics base from which to deploy and use the product, and maintaining the product in operable condition over some prescribed period of time. For purposes of life-cycle costing, a program is often divided into the following phases:

- (1) Conceptual studies.
- (2) Research, development, test, and evaluation (RDT&E).
- (3) Production.
- (4) Operation and maintenance.
- (5) Disposal.

The goal of life-cycle costing (i.e., achieving minimum life-cycle cost) is depicted in Figure 5-1, where costs are shown as a function of mean time between failure (MTBF). For purposes of illustration, the acquisition costs (all costs incurred through production), and operation and maintenance (O&M) costs are shown. The minimum life-cycle cost occurs at the crossover between the acquisition-cost curve and the O&M cost curve. Thus, there is an optimum reliability for a given piece of equipment—that reliability which permits the minimum life-cycle cost.

In the last decade, increasing emphasis has been placed on LCC from several points of view.

- (1) Minimization of LCC should be included as a program goal.
- (2) LCC considerations should be a factor in design and management decisions.
- (3) LCC should be an independent research and data project.
- (4) LCC should be included in the source selection criteria.

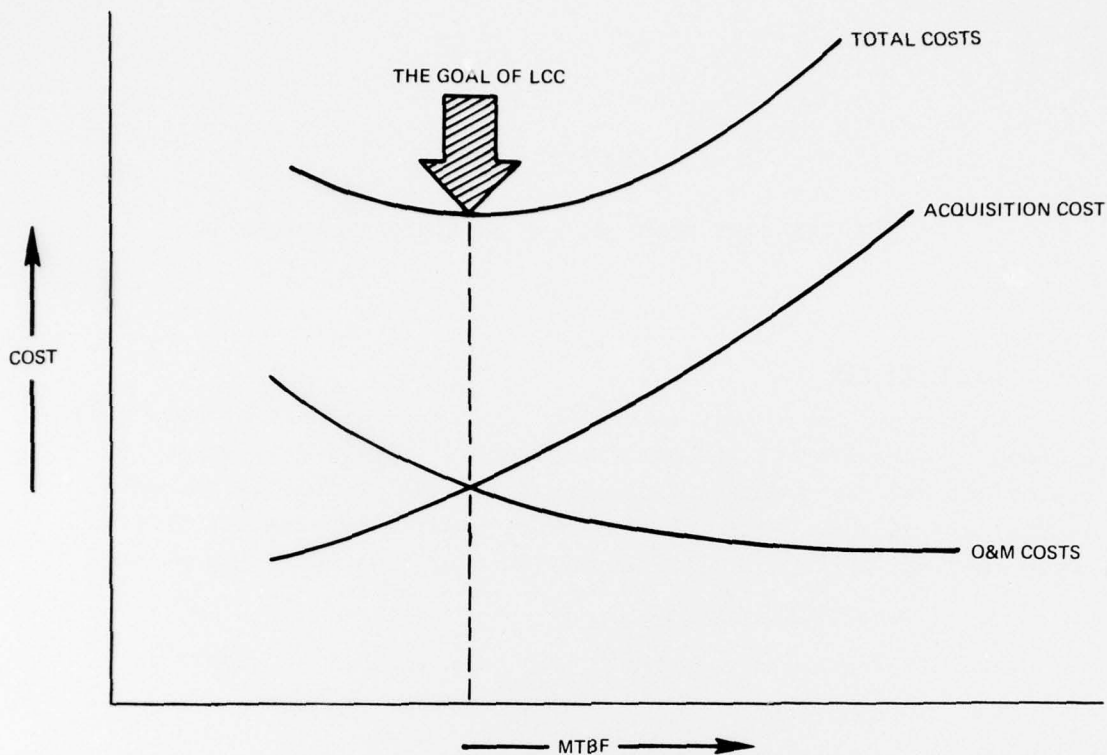


Figure 5-1. The goal of life-cycle cost analysis.

Life-cycle costing is generally accomplished through the application of a diverse spectrum of mathematical models to generate system LCC estimates or to aid in making the design and management decisions affecting LCC. In a recent USAF study<sup>(9)</sup> the following eight categories of LCC models were identified.

- (1) Accounting model - aggregates all costs.
- (2) Economic analysis model - treats the time value of money versus the program schedules.
- (3) Cost-estimating relationship model - relates cost to parameters.
- (4) Reliability/improvement cost model - relates cost to reliability.
- (5) Level-of-repair analysis model - determines minimum-cost-maintenance policy.

- (6) Maintenance-manpower planning model - evaluates alternative maintenance-manpower requirements or effects of alternative equipment designs on maintenance-manpower requirements.
- (7) Inventory management model - determines spare-part stock levels to minimize spares costs.
- (8) Warranty model - evaluates government maintenance versus contractor maintenance under warranty.

## 5.2 Objective

The goal of the life-cycle-costing effort in MIRA is the development of LCC techniques as design tools. The traditional approach in the application of LCC is to sum all the costs which would be included if a proposed equipment design were put into production. In this context, LCC becomes an important source selection criterion and in some instances may be the most important criterion. However, most of the decisions which affect LCC have been made during the early phases of the program; in particular, during conceptual studies and engineering design. Therefore, it is most appropriate that part of the MIRA effort should address the development of LCC techniques to aid the system designers in working towards a design which will meet performance requirements at an affordable cost to the government, rather than waiting to determine the costs after a design has been chosen.

## 5.3 LCC Model Survey

With respect to MIRA, the most useful of the models identified in Section 5.1 is the accounting model which estimates the aggregate of all the costs, and yet permits preselected cost areas to be considered separately. As the program work progresses, such an approach would be refined to produce increasingly better estimates of LCC. However, the application of one or more of the other types of models is not ruled out, and may be required as the MIRA effort progresses.

The first item considered in the LCC effort for MIRA was the review of available LCC accounting models from both DoD and industry. A USAF review<sup>(9)</sup> of LCC models developed for and by the military concludes that most of the general models (including the accounting type) are inadequate because they lacked focus on specific decisions or trade-offs, did not describe a particular equipment or system very well, and required excessive and specialized data. An earlier review of LCC



models by industry<sup>(10)</sup> indicated that the available models relating to military systems are too limited in scope, too complex, and required unavailable data, or are excessively time consuming.

Two comprehensive, accounting-type LCC models have been selected for possible application to MIRA. Both have been recently developed by knowledgeable LCC personnel and avoid many of the pitfalls described in the two surveys referenced previously. They are as follows:

- (1) The "Cost Reduction Is Everyone's Responsibility" (CRIER) model, developed by the Life-Cycle-Cost Task Group of the Joint Services Data Exchange for Inertial Systems. This Task Group is composed of representatives from the Armed Services (Air Force, Navy, and Army), industry, and the academic/research community. CRIER is very comprehensive and includes R&D, acquisition and operations, and maintenance factors. It is available without charge and recommended by the Task Group as the standard LCC accounting-type model for the Armed Services.
- (2) The "AGMC Model for Inertial Navigation Systems," developed by personnel at the USAF Aerospace Guidance and Metrology Center. In an overall sense, this model is less comprehensive than CRIER, but also includes R&D, acquisition, and O&M costs, as well as being available without charge.

#### 5.4 The CRIER Model

The CRIER model was the only one considered during this phase of the MIRA effort since it is an accounting-type model developed specifically for inertial systems. It is also applicable to all types of electronics systems and comprehensive, including all costs from conceptual studies through operations and maintenance to disposal. The CRIER model can be used in design tradeoff studies and is readily available. CSDL personnel are familiar with CRIER since they participated in the generation of the model through membership in the Life-Cycle-Cost Task Group.

Some of the major advantages of CRIER are:<sup>(11)</sup>

- (1) It includes the interests of both industry and the military.
- (2) It allows for general or detailed data inputs.



- (3) It contains general cost factors which can be overridden as specific data become available.
- (4) It provides selectable standard output reports.
- (5) It allows the user to develop his own output reports.
- (6) It contains override features when only specific sections of the model are of interest.

Special characteristics of CRIER permit the user to select applicable cost categories and select the level of input-data detail. Also, input data are required only for applicable cost categories, and spares prediction is cost optimized using Poisson distribution probabilities.

Table 5-1 lists the major cost elements included in CRIER and illustrates the comprehensive nature of this model.

The CRIER LCC model has been installed on the CSDL AMDAHL 470 central computer, and is in the process of checkout and evaluation.

#### 5.5 LCC Impact on Design

The traditional approach to life-cycle costing is illustrated in the upper half of Figure 5-2. The requirements for the equipment are translated into a set of detailed performance specifications, and an engineering-design LCC analysis is then performed to obtain the total costs of the proposed design.

In the MIRA approach, illustrated in the lower half of Figure 5-2, LCC analysis becomes an integral part of the performance-specification and engineering-design efforts by providing continuous cost feedback during these processes.

After a specific approach to equipment design is selected, the detailed equipment and LCC designs proceed with continuous feedback from the LCC efforts to the engineering effort. Thus, tradeoffs are conducted during all phases of performance specification and equipment design (from major decisions, to lower level detailed design and O&M concepts).

Tradeoff studies should specifically address elements which experience has shown to be high-cost drivers in order to achieve the optimum design approach at minimum LCC. Reliability is a major cost driver, and affects the costs of spares, maintenance, transportation, etc. The CRIER model enables tradeoff studies to be conducted as basic

Table 5-1. CRIER major cost elements.

<u>RD&amp;E</u>	<u>Acquisition Costs</u>	<u>O&amp;M Costs</u>
Conceptual Studies	Production	Organizational Maintenance
Engineering Design	Nonrecurring	Direct Labor
Software	Startup	Indirect Costs
Testing	Tooling & Test Equipment	Replacement Training
Hardware	Recurring	Support Equipment Maintenance
Spares	Installation	Intermediate Maintenance
Support Equipment	Technical Data	Direct Labor
Technical Data	Initial Logistics Cost	Indirect Costs
Modifications	AGE/GSE/TE*	Material
Training	Spares	Transportation
Training Devices	Line Replaceable	Spares Replenishment
Personnel	Shop Replaceable	Replacement Training
Program Management	Condemnation Items	Support Equipment Maintenance
Government	Technical Publications	Depot Maintenance
Contractor	Prime Hardware	Direct Labor
	Support Equipment	Material
	Training (Maintenance)	Indirect Costs
	Equipment	Transportation
	Initial Training	Spares Replenishment
	Tech Reps	Warranty Costs
	Facilities	Replacement Training
	Item Management (Initial)	Support Equipment Maintenance
		Inventory Management
		Maintenance Management Data

\* Aerospace Ground Equipment/Ground-Support Equipment/Test Equipment

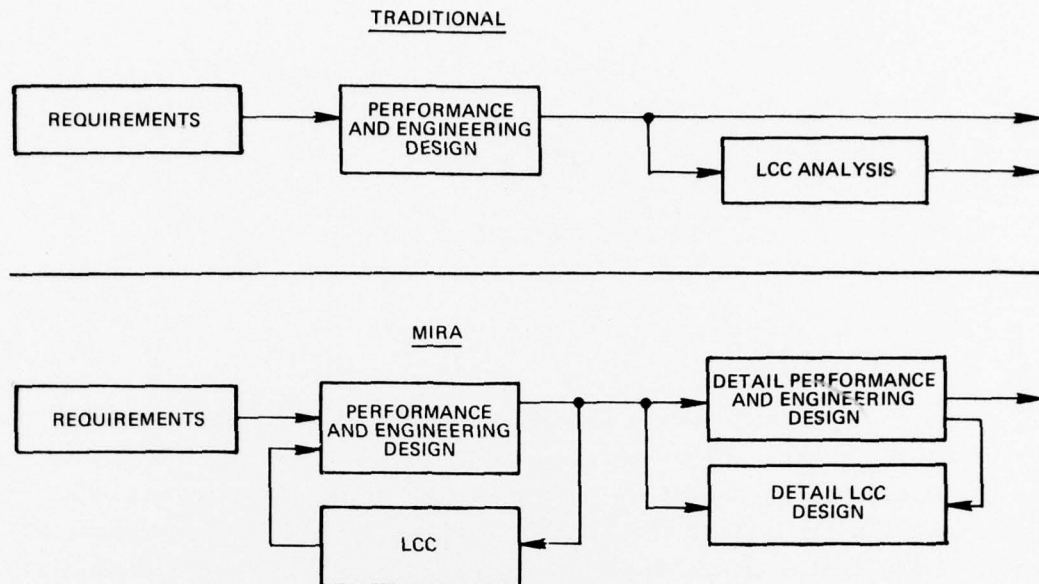


Figure 5-2. Approaches to life-cycle costs.

cost input data are developed. Typical examples of LCC impact areas which could be subjected to tradeoff analysis include:

- (1) Performance versus reliability.
- (2) Performance versus test/test-equipment cost.
- (3) Built-in calibration versus calibration plus software change.
- (4) Built-in test versus test by software versus troubleshooting.
- (5) Throwaway versus repair.
- (6) New parts versus standard parts.
- (7) Redundancy levels.
- (8) Plug-in modules versus hard-wired modules.
- (9) Reliability versus maintainability.
- (10) Optimum maintenance concepts.

The integration of LCC techniques into the design process can significantly aid in achieving a MIRA design which will meet performance requirements at a minimum life-cycle cost.

## SECTION 6

### SUMMARY AND CONCLUSIONS

#### 6.1 Phase I Summary

The Phase I MIRA effort at CSDL was dedicated toward developing tools and techniques which will be useful to the Air Force in the design and evaluation of MIRA systems over the long term. It was felt that the multidisciplinary goal of the MIRA program required the development of a unique capability which could evaluate all aspects of candidate MIRA systems.

The primary tool intended for the MIRA program was an all-digital real-time dynamic and kinematic simulation, which could be used to evaluate a wide class of MIRA systems in many different environments.

Although a hybrid (analog/digital) simulation would have represented a more classical approach to the problem, particularly since high-frequency dynamics (e.g., body-bending response) are of interest, it was felt that an all-digital approach provided a substantial advantage in terms of flexibility, stability, and repeatability. The digital-processor technology available at CSDL could support an all-digital real-time simulation, and has significant growth potential to support future program developments.

Sufficient simulation capability was required to include at least the lower frequency-bending dynamics, and provide a realistic dynamic environment for the MIRA instruments. Although it was anticipated that these effects would have a relatively small impact on the navigation performance, it was felt that they would affect the flight-control performance significantly.

All of the simulation goals, except for the full real-time capability, were realized in Phase I. The lack of a real-time capability would represent a major handicap for a program which was heavily oriented toward testing, but had a relatively small impact on this developmental portion of the program.



Thirteen different MIRA configurations were investigated; they represented a wide range of system configurations and constraints. Although the test periods used in this phase were short, the systems demonstrated comparable performance for both navigation and flight control in the tests accomplished. Although strong conclusions were not drawn concerning the relative merits of these configurations, it was felt that these cases did successfully demonstrate the flexibility of the basic tool to accommodate a wide class of MIRA systems.

The vehicle model used in the Phase I simulation was well documented, and a significant amount of equivalent data were available to CSDL from the literature. This comparative data provided a valuable check during the development phase of the simulation. Although not a true state-of-the-art vehicle, the performance was sufficient to point out some of the limitations of strapdown systems when used in the MIRA context. Conversion of the vehicle model to other aircraft during this phase was limited only by data availability, particularly for data relating to body-bending dynamics.

The relatively straightforward stability-augmentation control system appeared to function adequately with either dedicated flight-control sensors or flight-control data derived from navigation sensors. In systems with very small phase margins, the derived data might prove unacceptable, particularly if phase stabilization of the body bending is required.

The navigation algorithms included in the simulation were derived from the Standard Navigation Software effort, and they proved adequate for the system considered. Because of the relative magnitudes involved, however, evaluation of navigation errors was difficult, and sensor errors were indistinguishable from model, algorithm, and numerical roundoff effects. A modification to the navigation algorithms to allow a clearer evaluation of sensor effects is proposed for Phase II.

The life-cycle-cost effort provided survey data concerning life-cycle-cost models and some preliminary parametric data concerning the impact of design decisions upon life-cycle cost. This overall effort was hampered by the highly empirical nature of most life-cycle-cost analysis models, and the high degree of specificity required for many system parameters. Without a specific system design, the impact of many of these factors could not be assessed. It is felt that the overall concept of utilizing life-cycle-cost data on an a priori basis is promising for an effort such as MIRA, and the communication channels



between the engineering and life-cycle-cost areas should be kept open to provide coordinated system design decisions.

In summary, it is felt that the Phase I effort achieved its primary goals of demonstrating a viable approach for evaluating MIRA-type avionics systems from many aspects. The basic tools developed during this effort are currently available at CSDL and will be used in all further efforts in this area.

## 6.2 Phase II Inputs

During the course of the Phase I MIRA effort, there were several areas of investigation encountered which appeared to suggest meaningful candidates for the follow-on effort. Some of these areas were anticipated at the beginning of the Phase I effort, while others only became apparent as the effort progressed.

They are as follows:

- (1) Real-Time Capability - It is highly desirable to provide full real-time capability for the complete simulation. This not only allows man-in-the-loop activity, but greatly improves the efficiency of the navigation testing which, by its very nature, must represent relatively long duration tests.
- (2) Alternate Aircraft Models - The basic simulation structure is adaptable to a wide class of vehicle models. A more state-of-the-art fighter model is desirable from a system-application viewpoint, and a transport model may be desirable from a MIRA program validation standpoint. The largest constraint in adapting the simulation to different vehicle models is obtaining sufficient data, particularly in the area of bending dynamics. It is not felt that there would be significant gain in converting to a rigid-body model if bending data is not available.
- (3) Alternate Sensor Models - The simulation is readily adapted to utilization of alternate sensor models for MIRA systems. The approach of modeling sensor errors is quite general, and there exist data on a wide class of suitable sensors.
- (4) Navigation Error Analysis - The approach to navigation error analysis should be modified to that discussed in

Section 3.13 in order to allow more efficient separation of sensor errors from all other effects detrimental to navigation accuracy.

- (5) Study of Aided Navigators - From a system design viewpoint, it appears highly desirable to expand the MIRA system concepts studied to include a variety of aided navigators (e.g., TACAN or GPS)\*. Such aided systems might have significantly different MIRA sensor requirements than unaided systems.

These items seem to represent areas of natural evolutionary development for the MIRA effort at CSDL to allow its utilization as a meaningful evaluation tool for potential MIRA systems and for testing and developing MIRA system concepts of interest to the Air Force.

---

\* TACAN = Tactical Aid to Navigation.  
GPS = Global Positioning System.

# LIST OF REFERENCES

1. Eulrich, B. J., N. C. Weingarten, Identification and Correlation of the F-4E Stall/Post-Stall Aerodynamic Stability and Control Characteristics From Existing Test Data, AFFDL-TR-73-125, November 1973.
2. Hooker, D., R. Kisslinger, G. Smith, M. S. Smyth, Survivable Flight Control System Interim Report No. 1 Studies, Analyses and Approach, AFFDL-TR-71-20, May 1971.
3. Kisslinger, R., G. Vetch, Survivable Flight Control System Interim Report No. 1 Studies, Analyses and Approach Supplement for Control Law Development Studies, AFFDL-TR-71-20 Supplement-2, May 1971.
4. Hendrick, R., A. Bailey, L. Edinger, Design Criteria for High-Authority Closed-Loop Primary Flight Control Systems, AFFDL-TR-71-78, August 1972.
5. Sciegienny, J., R. Nurse, J. Wexler, P. Kampion, Inertial Navigation System Standardized Software Development, Final Technical Report, Volume II, CSDL Report R-977, June 1976.
6. Pritchard, F., J. Schuler, Six-Degree-of-Freedom Equations of Motion for a Maneuvering Re-entry Vehicle, Cornell Aeronautical Laboratory Report TE-1411-F-1, August 1961.
7. Houboult, J., R. Steiner, and K. Pratt, Dynamic Response of Airplanes in Atmospheric Turbulence Including Flight Data on Input and Response, NASA TR-R-199, 1964.
8. Nurse, R., Navigation and Attitude Error Propagation For a Strap-down Inertial Navigator-Given Inertial Sensor Error Time Histories and Flight Profile, CSDL Memo T&A 269-76, 7 December 1976 (TBP).
9. Collins, Lt. Dwight E., Analysis of Available LCC Models, and Action Required to Increase Future Model Applications, AFSC/AFLC Joint Commanders Working Group on LCC, WPAFB, December 1974.
10. Walker, Gary A., Life Cycle Cost/System Effectiveness Evaluation and Criteria, Boeing Aerospace Co., Document D180-17648-1, December 1973.
11. Proceedings of the Tenth Data Exchange for Inertial Systems, San Diego, California, 16-18 November 1976.